Surface stress and large-scale self-organization at organic-metal interfaces

Dissertation zur Erlangung des
naturwissenschaftlichen Doktorgrades
der Julius-Maximilians-Universität Würzburg

vorgelegt von

Florian Pollinger

aus Erlenbach am Main

Würzburg 2008

für Renate und Clemens

If I have seen a little further, it
is by standing on the shoulders
of giants.

(Isaac Newton)

Contents

Contents

List of Figures

List of Tables

Introduction

The future of nanotechnology could be based on a simple, yet ingenious idea: Let nature do the work.

Self-organization (or *self-assembly*) promises a realization of this vision. It is a growth principle which can be found at all possible length scales in nature, from weather systems down to crystal growth. Hence, it is not surprising that it is embraced by many disciplines in science, from biology, over physics, to chemistry, and material sciences [1].

From a technological point of view, self-organization can be a principle to control the bottom-up growth of nanostructures [2]. Different approaches have been identified for its application: From hybrid combinations with lithographic methods, over the liquid assembly of mesoscopic devices, to the ultimate goal of bio-functionalized recognition inspired by DNA [3]. Beyond visions, self-organization has already been very successfully exploited, e.g., for the growth of semiconductor quantum dots [2, 4].

Besides its conceptual appeal, self-organization is also associated with high cost-efficiency. It is not at least for this reason why it is interesting for organic electronics [5]. Indeed, self-assembled, purely heterorganic "nanodots" have been demonstrated recently [6, 7].

In particular, template-assisted bottom-up growth is a possible way to grow lateral, one-dimensional structures on scales of tens of nanometers [8]. For this purpose, vicinal or periodically faceted surfaces can be suitable templates [9, 10].

Moreover, organic adsorbents and vicinal metal surfaces can form morphologic and chemical gratings with a periodicity on nanometer, and a homogeneity on

micrometer scales by self-organization [11, 12]. In principle, this material class unifies all the properties of a template. Nevertheless, the complex interplay of the involved interactions impedes intuitive predictions [10, 13].

In fact, the understanding of these interfaces is mainly based on continuum models developed in the 1980s and early 1990s [14–16]. But a direct experimental verification of the basic physics and suspected driving forces is missing completely.

In this thesis, self-organization and faceting is studied by an unprecedented combination of complementary in-situ methods: The formation of the interface between 3,4,9,10-perylene-tetracarboxylic-dianhydride (PTCDA) and Ag(10 8 7) has been investigated by microscopic and diffractive methods, combined with a technique sensitive to the changes of surface stress. In particular, the latter method has been applied for the first time to interfaces formed by large aromatic molecules and metal surfaces.

These methods are briefly introduced in chapter 2. Subsequently, the concept and understanding of surface stress in literature is reviewed. In addition, the change of surface stress upon formation of the model interface PTCDA/Ag(111) is studied in chapter 3. The interpretation of the results in the framework of the theory of elasticity fits to the existing profound knowledge of the properties of this interface. Thus, the applicability of the method to metal-organic interfaces can be demonstrated.

As a consequence, the more complex and less understood faceted interface PTCDA /Ag(10 8 7) can be studied with confidence in chapter 4. Indeed, the combination of in-situ stress change and structural data provides evidence for an intimate relationship between surface stress change and morphology. Thereby, experimental evidence can be provided for these thermodynamic forces to drive the structural transitions. Additionally, insight into the role of kinetics and of defects can be gained.

Furthermore, actual template-assisted growth of lateral heterorganic nanostructures is investigated in chapter 5, which is based on the PTCDA/Ag(10 8 7) interface. Finally, a summary of the results is given in chapter 6.

Experimental methods

The experimental methods used in this work will be introduced in this chapter. After a summary of standard methods, more emphasis will be placed on methods based on diffraction of electrons of low kinetic energy. Thereby, information is provided which is necessary to understand many of the following analyses of vicinal and faceted surfaces. Finally, a brief introduction into the cantilever bending method is given, certainly being the most specialized technique of this work.

2.1. Standard methods

The methods and setups discussed in this section have been described in detail before. Therefore, I will only briefly summarize them for completeness, and instead give references of comprehensive reviews and textbooks for further detail.

UHV

The experiments have been performed under ultra high vacuum (UHV) conditions in four different UHV chambers, three at Würzburg [17–19] and one at Berlin [20]. The base pressures were better than $5 \cdot 10^{-10}$ mbar in all the experiments.

Substrate preparation

Various silver crystals have been used as substrates in this work, both, "conventional" crystals of a thickness in the order of 1 mm, and thin (i.e. approximately

140 μm thick) crystal slices optimized for the cantilever experiments.

The cantilever crystals and the vicinal crystal used in the LEEM experiments were prepared from bulk Ag(111) single crystals in the course of this work. The Laue method [21] was used to determine the correct azimuthal orientation of the crystal, and the deflection of a laser beam for the polar orientation. The error bar of both methods is in the order of 0.2°. The rectangular cantilever crystals were cut from the raw material by spark erosion at the Max-Planck-Institut in Halle. Subsequently, the oriented crystals were sandpapered at Würzburg until the desired thickness was reached.

The thickness of the cantilever substrates was determined by measuring their resonance frequencies ν_1. Therefore, they were excited by a frequency generator (Voltcraft FG1617), and their oscillation was monitored by a spectrum analyzer (HP 8560E). The thickness t_s of the samples can be deduced from the resonance frequency ν_i by

$$\nu_i = \frac{t_s \beta_i^2}{4\pi l^2} \sqrt{\frac{Y}{3\rho}}, \tag{2.1}$$

with Y being Young's modulus, l the length, and ρ the density of the sample. The parameter β_i depends on the order i of the harmonic of the excited resonance (with $\beta_1 = 1.8751$, $\beta_2 = 4.6941$, and $\beta_3 = 7.8548$) [22]. The physical properties of the cantilever samples are compiled in table 2.1.

The crystal surfaces were prepared by several sputter- and annealing cycles. Ar$^+$-ion sputtering was performed using a kinetic energy of 700 eV at a partial pressure of argon of $1.5 \cdot 10^{-5}$ mbar. The quality of the vicinal surfaces depended strongly on the annealing process. The most homogeneous step separation was observed when annealing for 30 minutes at 700 K. Furthermore, this annealing temperature was carefully approached by heat ramps of 4-8 K/min in the case of the cantilever crystals in order to prevent the fragile crystals from thermally induced distortion.

Growth of organic monolayers

The molecular layers were grown in vacuo. Two different approaches had to be followed for the two types of molecules investigated in this work.

Table 2.1.: **Physical properties of the silver cantilever substrates.**

orientation	thickness [μm]	length [mm]	width [mm]	resonance ν_1 [Hz]
(10 8 7)	149 ± 2	6.7 ± 0.1	2.9 ± 0.1	2706 ± 2
(111)	139 ± 2	11.3 ± 0.1	2.7 ± 0.1	661 ± 2

4

3,4,9,10-perylene-tetracarboxylic-dianhydride (PTCDA) (for structure see chapter 3.3) is a solid powder at room temperature. Moreover, the vapor pressure is low enough that it can be stored under UHV conditions. Therefore, it is suitable for organic molecular beam deposition (OMBD), i.e. evaporation in UHV from Knudsen cells [23]. The powder was purchased from TCI and further purified by sublimation heating cycles in vacuum. Different home-made Knudsen cells were used in this work, designed to fulfill the boundary conditions of the various in-situ experiments.

The decanethiol molecules, discussed in chapter 5, are fluid at room temperature. Their partial vapor pressure has been measured to be in the order of 10^{-2} mbar in the experiments. Therefore, they could not be stored in UHV and had to be entered into the chamber by a leak valve. The decanethiol was purchased from Sigma-Aldrich (nominal purity of 96 %). In order to evacuate and to purify the material further, several freeze-pump cycles were performed during which the fluid was frozen and its repository evacuated to high-vacuum conditions.

XPS

The samples were characterized by x-ray photoemission spectroscopy (XPS) [24]. Usually, the coverage was also determined by this method. The data discussed explicitly in chapter 5 was measured by a combination of a VG XR2E2 twin anode and a VG CLAM2 analyzer with a pass energy of either 20 or 50 eV.

TDS

Furthermore, thermal desorption spectroscopy (TDS) [25] was used to investigate the chemical bonding of the self-assembled monolayers (see chapter 5). Therefore, a Balzers QMG 422 quadrupole mass spectrometer was combined with a VG RHC heat control unit (based on a Eurotherm 2408 PID controller). The system was synchronized and the data recorded by a home-made software developed in LabVIEW (National Instruments).

STM

The morphology of the co-adsorbate films was investigated by scanning tunneling microscopy (STM), which is sensitive to the electronic density of states in the vicinity of the Fermi levels of surface and tip [26]. A "beetle-type" STM [27] with Pt-/Ir-tips was used for imaging. Typical working parameters of this apparatus are tunneling voltages between -2.0 and +2.0 V, and tunneling currents between 0.2 and 1.5 nA. The apparatus has been described in detail by Seidel [17]. Principles of this technique can be found, e.g., in the textbook by Bonnel [28] and in the thesis by Herber [29].

2.2. Methods based on electron diffraction

Many of the results discussed in the following chapters have been gained by methods based on the diffraction of electrons of low kinetic energy (LEED). While "conventional" rear-view LEED is a well-established method in surface science [30], the particularities of SPA-LEED and LEEM justify a slightly more detailed introduction. In addition, information is provided which is necessary to understand some of the analyses in chapter 4.

2.2.1. Spot profile analysis LEED

The high resolution LEED data was recorded by a spot-profile analysis LEED (SPA-LEED). This technique, developed by Henzler and co-workers [31], is characterized by a high angular resolution in momentum space. The properties and the instrumentation of this technique have been thoroughly reviewed by Horn-von-Hoegen [32]. Moreover, the specific setup has already been described in detail by Kilian [18]. Nevertheless, a brief survey on the most important properties is given.

The high resolution is achieved by a 0-dimensional detector (a channeltron) whose acceptance angle is further narrowed by an additional aperture. In addition to its benefit for the resolution, this detection scheme offers a high sensitivity and a high dynamic range in the order of 10^6.

Due to its geometry, the angle between incident and detected electron beam is fixed by the instrument. In order to scan through k-space, nevertheless, the electron beam is deflected by an octopole lens system. As a consequence, the diffraction pattern is recorded on a "modified" Ewald sphere. It is characterized by an origin at the (000) point in k-space, and by a diameter which is nearly twice the diameter of the conventional Ewald sphere [32].

The setup at Würzburg is equipped with a conic entrance lens. Therefore, it is possible to evaporate material from the side onto the sample while measuring simultaneously. These in-situ experiments were performed at a fixed temperature of 550 K with the sample in thermal equilibrium. Thus, the impact of the thermal expansion of the lattice constants was minimized. Furthermore, heating cycles and data recording were automatically alternated. Otherwise, the magnetic field of the heating coil disturbed the electron path significantly. Exposure of the sample to the Knudsen cell also changed the imaging conditions slightly. This effect is discussed in appendix C.

2.2.2. Low energy electron microscopy

A second imaging technique used is low energy electron microscopy (LEEM) [33–35]. This method works with electrons of kinetic energies between 1-100 eV, elastically backscattered from the sample surface [33]. Since an understanding of the contrast
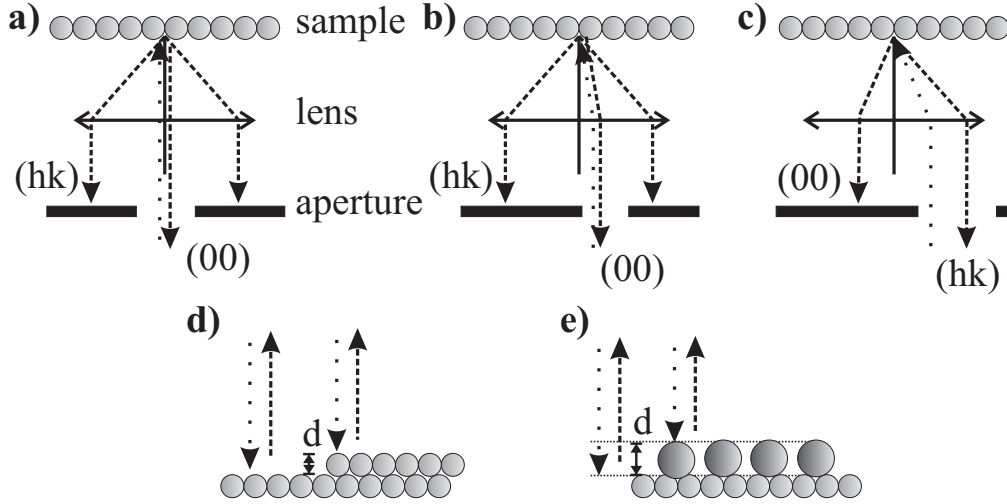
Figure 2.1.: **Contrast mechanisms in LEEM.** Schematic of the basic contrast mechanisms in LEEM as discussed in the text: **a)** bright-field mode under normal incidence, **b)** bright-field mode under tilted incidence, **c)** dark-field mode, **d)** geometric phase contrast at steps, **e)** quantum size contrast associated with thin films. (figure after [33] - In the SMART, the aperture is situated in the imaging optics. Therefore, the incoming primary does not have to pass the aperture as indicated in the schematic.)

mechanism is fundamental to interpret the results of this work, a brief summary will be given in the following paragraphs.

Contrast mechanisms

The interaction of "slow" electrons with surface atoms is governed by their wave nature [33]. Therefore, LEEM is closely related to LEED, to which it has been ascribed as "imaging counterpart" [33]. In fact, they are connected by the diffraction rods of a surface in k-space. In LEED, these rods are depicted as spots in the diffraction pattern. In LEEM, they are singled out by apertures in a diffraction plane to be used for imaging.

In principle, LEEM is sensitive to changes in the electronic reflectivity of the sample. The origin of this contrast, however, is not trivial. Five major mechanisms have been described in literature [20, 33–35], and are schematically depicted in figure 2.1.

Usually, the directly reflected, *specular* electrons are imaged. In LEED notation, these electrons correspond to the (00) spot. The imaging mode is referred to as *bright field (BF) imaging*. If the incident beam hits the sample normally (figure 2.1a), the differences in reflectivity of the specular reflex are based on structural differences for planar surfaces. In diffraction experiments, this effect is well-known

as energy-dependence of the intensity of LEED spots (LEED-I(V), see e.g. [30]). Examples for such structural differences are domains of surface reconstructions, local strain fields in the vicinity of defects or even different surface orientations [33].

Individual superstructure domains on the surface can be distinguished by two different approaches. Firstly, it is possible to break the isotropy of these domains with respect to the incoming beam in bright field mode. For this purpose, the primary electron beam has to be tilted slightly off-axis (figure 2.1b) [33]. A second approach is to select an intense higher order diffraction spot (hk), and not the specular reflection for the imaging (figure 2.1c). This mode is known as *dark field (DF) imaging* in LEEM. The detected intensity can be ascribed to the corresponding domain of the structure [36, 37] in this case.

Beyond these fundamental contrast mechanisms, intensity variations can have additional reasons on more heterogeneous surfaces.

The fact that different path lengths can induce interference effects is of major importance for the samples investigated in this work [20]. At steps (figure 2.1d), e.g., both intensity enhancement and extinction is possible, depending on the scattering phase S (compare chapter 2.2.3) of the electron beam. This effect is usually referred to as *geometric phase contrast*. Furthermore, the so-called *quantum size contrast*, observed for thin films (figure 2.1e), is of the same origin [33].

Additionally, it should be mentioned that the cross section of the backscattering process depends on the element [33]. Therefore, different atomic species adsorbed in domains large enough to be resolved can also induce different contrasts.

Finally, large protrusions on the surface distort the local electric field and thereby influence the trajectories of the electrons, thus inducing an additional contrast mechanism.

Facet-sensitive contrast

Surfaces consisting of different mesoscopic facets can be investigated by a variation of the dark-field mode: If the specular spot of the facet is selected for imaging (see figure 2.2), bright areas can be ascribed to the corresponding facet types. Since some specular facet spots overlap for the typical kinetic energies used, a mixture of different facet types can be seen in the dark-field images. Using intensity thresholds, images of the brightest facets can be extracted by the subsequent data processing.

This imaging mode has been successfully demonstrated to study in-situ the gold-induced faceting of vicinal Si(001) [38–40].

Local LEED

Besides real space imaging, it is possible to record a "local LEED pattern" directly in LEEM, i.e. the LEED pattern of a selected area of μm-diameter. For this pur-
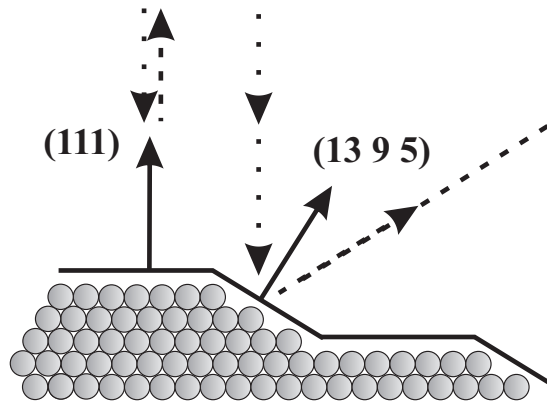
Figure 2.2.: **Direct reflections on different facets.** The direct reflection of the incoming electronic beam (dotted line) is separated by different facets on the surface. These specular reflections can be selected for facet-sensitive dark-field imaging.
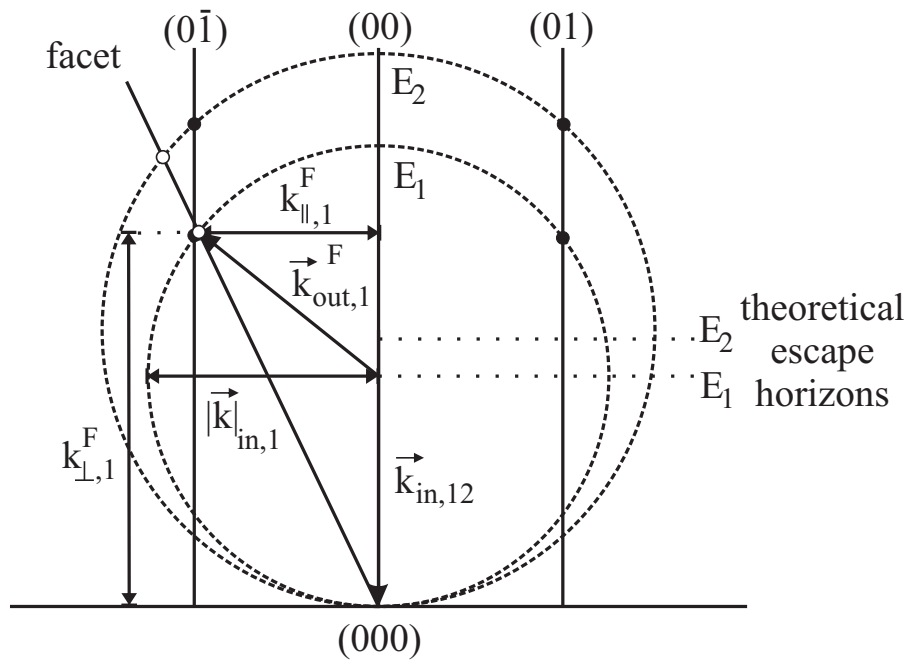
Figure 2.3.: **Ewald construction in LEEM.** The Ewald sphere is depicted for 2 different energies E_1 and E_2. All electrons whose exit momentum vectors $\vec{k}_{out}$ point above the theoretical escape horizon are imaged in the diffraction plane. Facet spots (open circles) move with increasing energy, while spots associated with the (111) surface (closed circles) remain fixed. The geometric considerations to derive the vertical k-space coordinate $k_\perp$ are indicated for one facet spot.

pose, a diffraction plane is imaged instead of an image plane, which only requires the transfer optics to be changed. In this study, the area to be investigated (diameter 1 μm) was selected by an aperture in an image plane. Alternatively, it is also possible to limit already the illumination by entering an aperture in the primary beam (*micro-spot LEED*) [35].

The imaged LEED pattern demonstrates the power of the method once more. In principle, the whole outgoing cone of diffracted electrons is imaged in the diffraction plane. Thus, the projection of the complete upper half of the Ewald sphere can be investigated.

As can be seen in figure 2.3, the radius of the imaged disc can be associated to the maximum parallel scattering vector $k_{\parallel}$. According to the Ewald construction, it is in absolute value identical to the incoming electron momentum vector $\vec{k}_{in}$. Furthermore, as a convenient consequence of this imaging mode, diffraction rods which are parallel to the optical axis are on fixed positions with respect to energy if the primary beam hits the sample under normal incidence [35]. Therefore, facet spots can be easily identified by their "moving" positions in k-space.

SMART

The LEEM experiments were performed at the SMART (Spectro-Microscope with Aberration Correction for many Relevant Techniques), a spectro-microscope at the BESSY II synchrotron facility at Berlin. This setup is distinguished from other spectro-microscopes by a sophisticated combination of the magnetic beam separator and an electrostatic tetrode mirror. This combination has been developed to correct simultaneously for chromatic and spherical aberrations of the objective lens [41, 42]. Moreover, the SMART is equipped with an "omega"-energy-filter, capable of an energy resolution of 0.1 eV [42]. In LEEM mode, the energy filter can be used to discriminate elastically scattered electrons from secondary and inelastically scattered electrons [41]. Details on the setup can be found in the theses by Marchetto [20] and Groh [43].

The ultimate goal of this correction effort is a lateral resolution of 2 nm or less in LEEM [42]. In the experiments of this work, however, a lateral resolution in the order of 10 nm was sufficient.

Finally, it should be emphasized in this context that organic thin films are highly sensitive to beam damage. Nevertheless, the SMART has been very successful in imaging organic-metal interfaces before [20, 43, 44]. The beam damage can be minimized by working with electrons of low kinetic energies. Moreover, the high sensitivity of the instrument allows to work with low electronic fluxes. Indeed, identical spots could be investigated for approximately 40 minutes without major beam damage in the experiments of this work.

2.2.3. Vicinal surfaces in low energy electron diffraction

The diffraction methods are used in this work to characterize vicinal and faceted surfaces. Steps, step trains and their interactions have been studied in diffraction for over thirty years [45]. Sophisticated analyses of the peak shapes allow conclusions on step distributions and interactions for one-dimensional (e.g. [46–49]) or two-dimensional vicinal surfaces [50–52].

In the frame of this thesis, however, the analysis is restricted to the morphologic composition of the surface. Although it is based on purely geometric considerations in k-space, a brief description of the analysis is given in the following paragraphs. Thus, I want to ease the understanding of the relatively compact presentation of the results in chapter 4.5.1.

Scattering phase S

The intensity of diffraction spots of stepped surfaces varies with energy [32, 45]. The dimensionless parameter S, the so-called *scattering phase* [32], is a very useful quantity to understand this effect. It is defined by [32]

$$S = \frac{k_\perp d}{2\pi},\tag{2.2}$$

with d being the height of a monoatomic step of the system, and $k_\perp$ the momentum scattering vector perpendicular to the terraces. From the physical point of view, it describes the phase difference $\phi = exp\,(i2\pi S)$ of electrons scattered at two adjacent terraces (compare figure 2.1d).

For integer values of S ($S = n$, Bragg-condition), these waves interfere constructively. A single, sharp LEED spot can hence be observed in the LEED pattern if this *in-phase condition* is fulfilled. Thus, the energy difference between two in-phase conditions can be used to determine the average terrace height [45]. Information on the lateral distribution of the steps, however, is completely lost for this diffraction condition [32].

The other extreme case in diffraction corresponds to half-integer values of S ($S = n + \frac{1}{2}$, anti-Bragg-condition), for which electron waves scattered from adjacent terraces interfere destructively. The scattered intensity is redistributed into the diffuse shoulder of the peak and reflects the lateral arrangement of the steps. The surface is effectively projected to a two-level system and the information on the vertical distribution of the steps is lost [32]. Two distinct peaks can be observed (spot-splitting) for homogeneous terrace width distributions. This distance in k-space Δk is directly related to the average terrace width Γ [32, 45] by

$$\Delta k = \frac{2\pi}{\Gamma}.\tag{2.3}$$

Intermediate values of S correspond to scattering conditions which are less well defined. The intensity variation of the specular spot with scattering phase S can be used to derive the vertical roughness of a surface ($G(S)$-*analysis*) [32].

Faceted surfaces in k-space

Before proceeding to the actual analysis, it helps to consider the k-space associated with a faceted surface qualitatively.

The Fourier transform of an ordered surface consists of (intensity modulated) rods standing perpendicular on the surface. In analogy, the Fourier transform of a surface consisting of differently oriented mesoscopic facets can be understood as a superposition of the Fourier transform of surfaces inclined with respect to each other. Indeed, sets of diffraction rods of different inclination angles form the k-space of such a system [32], which is illustrated in the bottom part of figure 2.4.

These intensity rods can be mapped in k-space by SPA-LEED and by LEED patterns obtained in the LEEM experiment. Thus, the geometric orientation of occurring facets can be determined.

3D reciprocal space maps

In principle, two-dimensional cuts through reciprocal space can be directly recorded by energy-dependent SPA-LEED line scans. Diffraction rods can be mapped with high precision by this technique [53–56]. The method is less practicable, however, for the system investigated in this work. As we will see, up to five facets of different azimuthal orientation are simultaneously present on the surface. In order to characterize them efficiently without too much loss of information, 3D reciprocal space maps have been reconstructed from an energy stack of two-dimensional SPA-LEED diffractograms. The necessary data processing is summarized in the following paragraphs and sketched in figure 2.4.

If a facet is aligned perpendicularly to the SPA-LEED system axis, its diffraction rods intersect the modified Ewald sphere at the same lateral coordinates in k-space for a wide range of kinetic energies. Inclined diffraction rods, however, intersect at different lateral coordinates when the energy is varied. Therefore, the respective peak seems to "move" in a series of SPA-LEED images of different energies.

This effect can be used to identify facets. If SPA-LEED diffractograms taken at different kinetic energies are properly rescaled and added up, the diffraction rods are effectively projected into the depicted plane in k-space. Internally, the SPA-LEED works with coordinates given in deflection voltages U of the octopole plates [54]. The deflection of a lateral momentum vector at a specific primary kinetic energy $k_\parallel (E_{kin})$ is proportional to $U/\sqrt{E_{kin}}$ in small angle approximation [54]. Therefore, diffractograms taken at different kinetic energies $E_{kin,i}$ can be rescaled

superposition of
diffractograms:
projections
of facet rods

overlaid
image

SPA-LEED
diffractograms
at different
energies

(222)

E_2

E_1

(111)

faceted
surface in
reciprocal
space

$k_\perp$

$k_\parallel$

(000)

SPA-LEED
Ewald spheres

(111)

(954)

faceted
surface in
real space
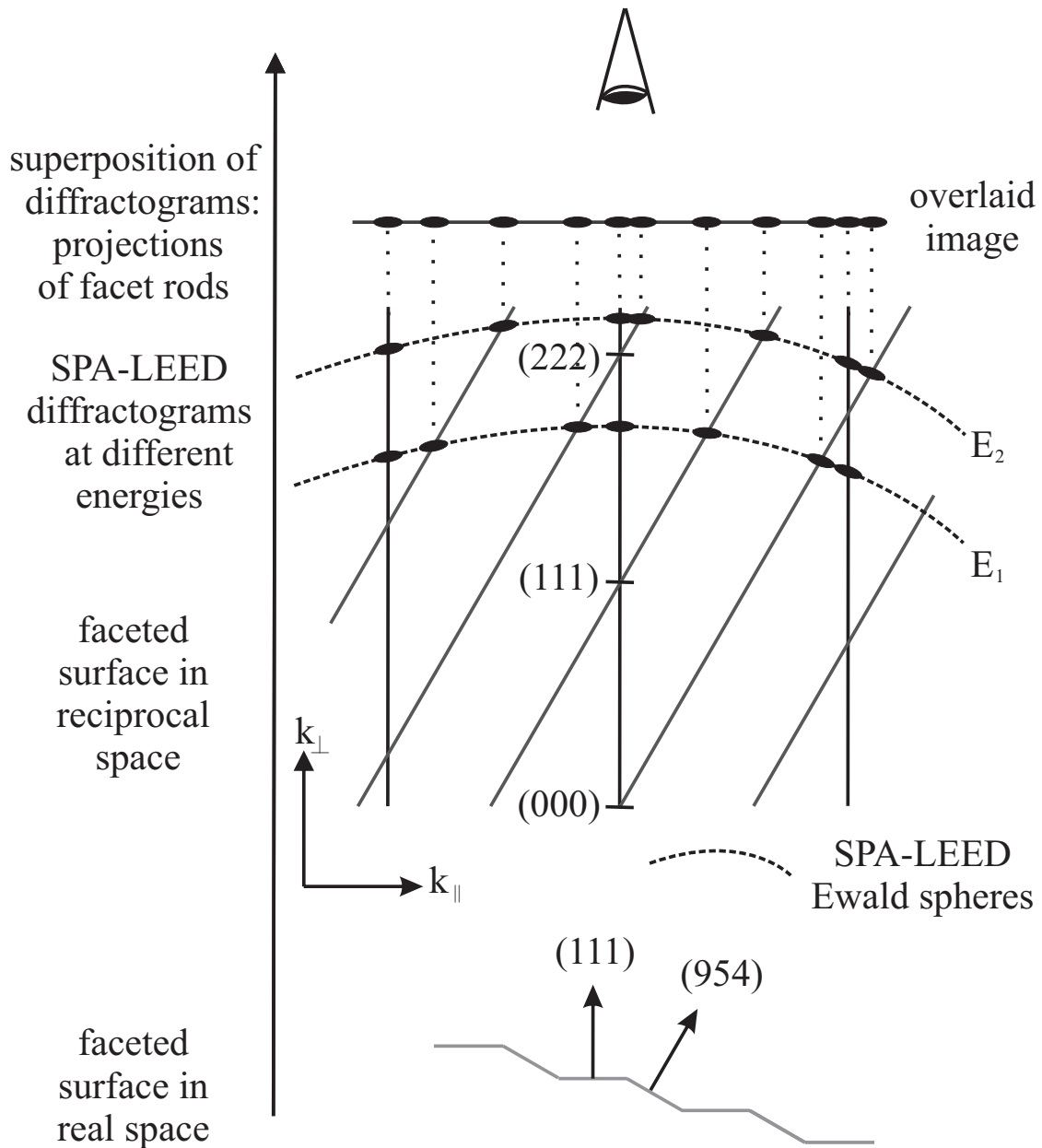
Figure 2.4.: **(De)composition of overlaid SPA-LEED diffractograms.** The diffraction rods of different facets are tilted against each other in reciprocal space. Therefore, corresponding diffraction peaks "move" in SPA-LEED diffractograms taken at different kinetic energies. Adding diffractograms corresponds to a projection of diffraction rods into the $k_\parallel$-plane. Thereby, the tilted facet rods leave a "trace" of spots in such an overlaid image.
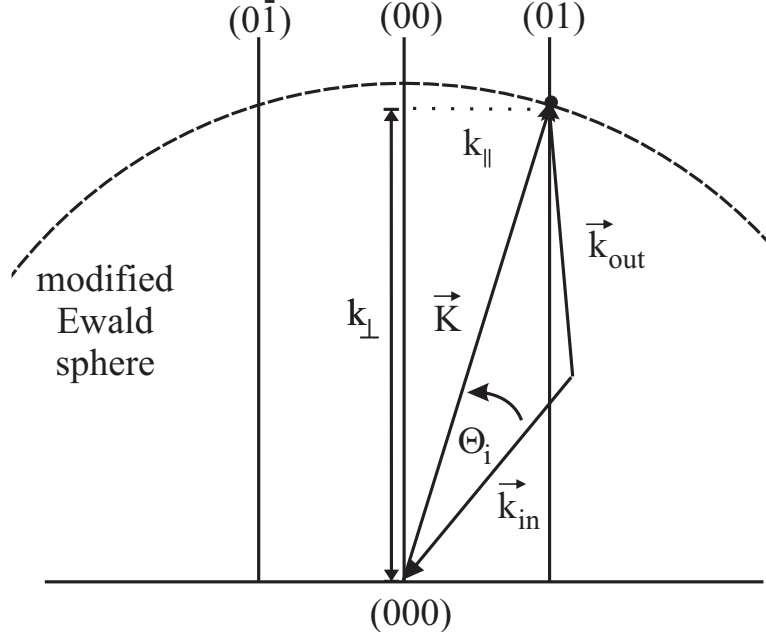
Figure 2.5.: **K-space coordinates in SPALEED.** The schematic illustrates how the vertical momentum vector $k_\perp$ can be deduced from a SPA-LEED diffractogram, knowing the parallel components $k_\parallel$ and the energy of the scattered electron beam.

to the coordinates of a reference energy E_{kin}^{ref} by

$$k_\parallel\left(E_{kin,i}\right) \propto \left(U\left(E_{kin,i}\right)/U\left(E_{kin}^{ref}\right)\right) \cdot \sqrt{\left(E_{kin}^{ref}/E_{kin,i}\right)}. \qquad (2.4)$$

When thus rescaled and diffractograms taken at different kinetic energies are laid over each other, rods normal to the surface appear as single spots. All Ewald rods tilted with respect to the surface normal leave a series of spots which will be called a *facet trace* in the following. Such traces will be used in chapter 4.5.1 to identify facets and to ascribe the numerous superstructure spots to sets of facet rods.

The coordinates $k_{\parallel x,y}$ in deflection voltages U can be calibrated to Å^{-1} by known structures. In this work a calibration factor of $\alpha = (0.1165 \pm 0.0018)$ Å^{-1}/V was used which had been deduced from a commensurate superstructure of CuPc on Ag(111) for a kinetic energy of 23.0 eV [57]. According to figure 2.5, the perpendicular coordinate $k_\perp$ can be calculated from the lateral coordinates $\vec{k}_\parallel$ and the kinetic energy E_{kin} as

$$k_\perp = \sqrt{2(1+cos(2\Theta_i)) \times \frac{2m_0}{\hbar^2}E_{kin} - \left|\vec{k}_\parallel\right|^2} \qquad (2.5)$$

with m_0 being the free electron mass and $\Theta_i = 4°$ the incidence angle of the primary electron beam of the SPA-LEED.

It is therefore possible, both to assign LEED spots to sets of diffraction rods and to determine their position with relatively high accuracy in three-dimensional k-space. The respective rods can then be fitted by linear regression as straight lines in 3D. Thereby, their polar coordinates Θ and Φ can be determined with relatively high accuracy. Thus, the facets can be identified and labeled.

Finally, the analogous procedure can be applied to reconstruct the reciprocal space from the LEEM-LEED data, too. Again, an energy stack of LEED images can be used to determine the polar coordinates of facet diffraction rods. The analysis is even slightly easier due to the convenient scaling properties of the projected Ewald sphere (compare chapter 2.2.2).

The lateral coordinates $\vec{k}_\parallel$ can be calibrated using inherent scales provided, e.g., by known superstructure spots. The S_A superstructure of PTCDA on Ag(111) was used in this work (compare chapter 3.3). The perpendicular coordinate $k_\perp$ in k-space can be derived from figure 2.3 as

$$k_\perp = \left| \vec{k}_{in} \right| \left(1 + \sqrt{1 - \left(\frac{\left| \vec{k}_\parallel \right|}{\left| \vec{k}_{in} \right|} \right)} \right) \tag{2.6}$$

with

$$\left| \vec{k}_{in} \right| = \sqrt{\frac{2m}{\hbar^2} E_{kin}}. \tag{2.7}$$

2.3. The cantilever bending technique

In this section, I will summarize the experimental technique used in this thesis to measure the change of surface stress by adsorption. A comprehensive introduction into the concept of surface stress and its physical relevance will be given in chapter 3.

Experimental setup

All techniques measuring the change of surface stress $\Delta\tau$ upon formation of an interface are based on the same principle [58]: The adsorption of material on only one side of a flat single crystal (i.e. without deposition on the backside) induces an asymmetry in surface stress. The system evades this asymmetry by bending, i.e. by changing its curvature. If the substrate is thin enough ($t < 0.5$ mm [58]), this change of curvature $\Delta(1/R)$ can be detected and quantified.

One detection approach is to monitor the curvature directly with STM [59–61]. Another approach is based on capacitive distance measurements [62, 63]. I
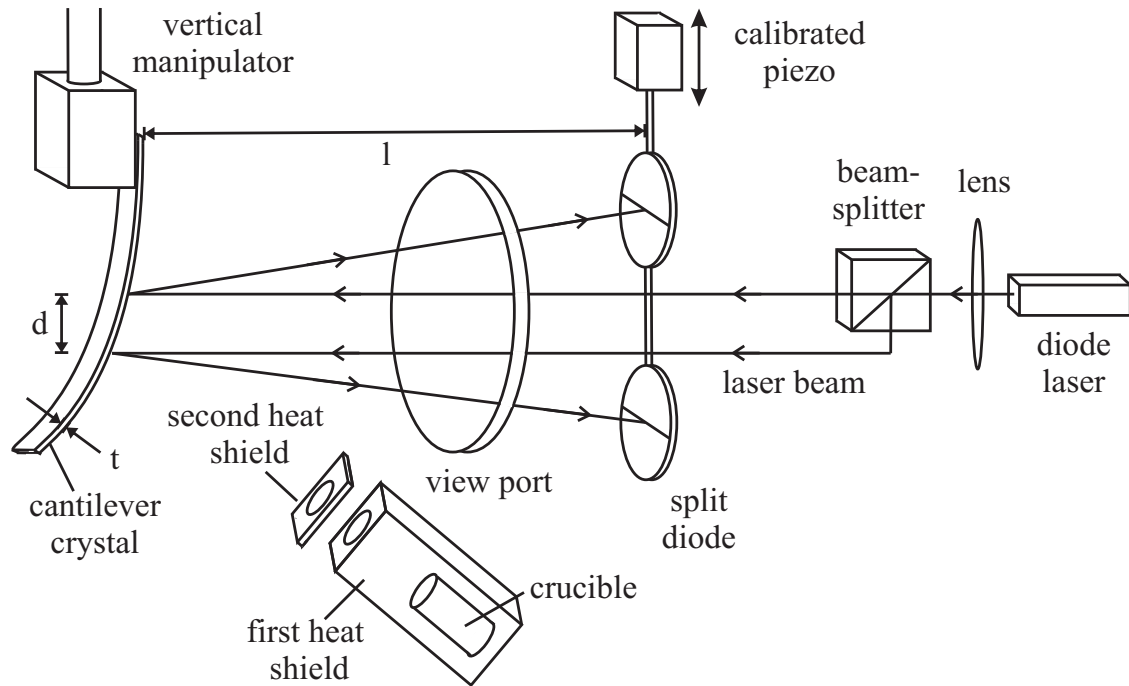
Figure 2.6.: **Set up of the cantilever bending experiment.** The optical setup can be attached ex-situ to a CF100 view port. In UHV, the interface is formed by evaporation of the molecules from a Knudsen cell with an optimized heat shielding. The major components of the setup, the optical path of the laser beam, and the geometric dimensions necessary for the data analysis (crystal thickness t, spot separation d, and distance cantilever to split diodes l) are indicated. Details are discussed in the text.

have used an optical detection scheme developed by Sander, Kirschner, and Ibach [58, 64–66], which will be discussed in more detail in the next paragraphs.

The setup was designed and built at the Max-Planck-Institute of Microstructure Physics at Halle. It can be transported and easily implemented into an existing UHV setup. A scheme is depicted in figure 2.6.

A laser diode beam is splitted in air and imaged onto two spots separated by the distance d on the cantilever crystal of thickness t. (The mounting of the cantilever is described in detail in appendix B.) The laser beams enter the UHV chamber through a CF100 view port to which the optical setup is attached. After reflection, they exit the UHV chamber again and get detected by two position sensitive split diodes. Their signal, recorded by digital voltmeters, can be calibrated externally. Therefore, a high precision piezo element induces a well-defined vertical translation of both detection diodes, which can be identified with the measured signal change.

The change of curvature $\Delta(1/R)$ can be derived by geometric considerations from the position changes Δx_1 and Δx_2 as [67]

$$\Delta(1/R) = \frac{\Delta x_1 - \Delta x_2}{2dl}, \tag{2.8}$$

with d being the separation of the laser beams on the sample and l the distance between sample and detectors. Following the usual sign convention, Δx_1 corresponds to the signal change of the beam reflected closer to the free end of the cantilever [67]. Beam separations of 4 to 5 mm were typically achieved for the Ag(111) substrate, and 1.5 to 2 mm for the shorter Ag(10 8 7) cantilever. The distance l between sample and detector varied between 23 and 25 cm.

Since the sample can be assumed to bend freely in two dimensions for the size ratios of the cantilever substrates used (see table 2.1) [68], the change of curvature $\Delta(1/R)$ can be associated with the change of surface stress $\Delta\tau$ by the modified Stoney equation [65]

$$\Delta\tau = \frac{Y_{Ag(111)}t^2}{6(1-\nu)}\Delta(1/R), \tag{2.9}$$

with the effective Young's modulus $Y_{Ag(111)} = 82.82$ GPa and Poisson's ratio $\nu = 0.513$. These elastic quantities have been derived for the Ag(111) surface using the elastic constants listed in [69] and the expressions given in [65]. I have neglected a possible temperature-dependence of these values in my analysis. In fact, Kury and Horn-von Hoegen argue the respective error to be in the order of 1% for the temperature range between 300 and 550 K in the case of silicon surfaces [70], which would be well below the error bar of my experiments.

Cantilever measurements in practice

A particular challenge for the experiments has been to identify and to exclude external influences on the signal.

At first, possible sources of vibrations (e.g. water cooling, air condition) were switched off although the setup, based on a differential measurement, is relatively stable against external vibrations. Furthermore, the pressure in the chamber was kept below $2 \cdot 10^{-10}$ mbar.

Besides these rather obvious external influences, artifacts induced by the experimental setup are more challenging.

All the experiments were performed at elevated temperatures. After surface preparation according to chapter 2.1, the cantilever crystal was slowly heated with approximately 4 to 8 K/min to the desired working temperature. The sample was kept at this temperature for at least three hours before proceeding. The temperature was controlled by a VG RHC heat controller. Both, sample temperature, and heating power were automatically logged throughout the experiment. Therefore, artifacts induced by variations of the temperature could be identified afterwards. If a temperature stability better than 0.1 K could have been sustained throughout the whole experiment, the temperature influence on the curvature change was below the detection limit.

Finally, the evaporator could have a strong influence on the detected signal, too. For once, mechanical movement was introduced into the system every time the shutter was opened or closed. Moreover, the crucible had to be thoroughly shielded from the sample by a combination of two pinholes (compare figure 2.6) to suppress the heat flux from the evaporator to a minimum.

Given the large number of possible disturbances, each cantilever adsorption experiment was followed by a validation experiment to check the stability of the setup. Therefore, the freshly formed organic-metal interface was exposed to the molecular beam again, at the same evaporator temperature and in the same geometry. At sample temperatures of 550 K, no bilayer film of PTCDA can nucleate (compare chapter 3.3). Hence, the experiment could be even repeated using the same experimental parameters (substrate and evaporator temperature) on a quasi-passivated sample. As a consequence, in this case any observed bending could be attributed to external influences only. In the following chapters, these reference measurements are always presented together with the experimental data.

Finally, the separately recorded difference position signals of the two split diodes were calibrated after the experiment and evaluated according to equations 2.8 and 2.9. A remaining overall linear drift, which can be identified in the data taken before the actual experiment, was subtracted from the data. Furthermore, the raw data was smoothed by a Gaussian convolution in order to reduce the noise level.

Surface stress upon chemisorption: PTCDA/Ag(111)

The investigation of the change of surface stress upon adsorption of 3,4,9,10-perylene-tetracarboxylic-dianhydride (PTCDA) on Ag(111) is documented in this chapter. The experiment is motivated by two different goals. First, it adds a piece of information from a new perspective to this archetype metal-organic interface. Second, the measurement establishes confidence into the applicability of the cantilever technique to such organic-metal interfaces. Those goals can only be reached if the data is interpreted and analyzed in the right context. Therefore, the necessary definitions, literature models, and a brief introduction into the system are given in advance to the actual experimental part.

3.1. The concept of surface stress

The basic equations of elasticity are attributed to works of Cauchy and Poisson in the 1820s . The thermodynamic framework and its application to interfaces and surfaces have been introduced by Gibbs [71]. In the last two decades, considerable progress has been made in the understanding of its relevance at surfaces and interfaces [65, 72–75]. Due to the long tradition, however, definitions and expressions sometimes appear rather vague or even contradictory when comparing different authors (see e.g. discussion in [76–78]). In order to provide a sound basis for this work, the most important definitions and relations are given in the following section.

3.1.1. Strain and stress at bulk, interface, and surface

The surface quantities are introduced as excess quantities of the respective bulk properties. Therefore, first the definitions of the bulk strain, stress and elastic energy are briefly recapitulated.

Bulk quantities

As a starting point, a body consisting of a continuum medium is considered. If a force is applied to the body, a point $\vec{r}$ in the medium changes its position by its *displacement vector* $\vec{u} \equiv \vec{r'} - \vec{r}$. To describe the whole continuous medium, the concept of the displacement vector is mathematically extended by the introduction of the *displacement field* $\vec{u}(\vec{r})$.

If the body now changes its shape under the force, the distances between the individual points change, too. Assuming only small deformations, the extension (or compression) of an infinitesimal element of length dl can be described by the symmetric *strain tensor* ϵ_{ik} (with i, k representing the respective cartesian coordinates 1, 2 and 3)[71]:

$$\epsilon_{ik} \equiv \frac{1}{2} \left(\frac{\partial u_i(x)}{\partial x_k} + \frac{\partial u_k(x)}{\partial x_i} \right) \tag{3.1}$$

In a body whose microscopic arrangement is not in its state of equilibrium internal forces occur counteracting the thermodynamically unfavorable configuration. These forces are called *internal stresses*.

We now consider an infinitely small cubic volume ΔV (compare figure 3.1) in such a body. Forces acting in the inside of cube vanish due to Newton's third law of motion. Thus, only the forces acting on the cube's faces have to be accounted for. Using Gauss' theorem this statement is equivalent to the requirement that the integral on the ith component of the force density $\vec{\mathfrak{F}}$ over the volume ΔV can be replaced by a surface integral [79]. As a consequence, each force density component $\mathfrak{F}_i$ can be derived as divergence of a vector τ_i^b:

$$\mathfrak{F}_i = div\tau_i^b \tag{3.2}$$

Since this relation must be fulfilled for all force components, τ has to be a tensor of 2nd order. The total force $\vec{F}$ on the volume can then be written as

$$F_i = \int_{\Delta V} \mathfrak{F}_i dV = \oint \sum_{k=1}^{3} \tau_{ik}^b df_k. \tag{3.3}$$

Physically, the product $\sum_{k=1}^{3} \tau_{ik}^b df_k$ is equal to the ith component of the force on the surface element df. The diagonal elements of the *bulk stress tensor* τ^b describe normal stresses on the faces while the off-diagonal elements define shearing stresses.
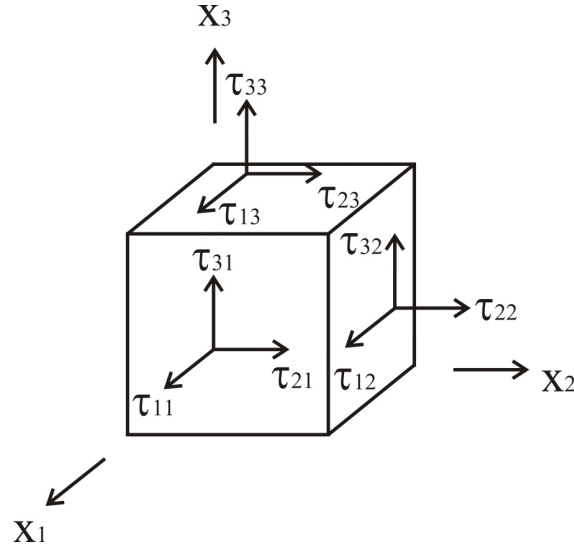
Figure 3.1.: **An infinitely small cube ΔV in a stressed solid.** Each face of the cube is under stress. The net force on a face is given by multiplication with the normal vector of the face. The sign conventions are indicated.

Their dimension is energy per unit volume.

The presence of intrinsic stress in the body implies that work must be performed to induce a displacement $\vec{u}$. Assuming small deformations, the *elastic energy* E_{el}^b can be derived in terms of strain ϵ and stress τ [75] as

$$E_{el}^b = \frac{1}{2} \int_{\Delta V} \sum_{ik} \tau_{ik} \epsilon_{ik} dV. \tag{3.4}$$

Stress as interface excess quantity

The elastic energy is an extensive quantity, i.e. it scales with system size [80]. Across an interface between two different phases A and B (with respective bulk elastic energies E_A and E_B), the local value of the elastic energy varies.

The integrated variation of the elastic energy across the interface δE_{el}^{int} is called the *excess* elastic energy. It is solely caused by the interface (compare figure 3.2) and is defined by [75]

$$\delta E_{el}^{int} \equiv \int_{interface} \int_{z_A}^{z_B} \sum_{ik} \tau_{ik}^b(\vec{r}) \delta\epsilon_{ik}^b(\vec{r}) dV - \sum_{ik} \left(\tau_{ik}^{bA} \delta\epsilon_{ik}^{bA} V^A + \tau_{ik}^{bB} \delta\epsilon_{ik}^{bB} V^B \right) \tag{3.5}$$

It is now useful to separate the stress and strain tensor in their components parallel ($\parallel$) and perpendicular ($\perp$) to the interface. For the following experiments
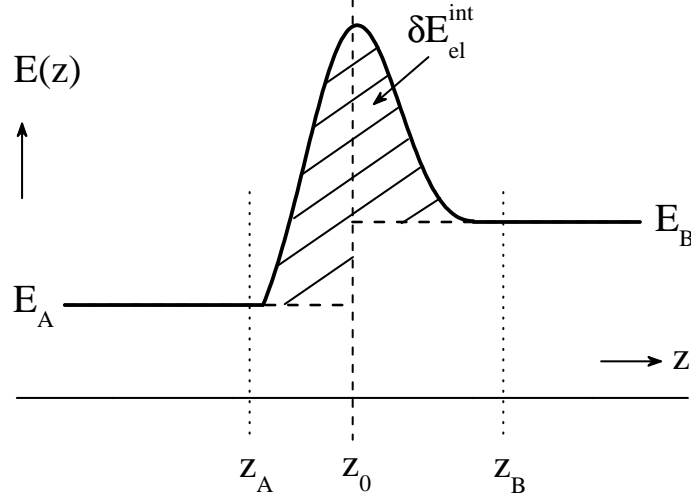
Figure 3.2.: **Elastic energy as interface excess quantity.** Two bulk materials A and B form an interface between points z_A and z_B over which the elastic energy varies from the bulk values. (Figure modified from [81])

two conditions [81] are valid, which significantly simplify the expression (3.5) [75]. First, it can be assumed that no relative gliding occurs between the phases A and B, i.e.

$$\delta\epsilon_\parallel^b(\vec{r}) = \delta\epsilon_\parallel^{bA} = \delta\epsilon_\parallel^{bB} \equiv \epsilon_\parallel^{int}, \tag{3.6}$$

and second, that the mechanical equilibrium is sustained. The latter leads to

$$\tau_\perp^b(\vec{r}) = \tau_\perp^{bA} = \tau_\perp^{bB} \equiv \tau_\perp^{int}. \tag{3.7}$$

Under these conditions the excess elastic energy given in equation (3.5) can be rewritten in the following form:

$$\delta E_{el}^{int} \quad = \quad \sum_{ik} \left(\epsilon_\parallel^{int} \tau_{ik}^{int} + \tau_\perp^{int} \epsilon_{ik}^{int} \right) S_{AB} \tag{3.8}$$

with

$$\tau_{ik}^{int} \quad \equiv \quad \frac{1}{S_{AB}} \left(\int_{interface} \int_{z_A}^{z_B} \tau_{ik,\parallel}^b(\vec{r}) dV - \tau_{ik,\parallel}^{bA} V^A - \tau_{ik,\parallel}^{bA} V^B \right), \tag{3.9}$$

$$\epsilon_{ik}^{int} \quad \equiv \quad \frac{1}{S_{AB}} \left(\int_{interface} \int_{z_A}^{z_B} \epsilon_{ik,\perp}^b(\vec{r}) dV - \epsilon_{ik,\perp}^{bA} V^A - \epsilon_{ik,\perp}^{bA} V^B \right), \tag{3.10}$$

and S_{AB} being the area of the interface. The definitions of the *interface stress*

τ_{ik}^{int} and *interface strain* ϵ_{ik}^{int} in equations (3.9) and (3.10) have the form of excess quantities. From a rigorous point of view, however, it has to be kept in mind that both are not extensive [75]. Their dimension is energy per unit area (eV/Å²) or, as frequently used in surface quantities, force per unit length (N/m).

Surface stress and strain

Surface stress τ_{ik}^{surf} and *surface strain* ϵ_{ik}^{surf} are included in the definition of the interface quantities by treating phase B as vacuum. Formally, one obtains "surface excess quantities":

$$\tau_{ik}^{surf} \equiv \frac{1}{S_A} \left(\iint_{surface} \int_{z_A}^{z_B} \tau_{ik,\parallel}^{b}(\vec{r}) dV - \tau_{ik,\parallel}^{bA} V^A \right) \qquad (3.11)$$

$$\epsilon_{ik}^{surf} \equiv \frac{1}{S_A} \left(\iint_{surface} \int_{z_A}^{z_B} \epsilon_{ik,\perp}^{b}(\vec{r}) dV - \epsilon_{ik,\perp}^{bA} V^A \right). \qquad (3.12)$$

Three remarks should be made at this point of discussion.

First, the definition of surface stress as given in equation (3.11) contains the one used by Ibach in his fundamental review paper [65]. If periodicity parallel to the surface can be assumed, the integration over the interface gets trivial. Since the choice of z_A and z_B is rather artificial in semi-infinite homogeneous phases, it is legitimate to set them to $\pm\infty$. Under these conditions one obtains his expression (labeled (1) in [65])

$$\tau_{ik}^{surf} = \int_{-\infty}^{\infty} (\tau_{ik}^{b}(z) - \tau_{ik}^{bA}) dz. \qquad (3.13)$$

Second, the presented derivation of surface stress demonstrates clearly what the cantilever bending method (see chapter 2.3) is actually sensitive to. It measures the change in in-plane stress ($\parallel$), i.e. change in "spring constants" in a toy-binding model, at the surface or interface.

Third, the surface stress τ^{surf} is a second-rank tensor according to the derivation. Nevertheless, it is diagonal if the crystallographic axes are respected in the actual experiments. The diagonal elements are degenerate at high symmetry surfaces. In this case, the surface stress can be treated as a scalar quantity. A sufficient condition for complete degeneracy is the existence of an at least three-fold symmetry axis on the surface [82, 83]. A scalar description of the Ag(111) surface is hence well-justified.

I will denominate surface stress with "τ" and surface stress change with "$\Delta\tau$" in this work and thus omit the "surf"-label for the sake of readability. Whenever necessary, the direction of the measured stress change is stated.

Tensile and compressive surface stress

An absolute positive surface stress indicates that the surface tends to shrink. Such a stress is called *tensile*. A surface favoring an expansion has an negative absolute surface stress and is called *compressive* [74]. Similarly, a reduction (an increase) in surface stress is called *compressive* (*tensile*), too. Nevertheless, it must be kept in mind that in differential measurements, conclusions on the absolute sign of the surface stress are only possible if the starting value is known (e.g. from ab initio calculations).

3.1.2. Energetic terminology at the surface

The fact that plastic and elastic deformations are not equivalent at a solid surface reflects physically in the existence of two surface quantities, namely *surface stress* τ and *specific surface free energy* γ. In this section, γ is defined, and the quantities are delimited from each other - but also a link is established by the *Shuttleworth equation*. These descriptive tools are essential for the elastic interpretation of chemical adsorption (chapter 3.2.2) and faceting (chapter 4.2).

Energy change associated with elastic deformations

Equation (3.8) gives the energy change when stretching an interface elastically. At a surface the normal component of the stress tensor vanishes as relaxation is possible in this direction, which further simplifies the expression. The change in elastic energy δE_{el} due to an infinitesimal strain $\delta\epsilon_{ik}$ can then be written for an isotropic surface of area A as

$$\delta E_{el} \;=\; \tau\delta\epsilon_{\parallel} \times A \tag{3.14}$$
$$=\; \tau\delta A. \tag{3.15}$$

According to the last expression, the surface stress τ corresponds to the reversible work per unit area to stretch a pre-existing surface elastically [83]. Stated otherwise, τ can be interpreted as the isothermal work per unit area against deformation [75].

Energy change associated with the generation of a surface

Stretching, however, is a different physical process as generating a surface under a constant strain, e.g. by cleavage. The latter process changes the free energy of the system, too. In analogy to expression (3.5), the free energy F^{surf} associated with the existence of a surface of area A can be defined as excess quantity of the bulk free energy F^b

$$F^{surf} \equiv \int_{-\infty}^{\infty} (F(z) - F^b)dz. \tag{3.16}$$

To enlarge or to reduce a surface by an infinitesimal amount dA at constant strain (i.e. by formally adding or subtracting surface atoms at equivalent places), the reversible work dw of

$$dw = \gamma dA \qquad (3.17)$$

has to be performed. Thus, the generation of a surface of area A requires a work W of

$$W = \gamma A. \qquad (3.18)$$

By definition, the latter expression is exactly the excess free energy measured with expression (3.16). Combining (3.16) and (3.18), one obtains

$$F^{surf} = \gamma A. \qquad (3.19)$$

As a consequence, γ can be identified as the *specific surface (Helmholtz) free energy* of the surface in question. γ must be positive for a surface to be stable. Otherwise, the system could gain energy by fragmentation.

The orientational dependence of $\gamma(\vec{n})$ ($\vec{n}$ being the surface normal) within a given crystalline structure determines the observed crystalline shape. Knowing the different specific free energy of possible surfaces, it is possible to predict the thermodynamically stable crystal surfaces by the Wulff-construction [84]. This quantity will be of particular use when discussing the physical origin of faceting in chapter 4.2.1.

The Shuttleworth equation

The specific free energy γ and the surface stress τ are, however, not completely independent. They are linked via the Shuttleworth equation [82]:

$$\tau_{ik} = \gamma \delta_{ik} + \frac{\partial \gamma}{\partial \epsilon_{ik}}. \qquad (3.20)$$

The *residual surface stress* $\partial\gamma/\partial\epsilon = \tau - \gamma$ (for isotropic) surfaces can be interpreted as a thermodynamic force driving atoms from the bulk to the surface [65]. It vanishes for liquids. In this case, τ and γ are hence identical and can be referred to as "surface tension" without danger of confusion.

3.2. Stress change in a chemisorptive system

Having defined surface stress, a short review of the understanding of the origin of surface stress will be given in the following chapter. I will focus on theoretical and experimental studies of clean transition metal surfaces. Thereon, chemisorption processes will be discussed. To remain within the scope of this thesis, the influence

of external fields on surface stress (reviewed e.g. in [58, 85]) will be omitted in the discussion.

3.2.1. Intrinsic stress of metal surfaces

The intrinsic surface stress of most investigated unreconstructed transition metal surfaces is tensile (see table 3.1). In this chapter I will briefly summarize the most important qualitative models in literature which try to explain the physical origin of the intrinsic stress. They provide a frame in which adsorption processes can be discussed. In addition, available theoretical and experimental data of the absolute values of transition metals are compiled.

Qualitative Models for the origin of surface stress

A perfect surface in bulk configuration can be virtually constructed by dividing a crystal along a plane parallel to the desired crystal direction and by removing all atoms and charges formally attributed to one fragment. The atoms at the newly formed surface are embedded in a different electronic environment than in the bulk. Therefore, their positions are energetically suboptimal. Nevertheless, they remain in lateral registry with the bulk positions in the absence of reconstruction. The virtual forces necessary to keep them in the unfavorable position can be identified as surface stress.

This gedankenexperiment is the common starting point of the models to be discussed. They differ, however, in their microscopic interpretation of the origin of surface stress.

Needs and coworkers [86] refer the tensile character to charge depletion in the surface layer. In a mean field picture, they assume that an optimum electronic charge density defines the optimum position of the ions. The charge density at the positions of a surface atom does not reach the optimal value because bonding partners are missing. The counteracting coulomb repulsion prevents a relaxation amongst the ions. As a consequence, tensile stress is built up.

Ibach [65, 87] uses the *Hellman-Feynman theorem* as starting point for a microscopic description. It claims that "all forces on the atomic nuclei originate from the coulomb forces of the electronic charge density and the nuclear charges" [87]. According to Ibach, extra charge accumulates in the topmost layers of the crystal surface because the charge of the unsaturated "dangling bonds" of the surface layer redistributes in the upper layers. As a consequence, the additional charge density strengthens the bonding. Perpendicular to the surface, the system is able to evade the induced stress by contraction, i.e. the topmost inter-layer distance shrinks. Within the surface plane, symmetry prohibits a stress relaxation. The resulting intrinsic stress favors a contraction, which is the definition of a tensile surface stress (see chapter 3.1.1).
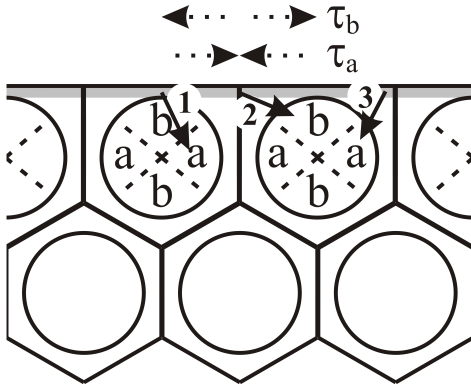
Figure 3.3.: **Heine-Marks-model.** At the surface, electrons deplete the grey-shaded area and flow into the attractive region around the core, the "core mantle", indicated by circles. An anisotropic charge redistribution leads to effective forces. Flows 1 and 3 into sectors **a** lead to tensile stress, while flow 2 into sectors **b** induces a compressive surface stress.
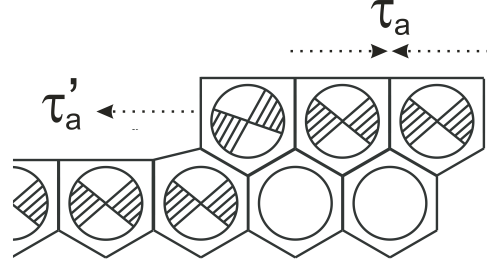
Figure 3.4.: **Defects in the Heine-Marks-model.** At a step the force partner is missing. Hence, the same charge distribution which induces tensile stress in the perfect surface of figure 3.3 leads to a compressive surface stress as depicted here.

For clean noble metal surfaces (Ag, Cu, Au), Heine and Marks [88] have developed a refined qualitative model. The d-bands are nominally completely filled for the noble metals inducing a pairwise repulsion between atoms. The delocalized electron-gas consisting of sp- and sp-d hybridized electrons see an effective attractive pseudopotential, leading to an "anomalously attractive region around the outer mantle of the core" [88]. These attractive and repulsive interactions balance in the bulk.

The attractive potential at the mantle of the core is a sharply localized "one-atom phenomenon" [88]. Therefore, it is preserved at the surface. But the charge in the free-electron gas which has been formally located at the surface redistributes into the attractive core region. According to the Hellman-Feynman theorem, the negative charge induces a force on the positive cores resulting in surface stress. Depending on its actual localization (compare figure 3.3), the net charge flow can lead either to a softening of the mutual in plane bonds (e.g. flow 2) or to a strengthening (e.g. flows 1 and 3). Both scenarios cannot be excluded from pure qualitative reasoning. Nevertheless, since experiments and ab-initio calculations reveal the overall stress character to be tensile for these materials (see following section), the second scenario (flows 1 and 3) can be assumed to dominate.

A defect leads to a surprising modification within the model, which can be seen

in figure 3.4. The same local charge redistribution which induces a tensile stress at the perfect planar terrace leads to a net expansive component. Therefore, its stress character is compressive. Hence, the actual local geometry on the sample surface can be expected to influence the overall surface stress.

Literature values for absolute surface stress

First-principles calculations have tried to improve the understanding and to provide more sophisticated models.

Several authors have performed population analyses of the charge difference of the surface and bulk layers. In general, their results seem to support a depletion picture. Nevertheless, the details of the results are in part contradictory. The employed approximations and the obtained final relaxed state of the systems influence the details strongly (compare, e.g., references [89, 90]).

Therefore, the compilation of calculated intrinsic surfaces stress shown in table 3.1 also shows a large scattering in the absolute values of the intrinsic surface stress of a large variety of metal surfaces. Nevertheless, all values have in common that the intrinsic surface stress of the metals is positive, thus tensile.

The experimental access to the absolute value of the surface stress has not yet been accomplished with high precision. Values given in literature are determined by the following idea: The lattice constant of elemental clusters and nanoparticles varies from the respective bulk value a. Interpreting this deformation in an elastic and isotropic picture, it is caused by the hydrostatic pressure p using $\Delta V/V = -\kappa p$, with κ being the bulk compressibility. Assuming spherical particles with radius r the pressure can be related to the (isotropic) surface stress τ by $p = 2\tau/r$. Combining those two relations one obtains

$$\tau = -\frac{3}{2}\frac{\Delta a}{a}\frac{\kappa}{r} \tag{3.21}$$

which is the "master equation" for the experimental determination of the absolute values of surface stress established by Mays et al. [99]. A number of authors have used different methods to produce clusters and deposit them on suitable substrates or matrix materials. To measure the deviation in lattice constants, high resolution electron microscopy (HREM), transmission electron microscopy (TEM) in combination with electron diffraction (ED) and extended x-ray-absorption fine-structure (EXAFS) have been used. The results obtained for metallic particles are compiled in table 3.2.

The method, however, contains systematic errors to be aware of. First of all, equation (3.21) neglects completely the anisotropic nature of surface stress. Furthermore, in principle, a single specific surface orientation cannot be found on an imaginary perfectly spherical particle. But at lower temperatures, the thermodynamically stable surfaces will dominate the crystal shape. Therefore, the measured

Table 3.1.: **Compilation of theoretical intrinsic surface stress of metals.**

Surface	Surface stress τ [meV/Å^2]									$\tilde{\tau}$ [a]
Reference	[92]	[90]	[93]	[94]	[86]	[95]	[96]	[97]	[98]	[89]
Al(111)				145	78					
Al(110)$_{[001]}$				115						
Al(110)$_{[\bar{1}10]}$				124						
Ni(111)									27	
Ni(100)									79.3	
Cu(111)									54	
Cu(100)									86.1	
Y(0001)	62.4	38								
Zr(0001)	139	98.0								
Nb(100)	55.6	112								
Nb(110)$_{av.}$	187	215								
Mo(100)	124	204								
Mo(110)$_{av.}$	185	259								
Tc(0001)	162	217								
Ru(0001)	197	297								
Rh(111)	170	132	242							
Rh(100)	147	134								536
Rh(110)$_{av.}$		58								
Pd(111)	160	134	193					230		
Pd(100)	135	106								278
Pd(110)$_{[1\bar{1}0]}$								171		
Pd(110)$_{[001]}$								116		
Pd(110)$_{av.}$		42								
Ag(111)	49	47	109						40	
Ag(100)	81.8	55							51	211
Ag(110)$_{av.}$		27								
Ir(111)			312			331				
Ir(100)										798
Pt(111)			234			350		422	179	
Pt(100)									168	699
Pt(110)$_{[1\bar{1}0]}$								317		
Pt(110)$_{[001]}$								113		
Au(111)			160			173	207.0		94.3	
Au(100)							170.0		112	340
Au(110)$_{av.}$							126.1			
method	GGA-PAW	GGA-EMTO	LDA-EMTO	LDA-Pseudopotential				LCAO	EAM	LDA-LMTO

[a]Transferred into meV/Å^2 with the help of structure parameters from reference [91]. The surface stress definition by Fiorentini et al. [89] is not equivalent to the conventional one (3.11).

Table 3.2.: **Compilation of experimental absolute surface stress of metals.** The decisive experimental parameters are added to the measured surface stress in order to ease the comparison.

material	free particles	embedded particles		
	τ [meV/Å²] (particle diameter range [Å])			
Ni	0 ± 28 (12-92)[101]			
Cu		270 ± 240[100]ᵃ (40-48)		
Pd		710 ± 380 (40-45)[100]		
Ag	88 ± 19 (30-178)[103]	375 ± 56 (14-50)[102]		
	373 ± 56 (60)[107]	338 ± 69 (13-45)[105]	119 ± 75 (30-140)[106]	
	143 ± 13 (25-130)[104]			
Pt	161 ± 25 (19-122)[101]			
Au	73 ± 6 (≥30)[99]	394 ± 63 (14-50)[108]		
method	TEM & ED	EXAFS	EXAFS	TEM & ED	HREM
Host matrix	none	Ar	am. Cᵇ	polymer	glass
substrate	am. C	Al	am. C	polymer	glass
T [K]	321 - 338	4.2	-	-	300

ᵃApai et al. [100] do not explicitly deduce the surface stress from their structure data. The values given here have been derived from the published dilatation using expression (3.21).

ᵇamorphous carbon

30

stresses are often compared to the stresses calculated for the (111)-surfaces [90]. More realistic model particles show a much better agreement with the experimental values [109].

A correct interpretation of the experimental results is furthermore complicated by the fact, that the measured particles interact with the substrate or with the surrounding matrix material. Therefore, the observed stress is more precisely the interface stress in the investigated system and not the surface stress of the system in question. Hence, the host environment of the investigated particles is included in table 3.2. Finally, the width of the particle size distribution can lead to large errors in the determined surface stress.

In summary, one can still draw two major conclusions from the data in table 3.2. First, the experiments confirm the intrinsic surface stress in metals to be positive and second, the results support the order of magnitude of the theoretical values.

3.2.2. Surface stress change induced by chemisorption

All microscopic surface stress models explain the existence of surface stress with the specific electronic configuration at the surface. Charge transfer during chemisorption modifies the charge distribution. Thus, surface stress should change upon adsorption. In the following paragraphs I will discuss these consequences for the intrinsic surface stress of metals using the different frameworks introduced in chapter 3.2.1. Furthermore, a simple expression for the coverage dependence of surface stress is derived, and finally, the impact of structural transitions discussed.

Chemisorption in the microscopic models

When adsorbing, electron acceptors withdraw charge density from the "strengthened bonds" according to the Ibach model [65, 87] (see chapter 3.2.1). As a consequence, the intrinsic tensile surface stress of the metal surface is reduced, and a compressive stress change is observed in the experiment. In the contrary, electron donors enhance the bonding in this picture and therefore induce a tensile stress change. The formally charged adsorbates repel each other in this model adding a compressive contribution to the system.

Heine and Marks argue similarly. They suppose for noble metals that the charge transfer in a chemisorptive adsorption process increases or decreases the charge density in the mantle region [88, 110] (compare figures 3.3 and 3.4). Adsorption of an electron acceptor on a perfectly flat noble metal surface would therefore relieve the intrinsic surface stress. But the consequences of an increased electronic density at the core mantle are less straightforward to predict. The specific geometric configuration of the charge distribution enters into their model and determines the mesoscopic character of the Hellman-Feynman-forces. General assumptions on the localization of the additional charge cannot be made.

Although the concept might appear more sophisticated, the systematics are the same if one argues with charge depletion: Charge donors can be seen to restore in part the depleted charge density and increase the repulsive Pauli pressure in the topmost layers [74, 111]. As a consequence, charge donating adsorbates should reduce the intrinsic tensile surface stress while charge withdrawing adsorbates lead to an increase.

In general, arguments purely based on electronegativity are rather intuitive and moreover, very successful in explaining the tendency in most of the experiments [65, 74, 75]. Nevertheless, their simplifications may lead to wrong predictions as Feibelman has demonstrated for the adsorption of hydrogen on Pt(111) [111].

Analytical coverage dependence

Surface stress change upon adsorption is experimentally accessible with the help of the cantilever-bending-technique discussed in chapter 2.3. It is instructive to consider not only the sign of a stress change but also to think about the analytical form of the coverage dependence of the surface stress change.

A heuristic derivation of that dependence has been first proposed by Ibach [87]: Since each adsorbate atom changes the local electronic environment equally, a linear dependence on coverage can be expected to first approximation. The linear dependence gets modified by an exponential term growing with the average adsorbate distance (i.e. with the square root of the coverage $\sqrt{\Theta}$). The correction term subsumes interactions induced by the growing overlap of wave functions of adsorbate atoms and changes in the band structure at higher charge transfer. In total, one obtains the following functional form for the surface stress change dependence during pure adsorption:

$$\Delta\tau = a\Theta + be^{-c/\sqrt{\Theta}} \tag{3.22}$$

with a, b and c being system-dependent constants. A more formal derivation of (3.22) has been demonstrated for special cases with the help of the Shuttleworth equation (3.20) in reference [75].

For completeness, it should be noted that the nonlinear coverage dependence has also been reproduced in one dimension by continuum theory modeling [112] if a strain-dependent interaction energy is assumed. A complete analytical derivation of the coverage dependence, however, is still to be found because the underlying physics is highly complex.

Surface stress and structural phase transitions

It is a well-known fact that adsorbates can induce structural phase transitions in the substrate. The particular reconstruction often depends on the experimental parameters temperature and coverage. There are a few studies in literature which have investigated these reconstructions with the cantilever technique (chapter 2.3)

to gain insight into the behavior and the role of surface stress. In this section, I will discuss two examples: the O/Cu(100) and C/Ni(100) interfaces. Systems in which a large-scale (i.e. mesoscopic) structural phase transition occurs by self-organization will be discussed separately in chapter 4.2.

Temperature-dependent structural phase transitions cannot be studied in a single measurement due to the thermal instability of the cantilever setup (see chapter 2.3). The respective phases must be isothermally measured in independent experiments whose results can then be compared. Harrison et al. [113] have performed such stress change measurements during the adsorption of oxygen on Cu(100). Two different structural phases can be obtained, depending on the preparation temperature. At 300 K, a c(2x2) superstructure is formed, while at 500 K the system forms a missing-row reconstruction. In the first case, the authors observe a compressive surface stress change of -1.0 N/m. But the surface stress changes only by -0.6 N/m if the system reconstructs. According to Harrison and coworkers, the system evades the absolute compressive surface stress built in the c(2x2) superstructure by "choosing" to reconstruct. The authors can support that view with DFT calculations [58, 113].

According to the arguments of the last paragraphs, the surface stress $\Delta\tau$ should basically change monotonously with coverage in the sub-monolayer regime. Nevertheless, there are studies on systems undergoing a structural phase transition in which the surface stress changes completely differently.

Sander et al. [114] have investigated the adsorption of carbon on Ni(100). In their surface stress measurements they observe a very pronounced compressive stress change during the initial adsorption of carbon. But at a coverage of 30% of a monolayer (ML) of carbon, the slope of the surface stress change curve flattens. The authors could correlate the onset with the beginning of a structural transition: In this system, the topmost Ni-layer alters resulting in a p4g-reconstruction. A number of structural investigations (see e.g. Kilcoyne et al. [115]) have shown that the next neighbor-distance of the Ni-atoms is enlarged as a consequence. The greater distance between the Ni-nuclei reduces compressive stress. As a conclusion, the structural transition has been interpreted as the channel of the system to evade the growing massive compressive surface stress. (Recent ab-initio calculations, however, identify other electronic effects as driving forces [116, 117]. The fact that the discussion is not settled after fifteen years underlines the complexity of the problem.)

Nevertheless, similar observations of "unconventional" coverage-dependencies associated with structural phase transitions have been made for the C/Ni(111)-interface [118] and for the formation of a self-assembled monolayer (SAM) of alkanethiols on Au(111) [119]. These studies have established that deviations from equation (3.22) in the sub-monolayer coverages can be referred to a structural phase transition. But although such a behavior gives evidence for the intimate relation between surface stress change and structural phase transitions, the final

proof whether the transition is actually driven by surface stress can only be made based on the knowledge of the absolute surface stress [66].

3.2.3. Surface stress change by organic molecules

In this section, the surface stress change of systems with large organic molecular adsorbents will be discussed. New degrees of freedom influence the surface stress at these interfaces. After reviewing the previous work on the subject, the major questions will be deduced and thus the experimental studies of this work motivated.

Literature review

Surface stress change upon adsorption of large organic molecules has only been studied for two systems under UHV conditions.

A number of groups have investigated the change in surface stress upon formation of a self-assembled monolayers (SAM) of alkanethiols on evaporated gold films. In this system, the sulphur head group covalently binds to a surface gold atom, thus forming a highly localized bond. In most cases, the "micromechanical cantilever" technique introduced by Berger et al. [120] has been used, only Shrotriya et al. [121] use an interferometric setup. The former method, however, differs significantly from the cantilever technique discussed in chapter 2.3. The basis of the employed detection systems are V-shaped SiN_x cantilevers with microscopic dimensions whose curvatures are monitored. As receptor layer, a thin (approx. 20 nm) gold film is evaporated on one side of the substrate.

As can be seen in table 3.3, a chain-length-dependent compressive change in surface stress is measured. But the results show a spread of three orders of magnitude ranging from -0.1 N/m up to -16 N/m. The large variance has several reasons: Godin et al. [119] have realized that the different structural phases (flat-lying, up-right standing molecules and mixtures thereof [125]) are characterized by completely different stress regimes. The polymorphism of the system is hence the prime reason for the wide distribution of the experimental results.

In addition, experimental factors explain some uncertainty of the determined absolute stress change values, too. First, the cleaning treatment of the gold substrate has been demonstrated to influence the measured stress change [123]. Furthermore, the often unclear grain sizes of the polycrystalline gold film exacerbate the comparison of different experiments [119]. Besides, the curvature change is often interpreted using exactly the equation by Stoney [65] (only Godin et al. [119] use a modified expression). But the V-shaped microcantilevers of sub-micron thickness resemble only in a limited manner the rectangular plates for which Stoney derived his expression. Finally, it is not clear which elastic constants have to be chosen for the layered SiN_x/Au cantilever. Modifications to Stoney's equation that are better

Table 3.3.: **Surface stress change measured for organic adsorbates.** The published data on systems investigated under UHV conditions is summarized.

Adsorbate system	Surface stress change $\Delta\tau$ [N/m]
SAMs/Au(111)	
HS-$(CH_2)_3$-CH_3/Au(111)	-0.08 ± 0.02 [120, 122]
HS-$(CH_2)_5$-CH_3/Au(111)	-0.10 ± 0.02 [120, 122], -0.8 to -0.05 [123]
HS-$(CH_2)_7$-CH_3/Au(111)	-0.15 ± 0.02 [120, 122]
HS-$(CH_2)_{11}$-CH_3/Au(111)	-0.19 ± 0.02 [120, 122]
	-0.51 ± 0.02 [119], -15.9 ± 0.6 [119]
HS-$(CH_2)_{15}$-CH_3/Au(111)	-0.08 ± 0.02 [120, 122]
HS-$(CH_2)_{17}$-CH_3/Au(111)	-0.15 to -0.12 [121]
Alkanes/Au(111)	
CH_3-$(CH_2)_{15}$-CH_3/Au(111)	"negligible"[a] [120, 122]
aromatic molecules	
pentacene/Si(111)-(7x7)	-0.1 [124]

[a]The system is used as baseline reference in the study.

applicable to microcantilevers can be found, e.g., in references [126–128][1].

The second system studied might be more useful as a reference. Kury et al. [124] have reported on the change of surface stress upon the adsorption of pentacene on the reconstructed Si(111)-(7x7) surface. At this interface, the aromatic molecules form a wetting layer of flat-lying molecules whose bonding is covalent and highly localized at the central aromatic ring. The aromatic rings which are not involved in the bonding tilt away from the surface. This leads to a geometry which can be described as an "inverted umbrella" [124]. It leaves the adsorbate the freedom to rotate and to align freely within the substrate unit cell. According to Kury et al., the geometry yields a "maximum substrate passivation accompanied by a minimal adsorbate-substrate interaction" [124]. The surface stress changes only slightly by -0.1 N/m. The authors conclude the interaction strength to be insufficient to lift the Si(7 x 7)-reconstruction. As a consequence, they interpret the pentacene molecules to bury the reconstructed interface. Furthermore, a first insight into the

---

[1]In fact, a precise absolute value is not really the prime goal of the microcantilever technique. Its fascinating applications exploit another effect already discussed in Berger's original publication [120]. The surface stress of the SAM-gold interface can be modified by additional adsorbates bonding to the SAM-molecules. If the tail (alkyl-) group of the alkane chains is chemically replaced with a functional group, the bending gets chemically sensitive. Following this route, micromechanical "artificial noses" [129] are designed for numerous applications (see e.g. [130, 131]).

strength scale of pure intermolecular interaction has been gained. The data assigns each additional pentacene layer a surface stress change of -0.015 N/m which is of remarkably small magnitude.

Conclusions and open questions

The studies discussed in the previous paragraphs already indicate some properties which make the investigation of stress change at organic hybrid interfaces a demanding and yet very promising enterprize.

First of all, the magnitude of the surface stress change is still completely unclear considering the large variance of the observed values. The systems studied so far are all characterized by highly localized covalent bonds. Thus, they are chemically not that different from inorganic (mostly monoatomic) adsorbate systems. Yet most of the measured stress changes are orders of magnitude smaller than the one observed in purely inorganic adsorbate systems.

Furthermore, the bonding at organic-metal interfaces is usually much more complex than in the case of the examples discussed in literature before. This is especially true if large aromatic molecules are involved. In general, these systems form delocalized chemical bonds. The induced change of surface stress could be completely negligible.

Moreover, in contrast to atomic adsorbates, large molecules are able to distort themselves. This has already been observed for a number of adsorbates [132, 133]. As argued in the pentacene/Si(111)-(7x7) system [124], such a distortion could be suspected to promote a local compensation path for elastic stress and thus prevent the formation of large-scale strain fields.

Stated otherwise, the question of relevance of surface stress change at organic hybrid interfaces is unanswered yet. But the elastic quantity surface stress change provides additional information on such an interface which is in part complementary to the often known electronic and geometric properties. Hence, its knowledge would indeed improve the general understanding of these interfaces.

Nevertheless, for a systematic study of the surface stress change at organic-metal interfaces a well-defined adsorbate system has to be chosen in order to evade the problems of the alkanethiol/Au(111) studies.

3.3. The archetype system PTCDA/Ag(111)

As a model interface for large aromatic molecules on noble metal surfaces, I have investigated the surface stress change during the adsorption of 3,4,9,10-perylene-tetracarboxylic-dianhydride (PTCDA, structure formula given in figure 3.5a) on Ag(111). The system is very suitable for such a pioneering experiment since its properties are very thoroughly studied. Hence, a number of reviews are available in

literature [23, 134–138]. The focus of this chapter is on aspects of the geometric and electronic structure which are necessary to understand the experiment and which might influence the surface stress in the system based on the general principles discussed in the previous sections.

Thin film growth mode

PTCDA films of several Ångstrøms of thickness differ in their morphology and structure significantly. The growth mode depends strongly on the growth parameters, but especially on the growth temperature [139, 140].

At and below room temperature homogeneous films can be grown. Their roughness increases with decreasing temperature [139]. The unit mesh parallel to the surface differs slightly from those of the two bulk phases of PTCDA in the Franck-van-der-Merve growth mode. It resembles the unit cell dimensions found in the PTCDA monolayer on Ag(111) (see below). The strained crystalline growth induces compressive stress into the layers [139, 141].

At elevated temperatures (approximately above 350 K) the growth mode changes. The first two layers still grow strictly layer-by-layer [44], both layers in commensurate registry with the substrate [141]. Large molecular crystallites form on top of this double wetting layer[44, 140]. Their structure is (within thermal expansion) identical to the structure of the bulk phases of PTCDA [139, 141].

Molecules built in higher layers start to desorb at substrate temperatures of approximately 480 K. The second molecular layer desorbs only above 540 K [141]. In contrast, the molecules forming the first molecular layer on top of the substrate, i.e. the monolayer, cannot be desorbed intactly.

Geometric structure of the monolayer

The structure of the monolayer phase of PTCDA on Ag(111) has been analyzed with great care and with a large number of different methods for almost two decades. In conclusion, a detailed model has been developed. It is presented in the following paragraphs. A brief graphic summary can be found in figures 3.5b and c.

The molecules adsorb flat-lying, i.e. parallel to the metal surface [145, 146]. Substrate steps are decorated first. At their lower edge, large islands nucleate with a well-ordered commensurate superstructure [142]. Only few domain boundaries are observed on large terraces despite the large number of 198 possible domains [136]. The respective superstructure matrix

$$S_A = \begin{pmatrix} 6 & 1 \\ -3 & 5 \end{pmatrix} \tag{3.23}$$

describes an almost rectangular unit cell whose base vectors intercept under 89.0° [142] (compare figure 3.5b). It resembles the unit cells found in the (102)-planes of

a)

b)

PTCDA

[10$\bar{1}$]

89°

18°

[0$\bar{1}$1]

c)

(2.97 ± 0.06) Å
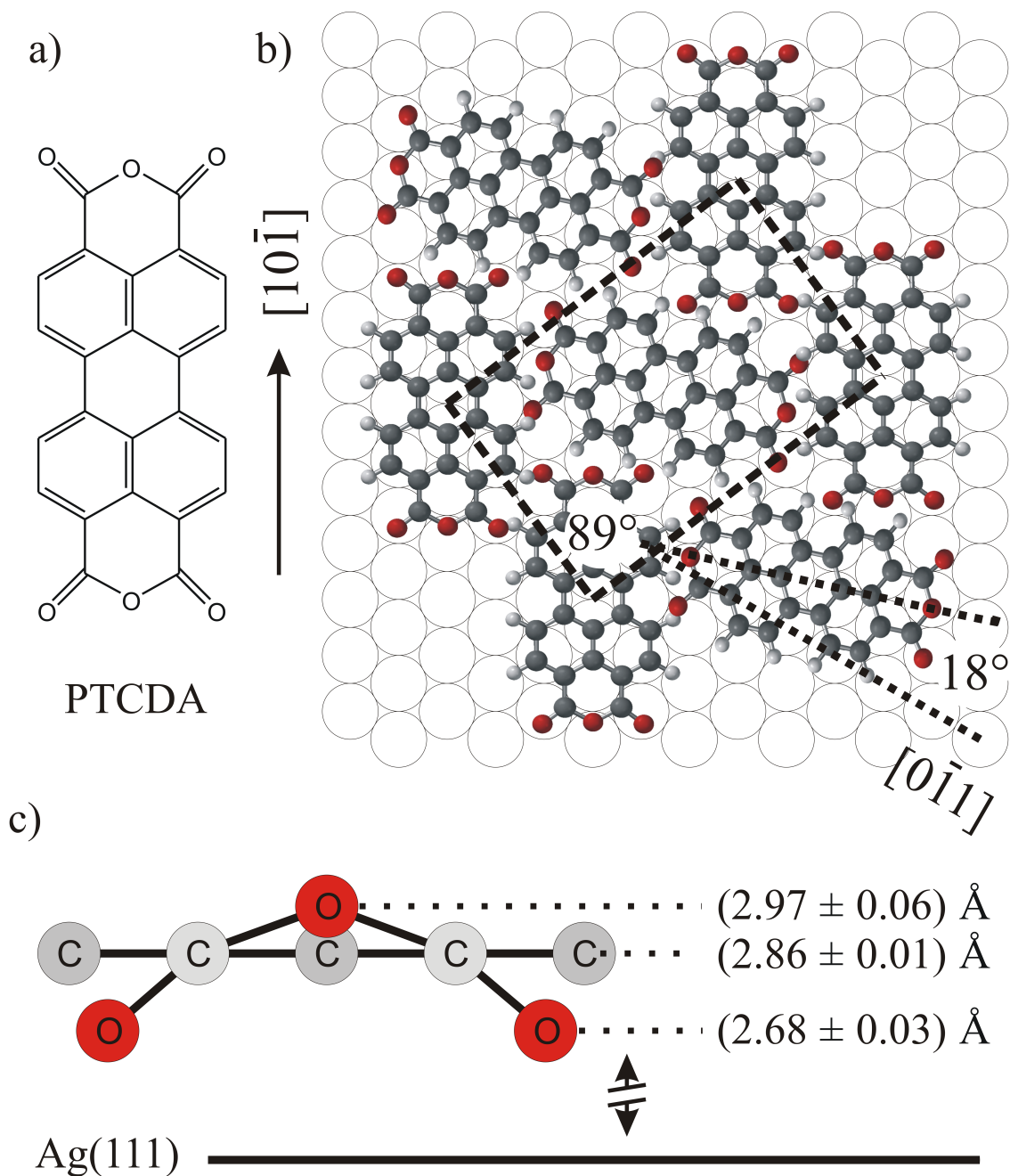(2.86 ± 0.01) Å

(2.68 ± 0.03) Å

Ag(111)

Figure 3.5.: The monolayer structure of PTCDA on Ag(111). a) structure formula of 3,4,9,10-perylene-tetracarboxylic-dianhydride (PTCDA) b) structure model of the PTCDA/Ag(111) monolayer unit cell [142, 143] c) average vertical distortion of the chemisorbed PTCDA molecule on Ag(111) [132, 144]

the two crystalline phases of PTCDA. Compared to the α-phase, the area covered is enlarged by 0.25%, while the aspect ratio deviates by 11%. The dimensions are even closer to those observed in the β-phase since the difference in aspect ratio amounts to only 3.3%. The observed interface unit cell is compressed by 0.67% compared to the latter structure in this case [141] .

Microscopically, one unit cell covers 33 silver atoms and contains two PTCDA molecules. They are arranged in a herringbone structure, which is presumably induced by mutual electrostatic interactions due to the inherent molecular quadrupole moment [142]. Both molecules are centered on bridge positions [143]. The long axis of the first molecule is aligned along the [10$\bar{1}$]-direction, while the second molecule is rotated by 18° with respect to the [0$\bar{1}$1] of the substrate direction [143].

Beyond the lateral configuration, further information has been gathered on the vertical geometry. In average, the molecules are positioned (2.85 ± 0.10) Å above the last silver atom layer [147]. Looking closely, however, the molecules do not adsorb absolutely flatly but significantly distortedly. The oxygen atoms bent out of the plane of the carbon core, which is depicted in figure 3.5c: The anhydride oxygens are tilted upwards to an absolute height of 2.97 Å, while the carboxylic oxygens bend downwards to an absolute height of 2.68 Å [132, 144, 148, 149].

Little information has been gathered on geometrical changes in the silver substrate upon the PTCDA monolayer formation on Ag(111). Experimental data is missing completely. In a first-principle calculation, only small relaxations (i.e. deviations to the position at the clean surface below 0.05 Å) of the silver atom positions have been observed [150].

Bonding of the monolayer

As mentioned before, the molecules in the monolayer are strongly bound to the metal and cannot be desorbed intactly [141, 151]. The binding energy E_{bin} of the monolayer has hence not yet been determined experimentally. Binding energy values which have been derived by ab initio calculations [13, 150, 152] vary between values smaller than 0.1 eV and 3 eV per molecule (see table 3.4).

The chemisorptive nature of the bonding of the PTCDA monolayer on Ag(111) is, however, well established as the result of a complex interplay of different mechanisms. A large variety of spectroscopic studies reveal the perylene core to play a decisive role in the bonding [151, 153]. In particular, the frontier molecular orbitals HOMO and LUMO (highest occupied and lowest unoccupied molecular orbital) hybridize with the Ag5s states [151]. As a consequence, the former LUMO (F-LUMO) is filled in part and therefore pulled down below the Fermi level [151] inducing a "metallic" character to the molecular film [154]. The charge transfer is apparently balanced in part by charge back-donation involving the former HOMO and former HOMO-1 states [151].

In addition to these rather delocalized bonding mechanisms, the distortion of

Table 3.4.: **Theoretical bonding parameters.** Binding energy E_{bin} per molecule, net charge transfer from metal into molecules, and adsorption height at the PTCDA/Ag(111)-interface as derived by first principle methods.

Method	E_{bin} [eV/molecule]	charge transfer [e]	adsorption height [Å]
LDA [150]	3	0.35	2.8
GGA-PBE [152]	< 0.1	-	3.5
GGA-PW91 [13]	0.5	negligible	3.2

the PTCDA molecules [132, 144] indicates the carboxylic oxygens to form localized covalent bonds to specific silver atoms. Several ab initio studies underline their importance [13, 148, 149]. Du et al. [13] even claim the latter to be the sole binding mechanism in the system. The latter interpretation, however, cannot explain the fact that the comparison between multilayer and monolayer near edge x-ray adsorption fine structure (NEXAFS) spectra of the interface [145, 151] reveal large differences in the spectral structures associated with the perylene core. But features associated with the anhydride groups change only slightly [155]. The model by Rohlfing et al. [150] suggests that both binding mechanisms enhance each other mutually.

Nevertheless, in total, the observed work function shift of only 0.1 eV between clean substrate and monolayer interface characterizes the net charge transfer to be small [151]. This finding is corroborated by theoretical calculations (see table 3.4).

In order to obtain a complete picture of the bonding, not only adsorbate-substrate but also inter-adsorbate interactions have to be considered. Four different intermolecular interaction pathes are possible (and indistinguishable): "conventional" molecular lateral covalent bonding, van-der-Waals interactions, electrostatic interactions due to the quadrupole moment, and indirect substrate mediated interactions [156]. Their strength has been argued to promote band formation within the molecular layer [157]. But recent 2PPE-experiments indicate the respective experimental observation to be a substrate property and not one of the molecular layer [158]. Nevertheless, there is strong evidence that intermolecular interactions both stabilize the metastable low temperature phase and promote the formation of the stable herringbone structure at room temperature [156].

3.4. Measured surface stress change

The change of surface stress has been measured during the adsorption of one monolayer of PTCDA on Ag(111) kept at a substrate temperature of (550 ± 0.1) K. The sample was exposed to PTCDA molecules for 500 s. According to the calibra-
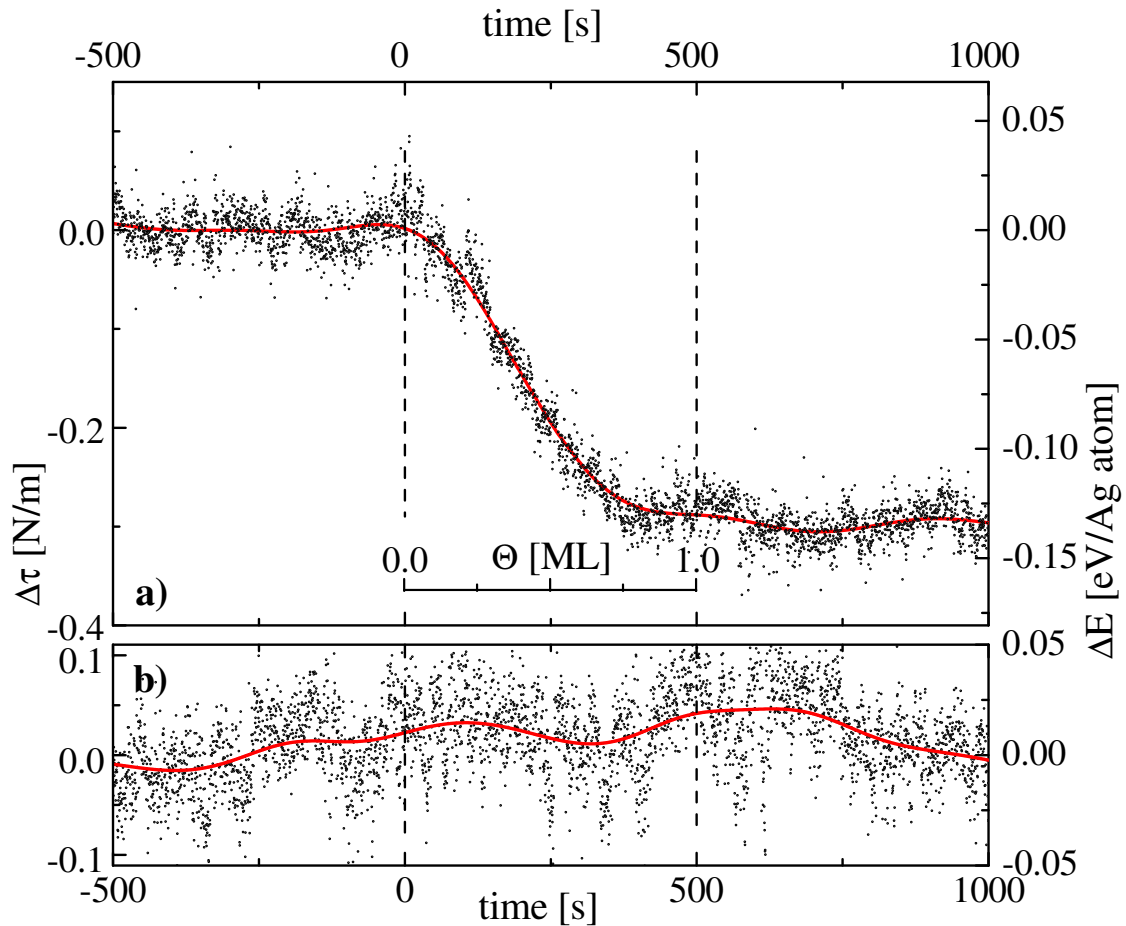
Figure 3.6.: **Surface stress change during the formation of the PTCDA/Ag(111) interface. a)** The Ag(111) cantilever is exposed to PTCDA-molecules between 0 and 500 s (indicated by dashed lines) while being kept at 550 K. The dots represent averaged measurement points while the red line has been smoothed by a Gaussian convolution. The inserted extra scale gives the corresponding PTCDA coverage Θ. **b)** Reference experiment to demonstrate the stability of the system.

tion, this exposure time leads to a coverage of one monolayer, which has been confirmed after each experiment with XPS. As mentioned in chapter 3.3, the adsorbed molecules are highly mobile under these conditions and form the ordered herringbone structure. Therefore, these growth conditions are suitable for an in-situ experiment.

Although the measured surface stress change is definitely at the limit of the resolution of the technique, the recorded data curves are nicely reproducible. Data points of three cantilever measurements have been averaged to obtain the data set shown in figure 3.6a. The surface stress τ changes immediately after opening the shutter. It decreases, i.e. the chemisorption of PTCDA induces a compressive surface stress change. Up to approximately 75% of a monolayer coverage, the surface stress drops almost linearly. For higher coverages, however, no further change is observed. After the shutter has been closed, the surface stress does not alter any more. The system has been checked with great care to remain stable for over an hour (not shown here) after shutter closing.

Overall, the surface stress changes by (-0.30 ± 0.03) N/m or (-19 ± 2) meV/Å^2. This value translates by multiplication with the average area per silver atom of 7.23 Å^2 into an average change in surface energy of (-140 ± 10) meV per silver atom. It is even more instructive to scale the surface stress change with the large area ascribed to a PTCDA molecule within the herringbone structure. Multiplying with 119.35 Å^2 [141], one obtains an energy change of (-2.2 ± 0.2) eV per PTCDA molecule. The error bar has been chosen to contain 90% of the data points.

According to the validation experiment depicted in figure 3.6b, this value can indeed be solely attributed to the adsorption process. The data, taken under exactly the same experimental conditions upon exposure of the passivated surface, demonstrate that the measured signal does not change without adsorption of PTCDA molecules.

It should finally be noted that the growth of the known herringbone superstructure [142] has been confirmed during each experiment using both LEED and XPS characterization. The coverage scale has been calibrated using XPS reference experiments. Its linearity has been tested for several partial coverages.

3.5. Discussion

In this section the stress change curve (figure 3.6) will be exploited to gain further insight into the PTCDA/Ag(111) interface. The sources of surface stress change can be manifold and are not straightforward to disentangle, especially without theoretical support. Nevertheless, fundamental qualitative and even semi-quantitative results can be deduced following the approaches discussed in chapter 3.2.2.

3.5.1. The absolute value of $\Delta\tau$

The primary result of the measurement is that the overall surface stress change upon adsorption of PTCDA on Ag(111) is negative, i.e. compressive. The magnitude of (-0.30 ± 0.03) N/m appears rather small compared to values measured for atomic carbon adsorption or the adsorption of small molecules. Surface stress changes of -4.0 N/m and -6.3 N/m have been measured, for example, for systems like CO/Pt(111) or C/Ni(100), respectively [65]. The value, however, fits to the general trend of smaller stress changes in organic adsorbate systems, which can be deduced from the studies compiled in table 3.3.

Nevertheless, it is premature to categorize the surface stress change in the system as small based on previous references. When considering the magnitude of surface stress change for PTCDA on Ag(111), one should in particular be aware of two points:

First, the intrinsic tensile stress of Ag(111) is in the order of 40 to 110 meV/Å^2, according to the references compiled in tables 3.1 and 3.2. The surface stress change induced by adsorption of PTCDA amounts to (19 ± 2) meV/Å^2. Therefore, the observed induced stress change is *of the same order as the intrinsic surface stress of the substrate.*

Second, it is very instructive to normalize the measured surface stress change to the average area per molecule. As already demonstrated in chapter 3.4, a $\Delta\tau$ of (2.2 ± 0.2) eV can be assigned to each molecule. In order to qualify that number, it can be compared to the theoretical binding energies compiled in table 3.4. In fact, the measured stress change is of the same order as the binding energy. Hence, without overstretching this comparison, it can be stated that the change in elastic interaction is also *of the same order as the strength of the chemical interaction.*

Therefore, the observed change of surface stress $\Delta\tau$ is significant on both inherent scales of the system: the intrinsic surface stress of the metal and the molecule-substrate interaction.

Beyond establishing the relevance of the quantity, the magnitude of the surface stress change also reveals clues on its microscopic origin.

Berger et al. [120] attribute the stress change in their organic adsorbate system to electrostatic interactions between molecular dipoles. For PTCDA/Ag(111), however, the net charge transfer is considered to be relatively small. Moreover, in contrast to Berger's SAMs, the molecules adsorb flat-lying, reducing the effective length and thus the strength of the image dipoles. Besides, the inherent quadrupole moment of the molecules is also almost completely compensated and screened by the resulting image dipole in the metal and by the charge transfer in the system. Considering that for simpler systems with larger charge transfer the magnitude of the electrostatic interactions has been estimated to be in the order of 10^{-3} N/m [87], a mere electrostatic explanation of the elastic interaction appears improbable. Nevertheless, it still contributes to the overall stress change.

In addition, the intermolecular interactions induce a change of the surface stress of the system. The dimensions of the superstructure cell are in between those of the equilibrium crystallographic α- and β-phases. Thus, a general argument on the tensile or compressive nature of the molecular configuration is not possible. But a net attractive interaction amongst the PTCDA-molecules as suggested by Kilian et al. [156] induces a compressive stress change in agreement with the experimental result. Kury et al. [124] have determined the stress change to be on the order of 0.02 N/m per molecular layer during the formation of pentacene crystallites. Considering this result as a scale for intermolecular elastic interactions, the distortion of the molecular arrangement cannot account for the measured stress change in the system either.

The best qualitative comprehension of the magnitude and sign of $\Delta\tau$ can be achieved by considering the interface formation as a typical chemisorptive process on a noble metal surface following the general concepts developed by Heine, Marks, and Ibach (see chapter 3.2.2). The charge reconfiguration in the topmost layers of Ag(111) releases in part the intrinsic tensile surface stress of the metal. As a consequence, a compressive stress change is measured (although the overall net interface stress remains tensile). This interpretation is in good agreement with the observed magnitude. In particular, it suggests the elastic interpretation of the chemisorption at an organic-metal interface not to be too different from the one of an atomic chemisorption.

3.5.2. Shape analysis of $\Delta\tau$

The functional dependence of the surface stress change on coverage (depicted in figure 3.7) qualitatively follows the characteristics of a chemisorptive process: The surface stress decreases monotonously with a nearly linear slope in the low and medium coverage regime. The slope of the curve changes when a coverage of 75% is reached. In the highest coverage regime, the surface stress even seems to increase slightly before reaching its asymptotic value upon completion of the monolayer.

In order to disentangle substrate-adsorbate and adsorbate-adsorbate interactions, the coverage-dependence of the surface stress change has been analyzed by fitting the data to the Ibach model given in equation (3.22). The resulting fit can be seen as blue line in figure 3.7a. A small qualitative discrepancy between model and data points can be deduced from the systematic deviations in the residuum 3.7b. Nevertheless, the model still fits rather well given its simplicity and generality.

As parameter values, a $= (-0.383\pm0.002)$ N/(mML), b $= (1.73\pm0.07)\times10^4$ N/m and c $= (12.01 \pm 0.04)$ $\sqrt{ML}$ are obtained. The linear coefficient a can be fitted relatively well. But the other two parameters b and c are highly coupled and depend strongly on the details of the asymptotic flat tail. The uncertainty of the numeric absolute values of b and c is hence definitely larger than indicated by the error bars taken from the fit routine.
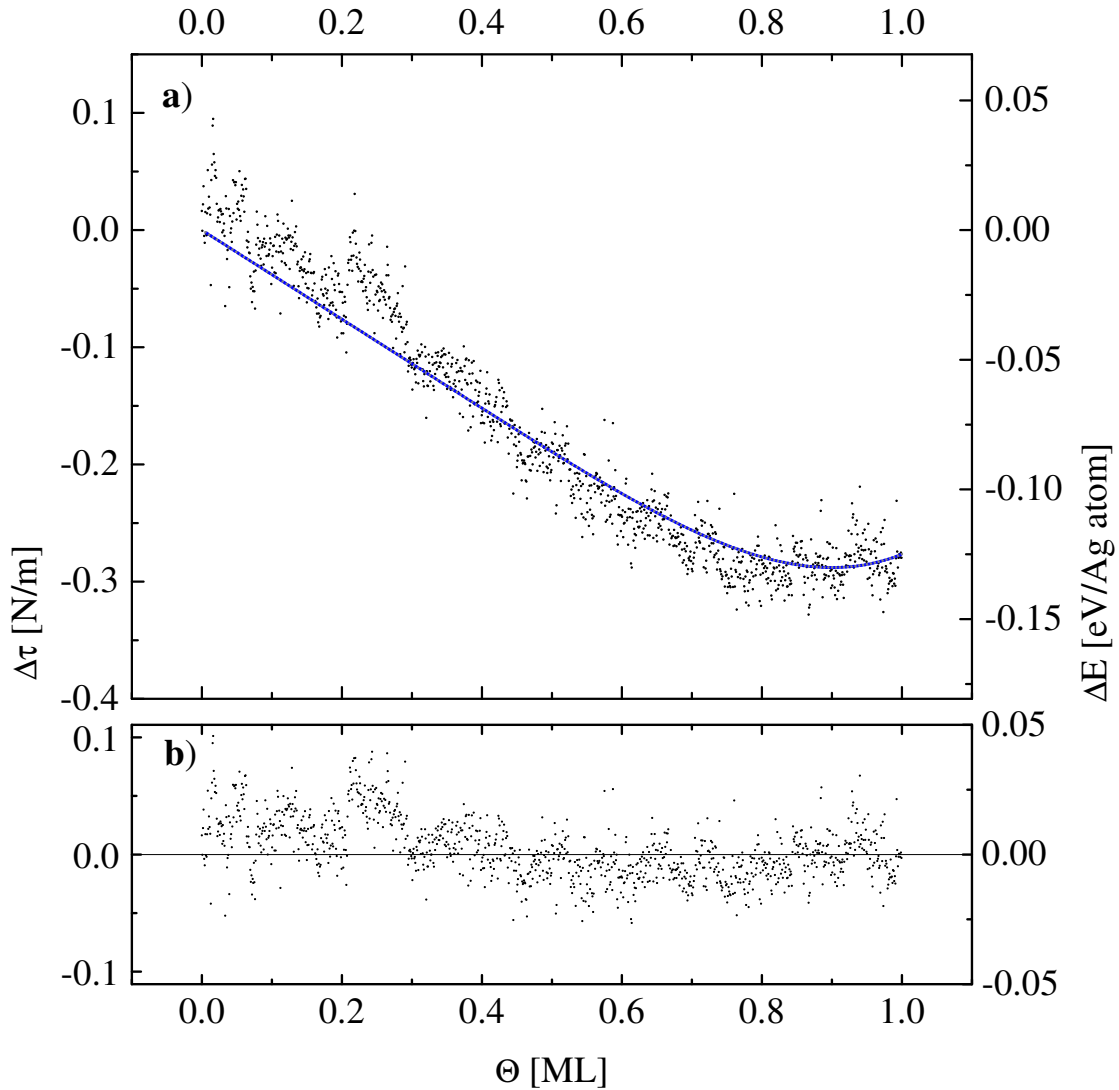
Figure 3.7.: **Coverage-dependence of surface stress change. a)** The surface stress change data (dots, see also fig. 3.6) has been fitted using the Ibach model (equation (3.22)). The fit result is represented by the blue curve. The obtained parameters indicate a compressive substrate-adsorbate interaction and a short-ranged tensile intermolecular interaction. **b)** Fit residuum.

According to the derivation in chapter 3.2.2, the coefficients reflect different contributions to the surface stress change in first approximation. The linear coefficient a is ascribed to the "direct" substrate-adsorbate interaction. As argued already before, the charge transfer from silver into PTCDA reduces the intrinsic tensile surface stress of the metal. Hence, the compressive character of the process is reflected by the negative sign of the coefficient.

With growing coverage, the correction term b ascribed to adsorbate-adsorbate interactions gets important. The overall positive sign signalizes that the molecules cannot be packed without limit. According to Ibach's reasoning [87], a tensile counter stress builds up with growing coverage.

But for the interpretation in the case of PTCDA/Ag(111), one must bear in mind that the formation of the adsorbate layer is not characterized by a continuous density increase in the surface layer as assumed for the gas adsorbate scenario by Ibach, but by an island growth mode. Adsorbed molecules are mobile enough to move quickly over large substrate areas. They attach to nuclei of the herringbone structure and thus reach more or less instantaneously their final closest packing. The intermolecular interaction within the perfect herringbone structure should hence contribute already in the low coverage regime and is therefore probably incorporated in the absolute value of a. Besides, as discussed before, the intermolecular interactions within the herringbone structure are expected to be of attractive and thus of compressive nature [156].

A more convincing interpretation takes into account the following observation: The onset of the deviation of the linear stress change curve occurs at relatively high coverage in the PTCDA/Ag(111) system. This is reflected by a large c coefficient compared to previously investigated systems (confirmed by table 3.5). The corresponding additional repulsive interaction can be explained by imperfect molecular orientations on the surface. In such a configuration, the inherent molecular quadrupole moment exerts a torque on neighboring molecules which induces surface stress. Furthermore, the orbital overlap of neighboring molecules might be suboptimal which would induce corrective forces, i.e. additional surface stress. Candidates are molecules at the borderline between domains of the superstructure. They do not contribute to the surface stress change in the low coverage regime because the density of domain boundaries is rather low in the PTCDA/Ag(111) system [136, 142]. Hence, they can be expected to play a significant role only when large domain islands meet.

Finally, it should be noted in addition that domain boundaries have been suspected to play a considerable role on PTCDA-silver substrate systems before. Schmitt [159] has proposed the formation of defect-free borderlines to be the reason for a re-faceting observed at the PTCDA/Ag(10 8 7)-interface. The respective process has been measured in this work to reduce the surface stress. This finding which will be discussed in much more detail in chapter 4 provides further evidence for the assumption that imperfect borderlines between superstructure domains can

Table 3.5.: **Compilation of fit parameter values for the Ibach model.** The listed parameters have been obtained by fitting equation (3.22) to the respective stress change curves.

Adsorbate system	a [N/(mML)]	b [N/m]	c [$\sqrt{ML}$]
S/Ni(100) [87]	35	5.5×10^2	3.3
O/Ni(100) [87]	6.5	2.0×10^4	6.0
C/Ni(100) [87]	12.0	7.5×10^3	0.77
PTCDA/Ag(111)	-0.38	1.7×10^4	12

induce tensile surface stress.

3.6. Conclusions

Several conclusions can be deduced from the experiment. They strengthen the trust in the applicability of the method to organic-metal interfaces and add new pieces of information to the broad and already comprehensive picture available of the PTCDA/Ag(111) system in particular.

From the perspective of the method, one can state that the surface stress change during the formation of the PTCDA/Ag(111) interface qualitatively behaves like a "conventional" system characterized by chemisorption. The release of the intrinsic tensile stress of the metal surface well explains the sign and the order of magnitude of the surface stress change. The remaining net surface stress of the interface can be deduced to be small but still of tensile nature from comparison with the absolute values of the intrinsic surface stress of Ag(111)(see chapter 3.2). The relatively weak binding of the PTCDA molecule to an individual silver atom is reflected by the small absolute change in binding energy compared to the (mostly) atomic adsorbate systems studied before.

More interesting are the results, however, when considering the system for which they have been obtained. Two major and surprising conclusions can be drawn from the at first glance "standard interpretation" given in the last paragraph. First, the fact that the cantilever bending method leads to meaningful results for an organic-metal interface at all cannot be expected a priori. It requires that additional local stress relaxation paths like, e.g., molecular distortions, do not seem to prevent the formation of long-range strain fields.

Moreover, the statement of a "small stress change" only holds when judged with respect to the small (inorganic) adsorbates investigated before. For the large molecular adsorbate which covers 33 substrate atoms a different normalization of the

surface stress is more revealing than the conventional with respect to the substrate area. It is highly remarkable that the change in surface stress per molecule is of the same order of magnitude as the suspected binding energy. Since the binding energy ultimately defines the relevant energy scale in the system, this result assigns surface stress a significant role for the interface formation.

As emphasized already in the discussion, the experiment gives some additional insight into the strength and occurrence of intermolecular interactions. Due to the almost instantaneous formation of a large superstructure, "regular" intermolecular interactions in the herringbone structure cannot be separated from the substrate-adsorbate induced stress change with the employed macroscopic technique. Further information could be gained in principle by investigating the surface stress change upon multilayer growth. The set up for this experiment would have to be even more stable than the one used in this work (see chapter 2.3). The Stranski-Krastanov growth mode, in which the system grows to multilayer coverage at slightly elevated temperatures (above 350 K), at least implies the molecular structure to be strained. An extended cantilever bending experiment could therefore provide further information.

However, even from the present experiment it can be deduced that the formation of imperfect boundary lines between domains induces a tensile stress. This result may be rather important: The built-in surface stress may give an explanation for the fact that the PTCDA/Ag(10 8 7) system is able to re-facet to promote perfectly fitting boundary lines [159].

A final remark should be made concerning the general implications of the experimental result. The fact that the surface stress changes slightly, yet significantly, implies that the positions of the silver atoms in the top layers change. Admittedly, the order of magnitude would be speculative to deduce from the data. To my knowledge, structural changes of the silver substrate upon interface formation have not been reported in literature, yet. The most sophisticated studies on the interface structure of PTCDA/Ag(111) by Krause et al. [139, 147] and Kilian et al. [141] focus more on the structure of the molecular film than on substrate changes. Since the present data indicate at least the existence of a structural change, a complete neglect thereof appears unjustified. The latter conclusion has consequences, e.g., for the interpretation of x-ray standing wave (XSW) data. It furthermore underlines that a correct ab-initio description of the interface must comprise fully relaxed substrate atoms in the top layers.

To sum up, the experimental result of the cantilever bending measurement of the adsorption of PTCDA on Ag(111) fits in general to the known properties of the system. Hence, confidence has been gained in the method and its application to a "new" system class of organic-metal interfaces. Furthermore, some details are surprising, especially the large value of the surface stress change. This "number" provides another piece of information of the interface which can and should be reproduced by model calculations. In this way, the elastic properties of the inter-

face could become another benchmark property besides geometric and electronic structure for a comprehensive model of the interface.

Surface stress and self-organization: PTCDA/Ag(10 8 7)

This chapter focuses on the process of large-scale self-organization. In the beginning, experimental observations of this effect are reviewed, followed by the particular interface of this study, PTCDA/Ag(10 8 7). The introductory part of the chapter is completed by a brief summary of the present theoretical understanding of the physics involved. In order to improve the comprehension of the process, the formation of the PTCDA/Ag(10 8 7)-interface is then studied with three complementary experimental methods in-situ: The cantilever bending technique, high resolution low energy electron diffraction, and low energy electron microscopy. This combination will finally allow conclusions on the physics driving the large-scale self-organization.

4.1. Phenomenology

In this section, surprising experimental results are presented from literature on the impact of the adsorption of large organic molecules on specific noble metal surfaces. Thereby, possible dramatic morphologic phase transitions will be encountered in these systems. Particular focus is on the known properties of the interface formed by PTCDA on vicinal Ag(111) are summarized because this system will serve as model system in the following.

4.1.1. From template growth to morphologic transitions

First, experiments are discussed in which the original structure of stepped vicinal surfaces is preserved under adsorption. They are given for completeness to represent the standard and expected behavior. In the second part of this section, a number of special systems will be presented of which the morphologies drastically change during interface formation.

"Conventional" growth of organic molecules on vicinal substrates

Step decoration defines distinguished adsorption states in many systems. Detailed observations have been made, e.g., for benzene/Cu(111) [160], thiophene/Ag(775) [161], fullerenes on Au(111) [162] or, as noted previously, for PTCDA/Ag(111) [17, 142, 159]. It appears hence straightforward to use well-defined vicinal surfaces of high step density to influence the growth behavior.

The goal of such adsorption studies is often to force otherwise non-nucleating adsorbates to nucleate by offering more high coordination sites. Primarily, however, the regular structure of high index surfaces is usually intended to be imposed on the formed interface, i.e. to use the stepped surface as a *template*.

The concept has already been demonstrated by Alvey et al. [163] for the adsorption of cyclopentene on Ag(221) in 1986. It has proven particularly valuable for the ordered growth of acenes on copper surfaces: Stable chain growth along step edges has been observed for naphtalene and anthracene on Cu(221) and Cu(443), despite their high mobility on the corresponding low-index Cu(111) surface [164]. Similarly, the next acene in the homologous series, pentacene, has successfully been grown in long-range ordered chains on Cu(119) [165].

Also 2-dimensional template-assisted patterning has been achieved. Néel et al. [166] have demonstrated C_{60} fullerene molecules to arrange in a rectangular pattern on Au(788) directed by the alternating fcc- and hcp-structure of this surface.

Finally, emphasizing the particularity of the effects discussed in the remainder of this chapter, it should be mentioned that also the large aromatic molecule PTCDA has been grown on vicinal noble metal surfaces without affecting their original structure. If adsorbed on Au(433), molecular chains form along the step edges [10]. Grown on Au(788) and Au(778), PTCDA monolayer structures do not reflect the substrates morphology at all [10]. At last, it is particularly interesting in this context that even if adsorbed on an "open" silver surface like Ag(110), only the structure of the molecular film is affected and not the morphology of the substrate. In this case, the molecules arrange in a brickwall pattern and not in a herringbone configuration. The substrate is left unaltered [142].

Step bunching, faceting, and long-range-ordering

There are metal substrates, however, whose morphology completely changes when large organic molecules are adsorbed. Low-index surfaces break up into high-index faces of different orientations. Surfaces with high original step density experience step bunching. After annealing facets with dimensions of several tens or even hundreds of nanometers are formed, which effectively lead to 3-dimensional mesoscopic hill-and-valley structures. Moreover, these new mesoscopic objects arrange by self-organization in almost perfect grating-like mesoscopic patterns with structural constants on nanometer scale.

These effects have been intensely studied for a number of organic acids on low-index noble metal surfaces. Already the most simple molecule in this class, the methanoic acid (or "formic acid"), has been observed by Leibsle et al. [167] to induce long-range faceting on oxygen-preconditioned Cu(110) surfaces. But also larger molecules containing the carboxylate functional group (-COOH) have shown their potential to reshape their hosting substrate. Examples for similar observations are benzoic acid on Cu(110) [167], or 4-[trans-2-(pyrid-4-yl-vinyl)]benzoic acid (PVBA) on Ag(110) [168]. Furthermore, faceting has been reported for various amino acids on Cu(110) [169] and on Cu(001) [170]. Some common properties can be deduced from these studies. Firstly, all acid molecules are oriented to allow local bonds between the carboxylate group and step edge atoms, independent of their size [168, 171]. Secondly, the same facet types are formed if the same original surface is used [167, 169]. Finally, a chirality of the adsorbents is conferred at the interface. As a fascinating consequence, it is hence possible to prepare chiral interfaces if homochiral adsorbents are used [172].

Faceting of low-index-surfaces is nevertheless not limited to adsorbents containing carboxylate-groups. Submonolayer coverages of copper-phthalocyanine (CuPc), e.g., have similarly been shown to induce step-bunching and faceting on Ag(110) [173].

Returning to the experiments discussed in the beginning of this chapter, I finally address interfaces between large organic molecules and high-index vicinal surfaces again. C_{60}-fullerene adsorption has been demonstrated to induce step-bunching, faceting, and order on mesoscopic scales when adsorbed on Cu(221) [174] and on Au(433) [12]. The importance of kinetics can be seen at the pentacene/Cu(119) interface: This interface has been previously discussed as a representative system preserving the original template morphology. If annealed above 463 K, however, it breaks up into a well-ordered hill-and-valley structure of facets of different polar orientations [175].

The driving forces of the gigantic morphology transition and the associated large mass transport (compare figure 4.1) are not really understood yet. The theoretical description will be discussed in chapter 4.2. At this point, however, first qualitative conclusions are summarized from the experimental observations: Clearly, the data
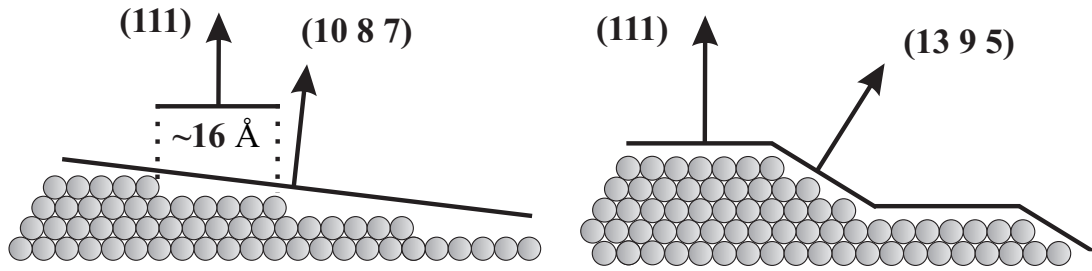
Figure 4.1.: **Mass transport during faceting.** The schematic illustrates the gigantic mass transport on the atomic level in the substrate during the faceting transition from a (10 8 7) surface into (111) and (13 9 5) faces.

indicates that strong local interactions between adsorbate and prominently exposed step atoms stabilize the newly built facets [171]. But the underlying physics is definitely more complex. For once, "more collective structural effects" contribute. One example is the observation that adsorbate-induced reconstructions on terraces adjacent to step bunches seem to support specific facets [170]. In particular, the long-range order must be supported by another mechanism which should be able to act on a much larger length scale than the local chemical interactions discussed so far.

4.1.2. PTCDA/Ag(10 8 7)

The representative interface chosen to study the underlying mechanism of the self-organization is formed by PTCDA on vicinal Ag(111). Its morphology and preparation dependence has been thoroughly investigated [17, 159], using a combination of microscopic (STM) and diffraction (LEED) methods. Therefore, it is an ideal system to study the formation processes behind the final ordered state.

The system differs from the well-known PTCDA/Ag(111) interface (reviewed in chapter 3.3) by the orientation of the substrate. A polar miscut angle of 8.5° has been chosen in all the experiments discussed in this work. If properly prepared (see chapter 2.1), the clean silver surface consists of (111) terraces separated by single atomic steps (as shown in figure 4.1). The configuration is stabilized by the mutual step repulsion. The average terrace width of 16 Å is in the order of the dimensions of the PTCDA molecule (9.2 Å × 14.2 Å). Seidel [17] and Schmitt [159] have studied crystals of different azimuthal orientations ((775) and (10 8 7)) characterized by two different step types: Kink-free straight steps in the case of the (775) surface, and steps with intermediate kink-density in the case of the (10 8 7) surface. The general behavior is similar for both substrates. Nevertheless, the details (like the specific counter facets) depend on the original orientation of the substrate.

The adsorption of small amounts (from percentages up to a complete monolayer)
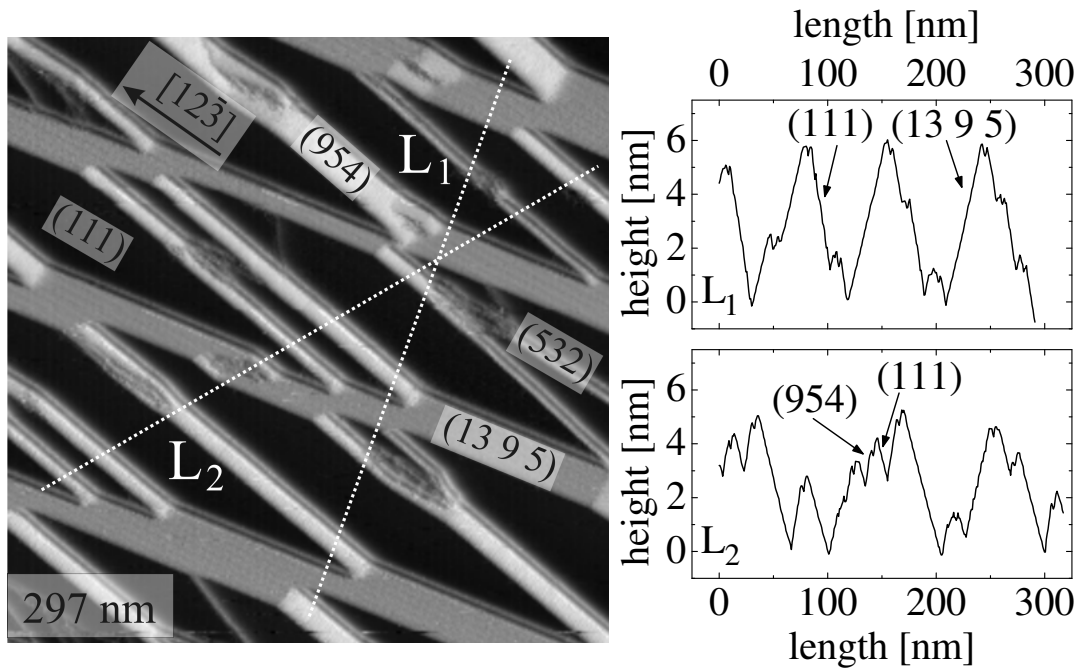
Figure 4.2.: **Morphology of the faceted surface as seen by STM.** The PTCDA/Ag(10 8 7) interface depicted here has been prepared by adsorbing 0.4 ML of PTCDA on a Ag(10 8 7) sample kept at 550 K. Four different facet types can be identified in the depicted region and are labeled. The pristine step direction [12$\bar{3}$] is indicated. The line scans L$_1$ and L$_2$ are chosen perpendicular to the (13 9 5) and (954) facets on a topographic image along the dotted lines in the depicted differentiated image. (Tunneling parameters: I=2.0 nA, U=1.34 V. Raw data provided by Stefan Schmitt.)

of PTCDA on these vicinal Ag(111) surfaces can now have a dramatic effect. At room temperature, no ordered phase is observed [17]. If done at approximately 400 K substrate temperature [17], however, the molecules begin to modify the surface. Ordered molecular chains nucleate on two or three silver steps, forming stable step bunches [17, 159]. At a substrate temperature of 550 - 600 K the silver atoms are mobile enough that these step bunches can grow into facet faces of nanometer size [17]. The vicinal surface decomposes into larger (111) terraces and facets of high step density. According to the available LEED and STM data, the latter ones are populated by stable PTCDA islands only after all steps are decorated, which corresponds to a nominal coverage Θ of 0.4 ML. Schmitt [159] has reported on 17 different facets. Their formation depends on the nominal substrate orientation, on PTCDA coverage, and especially, on the preparation path (e.g. substrate temperature, or sequence of annealing and adsorption) [159].

The facets formed are microscopically stabilized by the PTCDA molecules. Their binding energy has to compensate the step repulsion. Various commensurate, point-on-line and even incommensurate superstructures have been observed [159]. At higher coverage, facets seem to be preferred for which the superstructures interlock perfectly at the borderline [159].

As indicated before, the reconstruction does not only affect the microscopic, but also the mesoscopic scale. The newly formed facets arrange almost equidistantly in a "staircase"-like manner [135], leading to a uniform grating like pattern. The structural widths depend strongly on coverage [159]. An example for such a preparation is depicted in figure 4.2. The STM image and the line scans of the topography identify a corrugated surface with facets of several types, which are separated with almost perfect equidistant spacing.

The system has already been successfully exploited as a template for the deposition of iron clusters [11]. Besides, it has been used to study the face-specific coadsorption of PTCDA and 2,5-dimethyl-N,N'-dicyanoquinondiimine (DMe-DCNQI) [13]. Nevertheless, in order to realize a technological application as template on the nanometer scale, the underlying basic physics has to be understood.

4.2. Theoretical description of periodically faceted surfaces

Most of the morphologic transitions presented in the last chapter can be divided into two different thermodynamic processes in first approximation. First, there is the break-up of the morphology, and the formation of new facets or crystal faces after adsorption. Second, these new morphologic objects often order by self-organization on mesoscopic scales. In addition, much material must be transported leading to questions about the kinetics of these processes.

4.2.1. Faceting under thermodynamic considerations

The experiments presented in this work will contribute mainly to the understanding of the formation of long-range order. Nevertheless, a very brief summary of the theoretical understanding of the actual faceting transition is given in this section for completeness. Details can be found, e.g., in the excellent review by Rottman and Wortis [84], or in the textbook by Mutaftschiev [176].

To first order approximation, the shape of the surface of a given crystal is governed by the anisotropy of the surface free energy $\gamma(\vec{n})$ (compare chapter 3.1.2). To be more precise, the crystal shape in thermal equilibrium (ECS) minimizes the surface integral over the specific free energy. Besides, the boundary condition that the overall volume of the crystal is defined by the number of atoms involved and is therefore constant must be fulfilled. Mathematically, this can be formulated as

$$\oint_{crystal} \gamma(\vec{n})dA \xrightarrow{dV \equiv 0} min, \tag{4.1}$$

which is known as *Wulff's theorem* [176, 177]. The equilibrium shape can be graphically constructed in the so-called *Herring's γ plot* [176] using the *Wulff construction* [84, 176, 178].

Equation (4.1) defines an equilibrium shape with few distinguished faces. It is strictly valid only at 0 K. At more elevated temperatures, configuration enthalpy cannot be neglected. In effect, its contribution smoothes the free energy landscape. At the *roughening temperature T_R* the equilibrium shape is finally completely round, indicating that all faces can occur on the surface [176].

If a given crystal surface is not part of the ECS of the crystal, it is unstable against decomposition into a hill and valley structure (*Herring's theorem*) [178]. In other words, the system tends to facet in this case.

To cover the experiments given in chapter 4.1, one further point has to be comprised in the description: The theory presented up to now is obviously originally designed to derive the crystal shape of homogeneous pure materials. The focus of this work, however, is on faceting under adsorption of different atomic or molecular species. Nevertheless, the previous concepts are easily extended to heterogeneous interfaces [176]. Adsorption of foreign atoms or molecules modifies the free energy of the interface in question [171]. The Shuttleworth equation (3.20) relates, e.g., a changing surface stress under chemisorption to a changing surface free energy. The respective changes in free energy are in general not isotropic, i.e. the landscape of the free energy can be altered. As a consequence, the derived equilibrium crystal shape will change. In this case, the interface will break up and facet if kinetically possible.
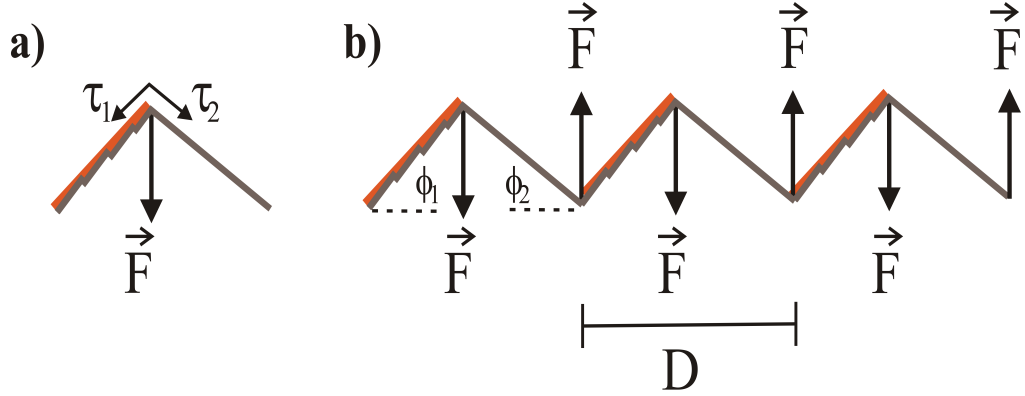
Figure 4.3.: **Surface stress and point forces. a)** The discontinuity of the surface stress τ induces a point force $\vec{F}$ at the boundary. **b)** The periodic sawtooth-like profile of a 1-D faceted surface leads to effective force dipols acting at the boundaries.

4.2.2. Long-range order: The Marchenko-Alerhand model

From an intuitive point of view, the formation of a boundary between two different phases requires energy: Since atoms are in suboptimal configuration at the boundary, their binding energy can be assumed to be lower than within an island. Therefore, a complete phase separation or at least huge domains could be expected to be the ground state of a system (interface) which consists of different phases. Stated otherwise, a spontaneous pattern formation as observed in the systems in chapter 4.1 could not be understood without another energetic contribution which, on top, should also be based on or result in a long-range interaction.

The Marchenko-Alerhand model

Marchenko [14], Alerhand et al. [15], and Vanderbilt [16] have investigated the mutual interactions of the boundaries. Their inclusion into the surface free energy leads to a ground state characterized by ordered domains.

The so-called "standard model" [75] for spontaneous pattern formation is based on the following ansatz for the surface free energy: If one assumes a one-dimensional regular pattern of two different domains "1" and "2", one with coverage Θ and the other one with coverage $(1 - \Theta)$, the surface free energy per unit area γ can be written as

$$\gamma = \Theta\gamma_{0,1} + (1 - \Theta)\gamma_{0,2} + \frac{\beta}{D} + \gamma_{interaction}. \qquad (4.2)$$

The first two terms represent the surface free energy of the two phases $\gamma_{0,i}$ and are independent of the periodicity D (defined in figure 4.3), while the parameter β represents the necessary energy to form a boundary.

The relaxation due to boundaries is contained in the fourth term. In principle, three different contributions to the interaction can be thought of: An entropic, an electrostatic, and an elastic contribution [75].

At non-zero temperature, step fluctuations reduce the free energy as the entropy S enters into the energy balance by $-TS$. Since neighboring steps are not allowed to cross, the configuration entropy S gets the smaller the closer two steps get. Analytically, the reduction has been found to increase with $1/D^2$ [75, 179, 180]. If the mobility of steps is hindered by interaction with adsorbents, the entropic repulsion between steps can be expected to be decreased significantly [173]. Therefore, the entropic contribution can usually be neglected.

The second contribution might be more significant. Surface phases of different orientation or coverage differ in work function by $\Delta\Phi$ [181]. If these phases alternate, their interaction in the far field can be described by effective surface dipoles. The interaction energy term is given by

$$\gamma^{electrostatic}_{interaction} = -\frac{\varepsilon_0}{2\pi}\frac{\Delta\Phi^2}{D}ln\left[\frac{D}{\pi a}\sin\left(\pi\Theta\right)\right], \tag{4.3}$$

with D being the periodicity, a an artificial cutoff parameter on atomic scales, and ε_0 the dielectric constant[16]. It is in form and functional dependence equivalent to the (1-dimensional) stress interaction energy term (compare equation (4.4)).

Estimates of the O/Cu(110) stripe phase [16] and measurements in the case of the N/Cu(001) checkerboard pattern [182], however, indicate the elastic interaction to dominate. Hence, the elastic contribution is usually considered to be the relevant term in the standard description. The interaction energy can qualitatively be constructed from point forces: At the intersection of two phases of different surface stress the respective tensor gets discontinuous. In effect, a force is induced acting on the boundary line [183]. The orientation of this force depends on the sequence of the phases. Thus, neighboring point forces have opposite signs for a repetitive stripe pattern. The resulting strain field of such a pattern can again be described by effective point force dipoles. This qualitative "construction" of the force field is depicted in figure 4.3.

Integrated, the free energy contribution of the elastic interaction in the case of a one dimensional sawtooth-faceted surface adds up to [75]

$$\gamma^{elastic}_{interaction} = -\frac{2\left(1-\nu^2\right)}{\pi Y} \times \frac{|\Delta\tilde{\tau}|^2}{D}\ln\left[\frac{D}{\pi a}sin\left(\pi\Theta\right)\right] \tag{4.4}$$

with ν being Poisson's ration, Y Young's modulus, a a cutoff parameter on atomic scales, and the effective stress difference $|\Delta\tilde{\tau}|^2$ between phases "1" and "2" given as

$$|\Delta\tilde{\tau}|^2 = (\tau_1 - \tau_2)^2 + 4\tau_1\tau_2\sin^2\left(\frac{\phi_1 + \phi_2}{2}\right). \tag{4.5}$$

The second term in expression (4.5) is necessary to project the inclined length of the facets onto the base line in order to reduce the problem to one dimension. The respective inclination angles are represented by ϕ_1 and ϕ_2 (compare figure 4.3). Further geometries are compiled, e.g., in reference [75].

In summary, the free energy of the system (4.2) shows a distinct dependence on the structure parameter D. The minimum free energy is obtained for an optimum period D_{opt} of

$$D_{opt} = a \times \frac{\pi}{\sin\left(\pi\Theta_D\right)} exp\left[\frac{\beta Y \pi}{2|\Delta\tilde{\tau}|^2\left(1-\nu^2\right)}\right] \tag{4.6}$$

if only elastic interactions (4.4) are considered [75]. Due to the exponential dependence, D_{opt} can be orders of magnitude larger than the atomic scale a.

Experimental verification

Although the standard model is frequently used as explanation, experimental verifications are rather scarce.

A first, indirect way to verify the formalism has been developed by Zeppenfeld et al. [184, 185]. They have derived a "universal" relation between the width of the minority phase at low coverage and the minimal structure constant of a self-organized pattern. The respective ratio of approximately $\frac{1}{3}$ [184] has been observed, e.g., for the 2-dimensional pattern of silver islands on Pt(111), the checkerboard pattern of terraces on Pd(110), and for the Cu-O(2x1)/Cu(110) stripe phase [184].

A direct measurement of the elastic interactions involved has only been accomplished for two systems: for the N/Cu(001) checkerboard pattern [182, 186], and the Cu-O(2x1)/Cu(110) stripe phase [61, 187]. Croset, Prévot, and coworkers [182, 186, 187] have used a combination of grazing incidence x-ray diffraction (GIXD) and displacement field calculations to prove a surface stress difference of 7 N/m in the former and (1.0 ± 0.1) N/m in the latter case to be the driving force of the respective long-range order. For the CuO-Cu-stripe phase, the conclusion is also supported by the results of Bombis et al. [61] who determined the surface stress change by evaluating the curvatures of STM images.

4.2.3. Kinetics of nucleation

Up to now, the system has been discussed from the thermodynamic point of view, assuming the system to be in equilibrium. But an exclusively thermodynamic approach cannot cover the complete physics of this system class. Considering the large mass transport involved, kinetics should play a role, too. Indeed, Schmitt has observed, e.g., a dependence of the morphology of the PTCDA/Ag(10 8 7) interface on growth parameters in his work [159].

From the previous discussion, it is clear that periodically faceted systems are very complex. To my knowledge, theoretical studies of the explicit kinetics of such

transitions have not been performed yet. Nevertheless, anisotropic nucleation has been studied for simpler systems. Respective models are either based on Monte Carlo simulations or on classical mean-field theories. The latter formalism has been reviewed by Venables and coworkers [188].

In the frame of this work, the focus is on one particular aspect, which is the distribution of stable islands formed during adsorption. The respective field in physics uses a relatively fixed nomenclature for the basic quantities. The symbols used are compiled in table 4.1; explicit definitions within the text will be omitted for the sake of readability.

The growth of islands can be described in mean-field theory by effective rate equations [188]. These equation systems can be solved in different growth regimes. In steady-state, if the number of nucleating atoms can be regarded as equal to the number of freshly adsorbed ones, fractional power laws of the form

$$N_x(\Theta) \sim \left(\frac{R}{\nu_V} \right)^\chi exp \left(\chi \frac{E_d + E_i/i}{k_B T} \right) \tag{4.7}$$

describe the density of stable islands N_x [188, 189]. The exponent χ comprises the critical cluster size i. The analytic form of χ depends on the dimension of the island growth [188]. For 2-dimensional film growth under isotropic conditions, e.g., χ is given by [188]

$$\chi = \frac{i}{i + 2.5}. \tag{4.8}$$

Therefore, relation (4.7) can be used to gain information on the critical nucleus size and activation energies from temperature and/or rate-dependent experiments (e.g. [44, 190]).

Evans and Bartelt [189] have driven the analysis further and investigated the distribution of the sizes of stable islands. They have shown that the respective density N_s obeys the following scaling law in the low coverage regime [189]:

$$N_s \sim \frac{\Theta_x}{s_{av}^2} \cdot f_i(s/s_{av}). \tag{4.9}$$

The *island size distribution function* f_i contains the physics of the specific nucleation process. As a mathematical distribution function, it is required to be normalized by $\int f(y)dy = \int yf(y)dy = 1$ [189]. Monte Carlo simulations have shown a strong dependence on the critical nucleus size i [189], a modest dependence on temperature T [191], and on the extent of island sizes for anisotropic diffusion [192].

For a critical island size i of 1, Blackman and Mulheran have developed an analytic expression for f_1 in one dimension [193]. Furthermore, they have succeeded to expand the result to quasi-1D nucleation (again with i=1) on stepped substrates [194]. A general expression for f_i, however, is not known in an explicit form.

Table 4.1.: **Kinetic nomenclature.**

symbol	physical meaning
ν_v	vibrational pre-factor or attempt frequency
R	adsorption rate
E_d	activation energy for diffusion
i	critical atom number for an island to be stable
E_i	binding energy associated with a critical island
s	number of atoms in a stable island (s≥i)
s_{av}	average number of atoms per stable island
S	scaled island size S:=s/s_{av}
N_s	density of stable islands of size s per adsorption site
N_x	density of stable islands per adsorption site: $N_x = \sum_s N_s$
Θ	total coverage
Θ_x	coverage associated with stable islands

The existence of a scaling law has an impressive consequence for island size distributions N_s. If distributions gathered under moderately different experimental conditions are scaled with s_{av}^2/Θ_x and plotted over $S = s/s_{av}$, they collapse in a single curve, namely the mutual island size distribution f_i. This behavior has indeed been observed not only in Monte Carlo simulations, but also in real experimental data. Respective studies have, e.g, successfully been performed on STM data gathered during the homoepitaxial growth of metals, like Fe/Fe(001) [191] or Pt/Pt(100) [190, 192].

4.3. Motivation

The literature review of the previous sections shows that on one hand, a sophisticated model for the spontaneous formation of long-range ordered mesoscopic systems has been developed for over twenty years. But on the other hand, experimental confirmation is rather scarce and, in particular, limited to systems in which only the adsorbate forms the pattern. The systems presented in chapter 4.1, however, are all characterized by spontaneous long-range ordering of both, substrate and adsorbate. The influence of surface stress in such a system has not yet been experimentally investigated at all. Moreover, the significance of surface stress at metal-organic interfaces is unclear, as argued in chapter 3.

Thus, the driving force of the long-range order in the systems compiled in chapter 4.1 is speculative in the sense that experimental data is missing. Considering their prospective technological importance, an experimental insight into the mechanism
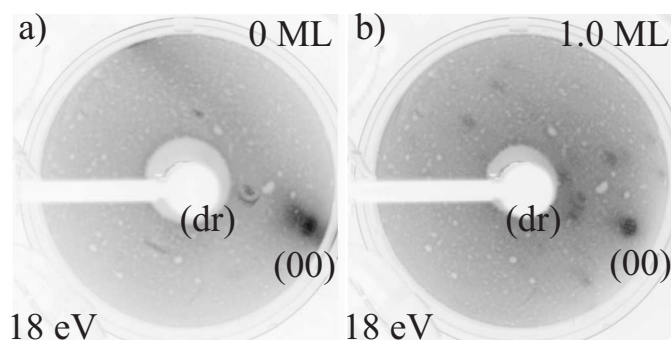
Figure 4.4.: **LEED characterization of the "disordered" PTCDA/Ag(10 8 7) interface.** The (00) spots of the (111) faces and the direct reflections of the incoming beams are marked. **a)** The prepared clean cantilever crystal at 18eV. In this out-of-phase condition, the (00)-spot is clearly splitted. **b)** PTCDA/Ag(10 8 7) interface in its "disordered" state at 18 eV. The (00) splitting is lifted. From energy dependency measurements (not shown here) all spots can be identified to belong to the superstructure of the (111) terraces.

behind the process appears highly desirable.

4.4. Surface stress change upon PTCDA adsorption

Cantilever bending experiments were performed to measure the change of surface stress during the adsorption of PTCDA on a (10 8 7)-oriented silver cantilever crystal. Its properties are given in table 2.1.

Depending on substrate temperature, two different final states can be obtained when adsorbing one monolayer of PTCDA: A faceted, long-range ordered interface at elevated substrate temperatures, and a less ordered one at lower temperatures. Both interfaces have been studied and will be discussed in the following two sections.

4.4.1. Surface stress change in the low temperature regime

In the first cantilever bending experiment the (10 8 7)-oriented cantilever is kept at (338.0 ± 0.1) K. One monolayer of PTCDA is deposited on top of the crystal with a deposition rate of (0.070 ± 0.005) ML/min for which the evaporator is kept at 625 K. The coverage of a closed monolayer was confirmed by XPS. The structural characterization shows the specific state the system is in if these preparation conditions are applied: In the LEED data comprised in figure 4.4, no specular facet spots can be identified. The splitting of the (00) spot, however, has vanished.

The stress change deduced from a corresponding cantilever measurement is depicted in figure 4.5a. At first glance, the data appears rather unspectacular: In the
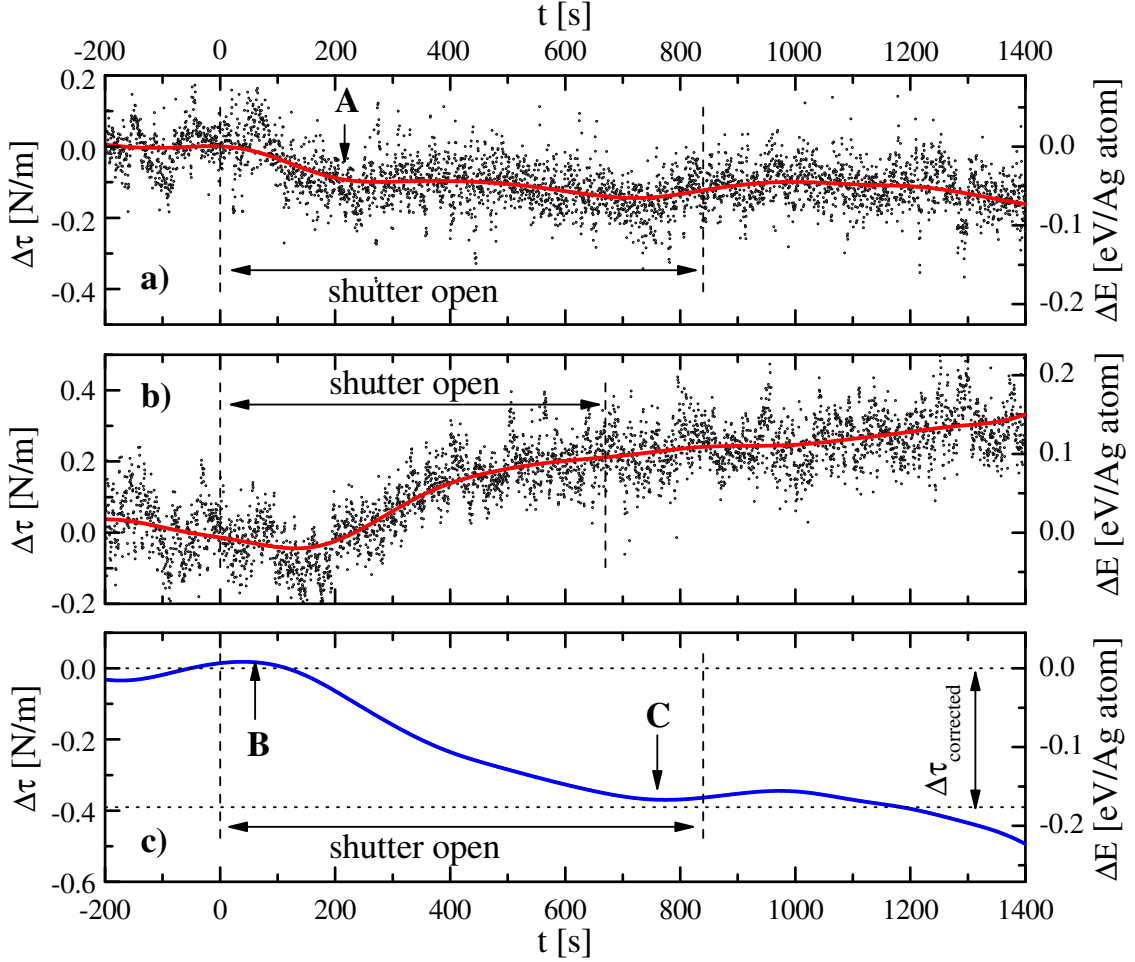
Figure 4.5.: **Surface stress change upon formation of the PTCDA/Ag(10 8 7)-interface at** $\mathbf{T}_{sub}$**=338 K. a)** The measured surface stress change during adsorption of one monolayer of PTCDA (in between dashed lines). The dots indicate the raw data, the red line has been obtained by smoothing by Gaussian convolution. **b)** Stress change mimicked by heat induced bending. The clean substrate is exposed to heat radiation by the evaporator kept 100 K below the PTCDA evaporation onset temperature. **c)** "Corrected" surface stress change. The red smoothed stress changes of a) and b) have been subtracted to account for heat induced changes. The corrected overall stress change amounts to $\Delta\tau$=(0.39 ± 0.10) N/m.

initial coverage regime, $\Delta\tau$ drops by (-0.09 ± 0.03) N/m. The value is reached at a coverage of 0.25 ML (point A). Subsequently, $\Delta\tau$ appears to be constant.

The measurement result, however, is a convolution of the bending induced by PTCDA adsorption and the bending induced by heat radiation of the evaporator. The latter effect is really significant under the employed experimental conditions, i.e. for low substrate temperature and imperfect heat shielding, especially since the evaporator was in a pre-stage design for the respective experiments, without the second pinhole heat shield. In order to quantify the heat influence, the clean substrate was exposed to the heat of the evaporator kept at 520 K, well below the evaporation temperature of PTCDA. This deviation from the standard procedure for the validation experiment was necessary in this case because the interface is not inert against further PTCDA exposure. In figure 4.5b the measured "mimicked" stress change is depicted: A positive (!) change in surface stress of $(+0.25 \pm 0.05)$ N/m is observed with a characteristic step-like functional dependance.

The actual "heat-induced" stress change is probably even larger in figure 4.5a since the evaporator is used at a temperature of 625 K. Nevertheless, measurement 4.5b gives the correct sign and a lower limit in the right order of magnitude of the effect. It therefore appears legitimate to subtract data set 4.5b from data set 4.5a to separate the real stress change from the heat-induced signal. Thereby, at least the overall magnitude and the general tendency of the surface stress change can be deduced. The thus corrected data set is depicted as blue line in figure 4.5c.

Initially, $\Delta\tau$ remains constant within the limits of accuracy of the subtraction. At a coverage of 0.08 ML (point B), $\Delta\tau$ starts to drop and changes rather monotonously until an almost complete coverage of 0.9 ML PTCDA is reached in point C, after which the curvature of the stress change flattens. After shutter closure, $\Delta\tau$ does not significantly change, considering the growing error due to imperfect drift corrections in the original measurements. In total, a (lower) limit of the adsorption-induced stress change of $\Delta\tau_{corrected}$ to (-0.39 ± 0.1) N/m can be derived after the correction for external influences.

In summary, the corrected surface stress change strongly resembles in shape and magnitude the stress change observed for the adsorption of PTCDA on (non-vicinal) Ag(111) discussed in chapter 3.4. This finding fits to the interpretation of the LEED data: The steps are bunched on the surface because the spot splitting is suppressed after adsorption. But the thermal energy does not seem sufficient to promote the material transport necessary to form large facets on the timescale of the experiment. Therefore, no specular facet spots can be identified. Hence, the surface is dominated by larger (111) terraces and step bunches, which are not arranged in a specific long-range order. A long-range strain field leading to self-organization has not built up yet.

4.4.2. Surface stress change upon faceting and self-organization

The experimental conditions are now altered and the sample is kept at (550.0 ± 0.1) K throughout the experiment. According to the LEEM experiments (see chapter 4.6), thermal energy suffices under these conditions to promote the instant faceting and formation of long-range order. The sample has been characterized before and after each adsorption experiment with XPS to check the deposited amount of PTCDA (1.0 ML), and with LEED to proof a successful structural transition.

Figure 4.6a shows the PTCDA-induced surface stress change under these experimental conditions. The data indicates that the adsorption of PTCDA on Ag(10 8 7) causes a significant compressive surface stress change of (-0.67 ± 0.10) N/m. Depending on coverage, however, also regimes of constant or even tensile $\Delta\tau$ intersect the overall compressive tendency. Moreover, the surface stress still alters after shutter closure, i.e. without exposure to PTCDA. Hence, the experiment can be divided into two physically inequivalent phases: Adsorption and annealing.

During adsorption the surface stress change shows a puzzling evolution: At low coverage (A-B), $\Delta\tau$ remains constant on the resolvable scale. At point B, the surface stress drops by (-0.29 ± 0.02) N/m. But the slope of the curve changes its sign at point C and $\Delta\tau$ increases by $(+0.07 \pm 0.02)$ N/m. At point D, the gradient of the surface stress change decreases again and changes only slightly until a coverage of 56% (point E) is reached. The completion of the monolayer (E-F) induces a negative change in surface stress.

Closing the shutter, however, does not define the end of the surface stress change. The slope of the stress change gets even steeper in the initial annealing phase. It takes approximately 1350 s without exposure to molecules (point G), in which the system is still kept at 550 K, until the surface stress change finally approaches its asymptotic value of (-0.67 ± 0.10) N/m.

Looking closely, one can also identify additional wiggles in the smoothed data in this regime. Nevertheless, they can also be observed before the shutter opening and during the reference measurement shown in figure 4.6b. Therefore, the respective modulation is assigned to external unidentified sources of noise.

The depicted measurement is representative for successful experiments. The relatively high noise level in the raw data indicates that the stress change is at the limit of the resolution of the set up. Nevertheless, it proves to be very stable against heat effects when looking at the validation experiment depicted in figure 4.6b: During exposure to the molecular beam and the heat flux of the evaporator (i.e. in the marked region between points A' and F') the signal mimics a stress increase by approximately 0.05 N/m. This value is in the order of the noise level. External influences can therefore be neglected for the interpretation of the data.
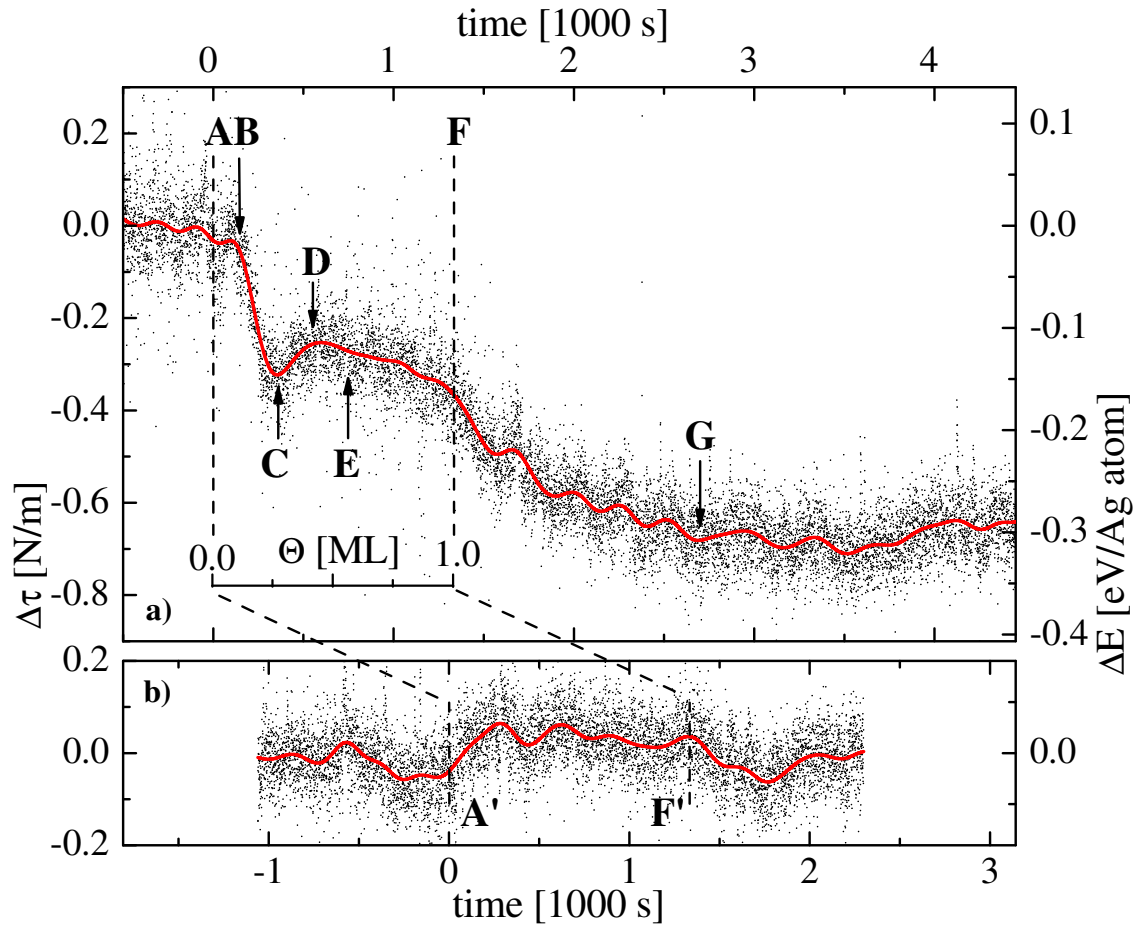
Figure 4.6.: **Surface stress change upon formation of the PTCDA/Ag(10 8 7)-interface at T_{sub}=550 K. a)** The thick red line renders data smoothed by a Gaussian convolution while the raw data is presented by small dots. The cantilever has been exposed to PTCDA in between the dashed lines (labeled A and F); the additional scale converts the exposure time into the respective coverage. Characteristic points at which the stress regime alters are marked with capital letters B-E and G. **b)** Additional exposure under the same conditions between points A' and F' leaves the surface stress unaltered demonstrating the stability of the setup.

4.5. SPA-LEED characterization of the system

The complex coverage dependence of the surface stress change can only be understood with the help of complementary insight into the system. Prime candidates to explain deviations from a monotonous surface stress change are structural transitions of the system (compare chapter 3.2.2).

Suitable time-resolved structural data on the system to support this hypothesis can be obtained using high resolution spot profile analysis low energy electron diffraction (SPA-LEED). The measurements have been performed in a different chamber which is capable of in-situ SPA-LEED measurements (see chapter 2.2.1).

Due to limited degrees of freedom in the manipulator positioning, the cantilever crystal itself - tilted macroscopically because of heat expansion under asymmetric clamping - cannot be aligned perpendicularly to the SPA-LEED axis. Therefore, a vicinal "bulk" crystal has been used as substrate for the following measurements. It is oriented in (10 8 7) direction, identical to the cantilever crystal. This crystal has been used before for the characterization of the system with STM [159].

The same preparation parameters (adsorption rate, temperature) have been chosen as in the cantilever experiments. The morphology of the faceted cantilever sample has been measured with conventional LEED. The observed patterns fit to the ones measured for the bulk sample in SPA-LEED. The lower resolution of the conventional LEED patterns, however, limits the accuracy of such a comparison. Nevertheless, the comparison confirms the same microscopic adsorption behavior of the two samples, given the same starting orientation, identical experimental procedures, and agreeing LEED patterns.

In the following section, different intermediate states of the system at critical coverages are characterized by SPA-LEED. These measurements identify the few features really necessary to map the structural dynamics in the system. In the thus strongly compressed relevant k-space, time-resolved measurements are possible, which are discussed in the second part of this section.

4.5.1. Identification of facets

Besides the techniques employed before to characterize the faceted system (STM, conventional LEED, and principle crystallographic considerations [159]), SPA-LEED offers a high k-space resolution. This independent measurement can therefore be seen as verification of the morphologic description by Schmitt [159]. Indeed, the results can be interpreted with his morphologic model. But the main goal of the following characterization is the identification of the minimum number of features necessary to map all relevant morphologic transitions in the system.

3D reciprocal space maps

The interface has been prepared for different partial coverages of PTCDA. During the whole experiment the system has been kept at (550 ± 1) K. Furthermore, the interface has been annealed at this temperature for another 30 minutes after completion of the final coverage. Besides the latter step, the same preparation path as in the cantilever experiments and in the in-situ SPA-LEED measurements (see chapter 4.5.2) has been used.

The system has been analyzed in three regimes in which major structural changes can be expected from previous measurements. To grasp all relevant major features, the morphology has been investigated with energy series of 2-dimensional SPA-LEED diffractograms. Following the procedure described in chapter 2.2.3 3-dimensional reciprocal maps of the central diffraction rods (for which distortion effects are smallest) have been extracted from the data.

The first series presented here has been taken at a nominal coverage of PTCDA of (0.24 ± 0.03) ML. In this regime, the first re-faceting from facets inclined by $27°$ to $20°$ is expected [159]. The result of the measurement is summarized in figure 4.7. Due to the low coverage, the overall intensity of the raw data is relatively small and the contrast thus not optimal. More intense and sharper spots can be assigned to traces of facet rods stemming from two different facet faces. Remaining weak intensity can be explained as traces of two other facet types, which will be fully grown at intermediate coverage (see below).

In azimuthal projection (indicated in figure 4.7) the traces form bunches, which intersect in the $k_{12\bar{3}} = 0$ Å^{-1} line and are periodic in the $(\bar{5}41)$ direction. The four facet traces are in azimuthal orientation identical to the ones found at intermediate coverage. As can be seen in table 4.2, the fits through the more intense facets (shown in the 3D plot in figure 4.7b) give polar angles of $15.9°$ and $13.9°$. The relatively large error bar of $2°$ is due to two reasons: Firstly, the spots from which the positions have been read-out are not very sharp. Secondly, the overall alignment of the crystal is most difficult in the low-coverage regime since the specular spot still splits significantly at energies which are not completely in-phase. Therefore, the two identified types of diffraction rods can also be considered to be identical to the ones observed in the higher coverage regimes with regard to their polar coordinates.

At a PTCDA coverage of (0.66 ± 0.04) ML, all spots observed are sharp and intense (compare figure 4.8). Spot splitting is not observed any more. Thus, there are not enough free single steps left on the surface within the transfer width of the SPA-LEED to influence the diffraction pattern. Stated otherwise, most of them are already bunched to form the large facet terraces in this coverage regime.

The model of four different sets of diffraction rods discussed already in the low coverage regime perfectly explains all traces in the overlaid data image in figure 4.8. Furthermore, the spots also lie on perfect lines in the reconstructed 3-dimensional reciprocal space. The fitted orientations of the diffraction rods show a narrow
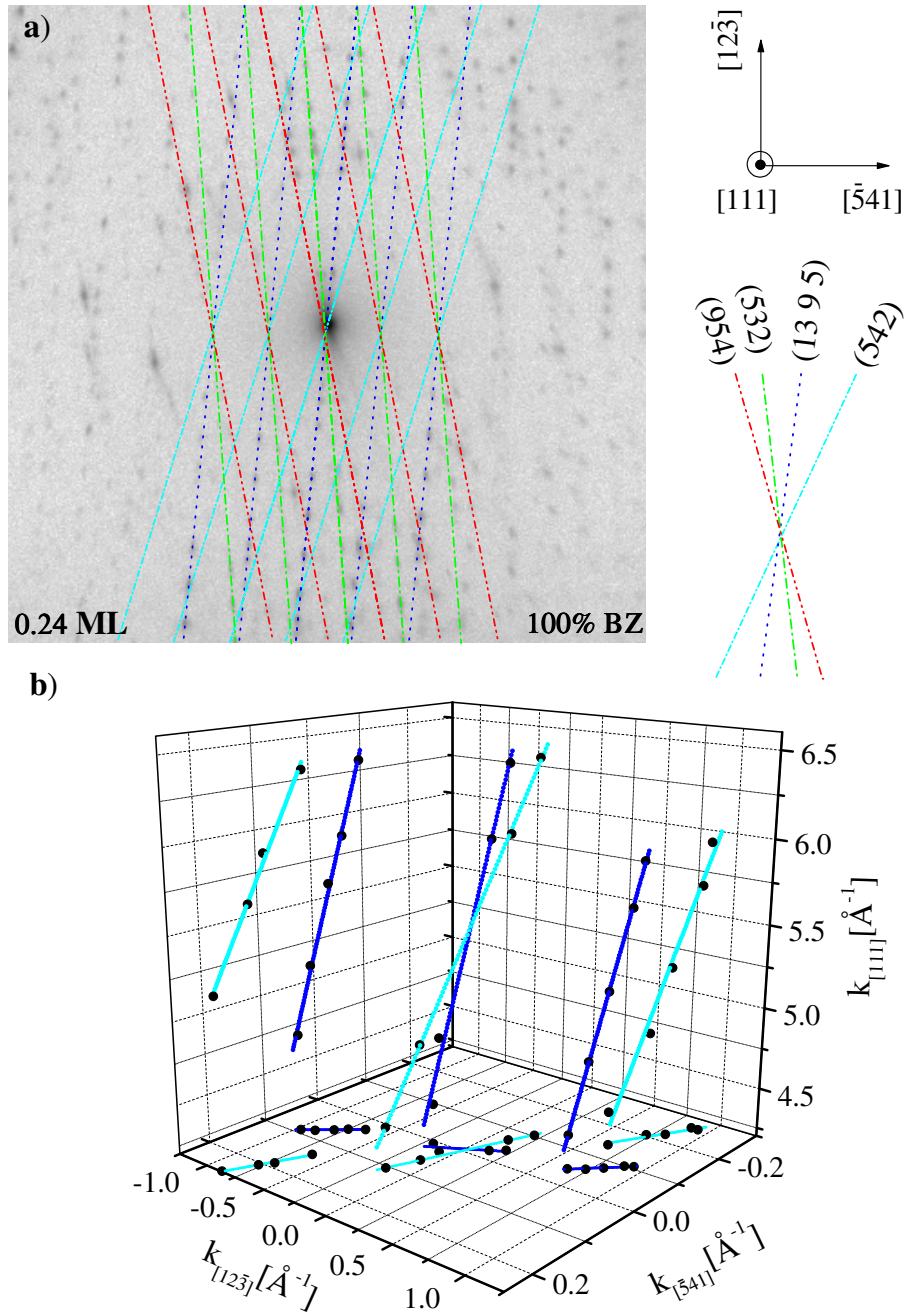
Figure 4.7.: **Facet traces at low coverage.** **a)** Overlaid diffractograms (E_{kin} = 19.0, 23.0, 27.0, 32.0, 35.0, and 40.0 eV; compare figure 2.4) at a nominal PTCDA coverage of (0.24 ± 0.03) ML. Identified facet traces are indicated. **b)** The facet spots associated with the central set of the (13 9 5) and (542) facet traces depicted in a) are plotted in three-dimensional reciprocal space. The colored lines have been fitted to the data points and represent the Ewald rods of the corresponding facets. Details of the analysis are discussed in chapter 2.2.3.
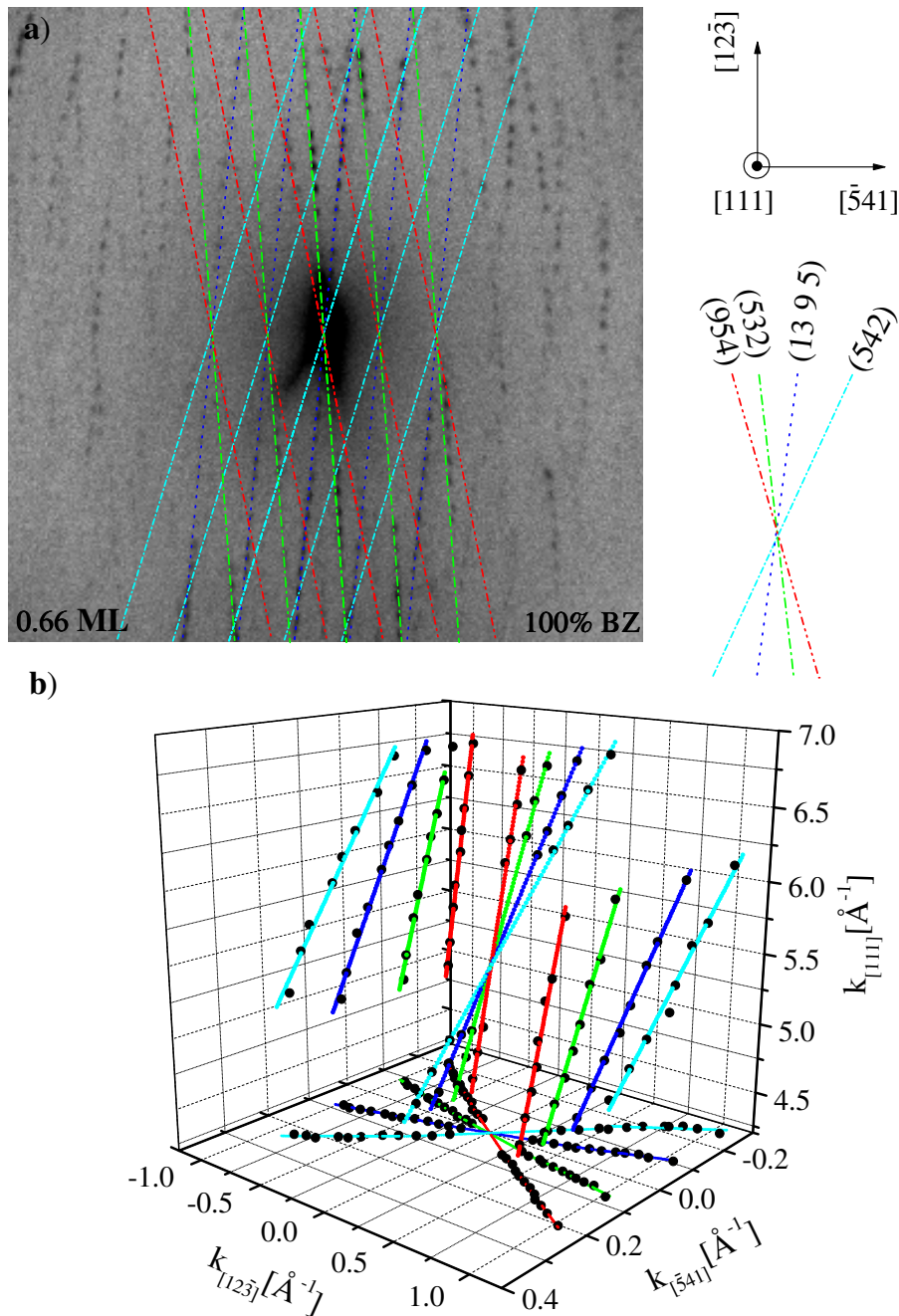
Figure 4.8.: **Facet traces at intermediate coverage. a)** Overlaid diffractograms (E_{kin} = 19.0, 21.0, 23.0, 25.0, 27.0, 30.0, 32.0, 35.0, 37.0, 39.0, 42.0, and 45.0 eV) at a nominal PTCDA coverage of (0.66±0.04) ML. **b)** The diffraction spots associated with the central set of facet traces depicted in a) are plotted in three-dimensional reciprocal space. The colored lines have been fitted to the data points and represent the Ewald rods of the corresponding facets. Details of the analysis are discussed in chapter 2.2.3.

Table 4.2.: **Facet identification.** Results of the analysis of the facet traces presented in figures 4.7, 4.8, and 4.9. The polar angle Θ is given with respect to the (111) direction, and the azimuthal orientation Φ with respect to the $(01\bar{1})$ direction. The facets are assigned in the last line of the table according to Schmitt's model [159].

coverage ML	polar coord.	trace 1	trace 2	trace 3	trace 4
0.24±0.03	Θ	-	-	15.9°±1.6°	13.9°±2.5°
(fig 4.7)	Φ	-	-	8.6°±19.1°	42.4°±7.7°
0.66±0.04	Θ	17.6°±0.8°	17.2°±1.1°	17.7°±0.8°	17.8°±0.7°
(fig. 4.8)	Φ	7.4°±1.0°	14.7°±1.1°	24.6°±1.5°	33.3°±3.6°
0.87±0.04	Θ	17.7°±0.7°	17.4°±0.7°	17.8°±0.8°	17.9°±0.7°
(fig. 4.9)	Φ	9.4°±3.6°	14.8°±0.5°	24.1°±1.7°	26.6°±9.4°
weighted	Θ	17.7°±0.5°	17.3°±0.6°	17.5°±0.5°	17.7°±2.1°
average	Φ	7.5°±1.0°	14.8°±0.5°	24.3°±1.1°	34.0°±3.1°
consistent with		(954)	(532)	(13 9 5)	(542)
nominal	Θ	19.8°	20.5°	19.9°	18.8°
values	Φ	10.9°	19.1°	30.0°	40.9°

scattering (compare table 4.2). The polar inclination of the diffraction rods is found for all types of rods around 17.5° within 0.3°.

Finally, the system has been characterized at a coverage of (0.87 ± 0.04) ML, close to the completed monolayer coverage. Additional intense spots appear in the overlaid data image depicted in figure 4.9a. In contrast to the previously discussed spots, they do not change their lateral position with energy in this projection. Hence, they can be identified as diffraction rods which are oriented along the SPA-LEED axis. Considering the alignment of the crystal, they can be concluded to stand perpendicular on the (111) terraces. As a consequence, they can be attributed to (111) superstructure spots.

In addition to these spots, no further new spots or traces can be identified in the overlaid data shown in figure 4.9a. The model consisting of four different facets explains reasonably well the observed diffraction peak traces. The linear fits resemble in quantity and quality those obtained in the intermediate coverage regime (compare table 4.2).
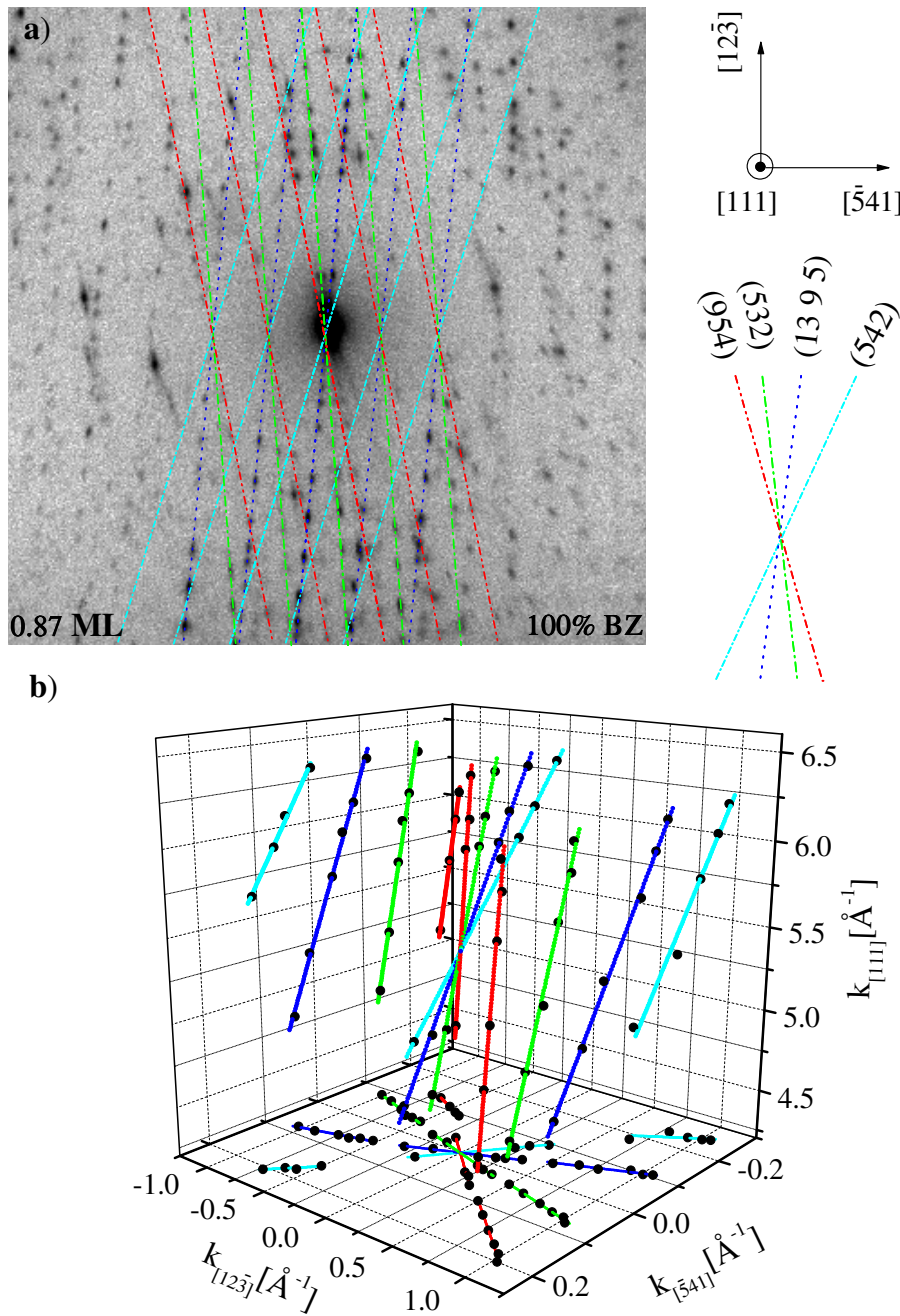
Figure 4.9.: **Facet traces at monolayer coverage. a)** Overlaid diffractograms ($E_{kin} = 19.0$ eV, 23.0 eV, 27.0 eV, 32.0 eV, 35.0 eV, 37.0eV, and 40.0 eV; compare figure 2.4) at a nominal PTCDA coverage of (0.87 ± 0.04) ML. **b)** The diffraction spots associated with the central set of facet traces depicted in a) are plotted in three-dimensional reciprocal space. The colored lines have been fitted to the data points and represent the Ewald rods of the corresponding facets. Details of the analysis are discussed in chapter 2.2.3.

Additional structural information from 1D-line scans

In addition to the four facet types identified in the survey LEED scans, a fifth facet type can be resolved at high coverages which has already been reported by Schmitt [159]. Zooming into the specular facet rods at a kinetic energy E_{kin} of 23.0 eV, additional intensity between two major spots can be identified. The line scans given in figure 4.11 have been recorded along the dotted white line labeled "A" in the inset of figure 4.10. They reveal the presence of an additional peak in the shoulder of the (954) facet peak. Its polar and azimuthal orientation is in agreement with a diffraction rod stemming from (743) facets. The small intensity and the vicinity to the (954) facet trace prevent an identification in the 2D survey data. Its appearance in the high coverage regime is in agreement with Schmitt's observations [159].

Summary

The results of the fits of the 3D-analysis of the reciprocal space are given in table 4.2. The diffraction rod traces can be explained with the same facet model for all three coverages analyzed. The polar coordinates of facets measured for all three coverages have been averaged to obtain an overall morphology measurement in reciprocal space. But to account for the different quality of the data in the three cases, a weighted averaging has been performed.

The polar coordinate Θ measured with respect to the (111) direction varies between 17° and 18° for the four facets identified. Strictly, the orientation does not fit to the coordinates of the facets described by Schmitt [159] within the statistical error bars given in table 4.2 although these results have been measured on the same substrate.

The disagreement can be explained by two different reasons: The distortion of the recorded diffraction pattern depends on energy for the used SPA-LEED apparatus. In particular, the parallel momentum vectors $k_{\parallel}$ are imaged systematically too small, the effect worsening for lower kinetic energies [195]. This error results in inclination angles Θ which are systematically too small. Furthermore, a slight misalignment of the sample can be seen in the raw data: The (00) spot slightly moves with energy, which indicates the (111) terraces of the crystal not to be perfectly perpendicular to the SPA-LEED system axis.

Similarly, the absolute values of the azimuthal coordinate Φ of the facets with respect to the [01$\bar{1}$] direction of substrate do not agree with the model values. Nevertheless, the relative positions of the facets are in good agreement of the model, indicating an overall misalignment of the azimuthal orientation.

Assuming these errors to add for the polar coordinates to the order of $(2 \pm 1)°$ and for the azimuthal coordinates in the order of $(4 \pm 1)°$, which appears very likely, the SPA-LEED measurements of the morphology are consistent with the

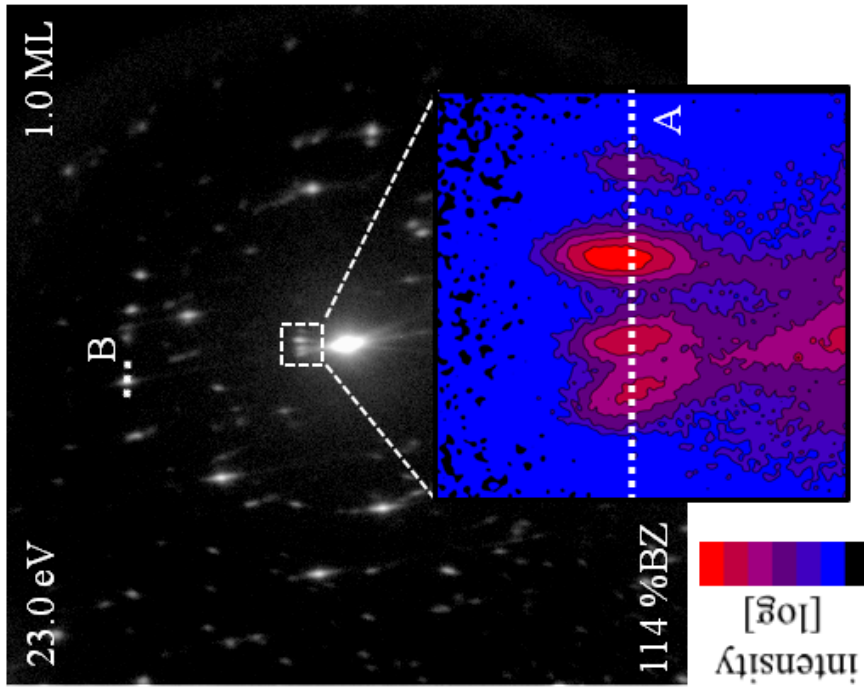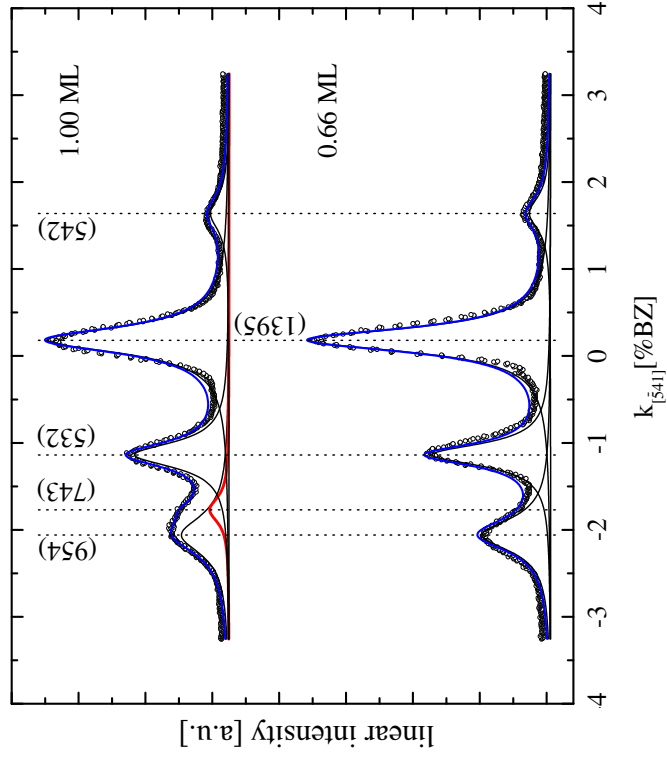Figure 4.11.: **Identification of the (743) facet.** The diffraction peak of the (743) facet appears as shoulder in the (954) facet peak. Its intensity is relatively small compared with that of the other peaks.

Figure 4.10.: **Reduced k-space for line scan mapping.** Zoom into the diffractogram at $E_{kin} = 23.0$ eV. The two line scans "A" and "B" indicated by dotted white lines cover all identified morphologic evolutions in reciprocal space.

75

morphology described by Schmitt [159] for the intermediate and high coverage regime. Therefore, his nomenclature will be used for the facets in the following. It is included in table 4.2.

Finally, I want to note at this point of the discussion that no steep facets with polar angles in the order of 27° have been observed in this experiment.

4.5.2. In-situ mapping of facet formation

In the previous chapter, intermediate states of the system have been characterized in reciprocal space. The setup, equipped with a conically shaped front end, allows to take the experiment further: Based on the gathered information, the formation of the relevant features can be measured in-situ during growth with reasonable time resolution. The results of these experiments will be discussed in this section.

2D snapshots

A first idea of the evolution of the morphology can be obtained by looking at 2-dimensional scans of the reciprocal space which contain the specular facet rods of second order. The corresponding area in k-space is indicated by dashed white lines and as insetin figure 4.10. The respective (and all following) in-situ experiments are performed at a kinetic energy E_{kin} of 23.0 eV. This energy corresponds to a scattering phase S of 1.84 for the investigated Ag(111) surface. The relative proximity to the in-phase condition has been chosen because it permits an optimal time resolution: Under these conditions, the specular facet spots are both sharp and close enough to cover all relevant features in a small volume in reciprocal space. Nevertheless, the energy of the electrons is still far enough out-of-phase that the spots can still be separated.

In the 2D in-situ experiments, a quadratic measurement window of edge length 6.4 % of the brillouin zone (BZ) has been used. In figure 4.12, however, only 6.2 % of the BZ are depicted on the horizontal axis since edge artifacts dominate the omitted regions. The employed sampling raster of 200×200 measurement points translates into a lateral resolution of (0.032 ± 0.003) % BZ. Each point has been sampled for 0.50 ms. An overall acquisition rate of 49 s per image has been achieved with these parameters. Considering the deposition rate of PTCDA in the respective experiments, this rate corresponds to a coverage increase of (0.044 ± 0.005) ML between two consecutive measurements.

Despite these optimization efforts, the acquisition time per point remained relatively small. To improve the signal to noise level, three consecutive scans have been averaged to obtain the 2D-images depicted in figure 4.12. Furthermore, the count rate has been normalized to the total intensity of the individual scan, and a logarithmic color scale has been chosen.
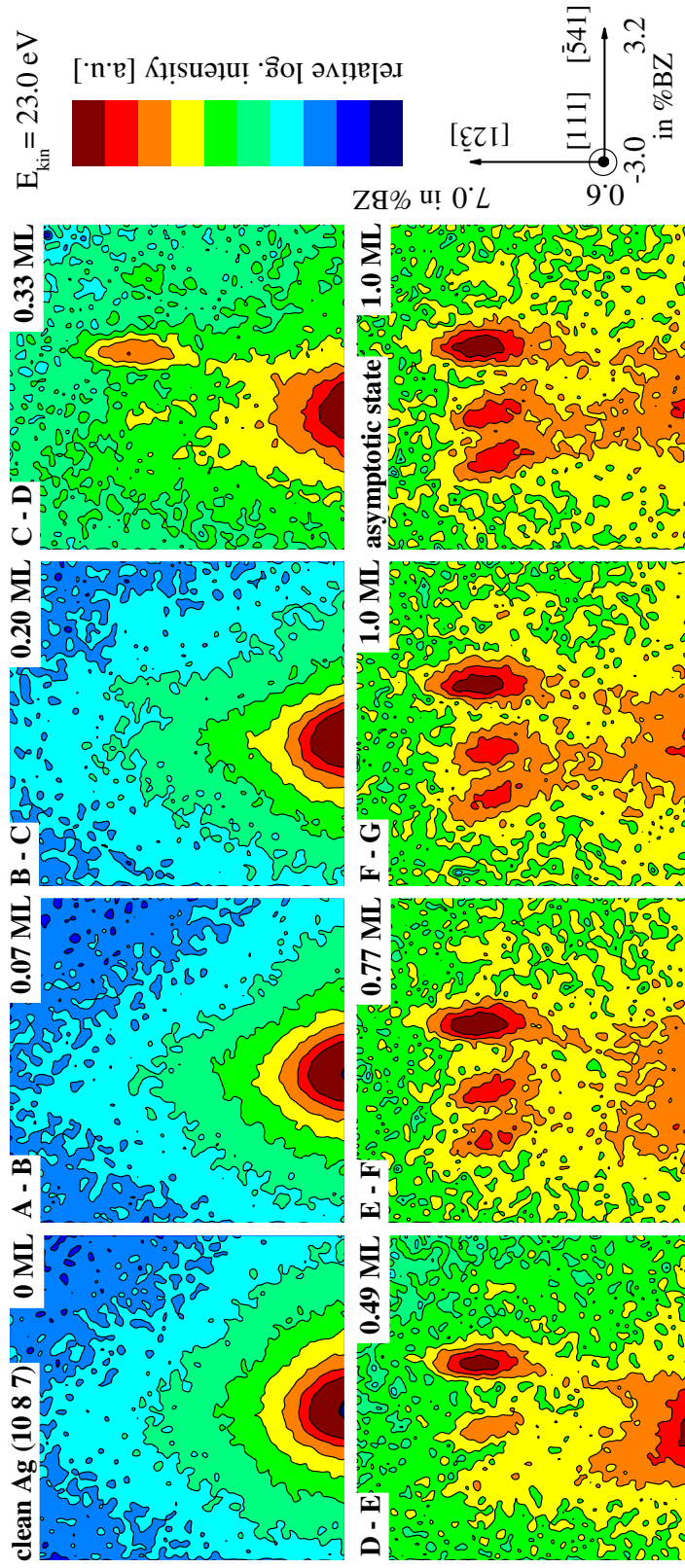
Figure 4.12.: **Facet evolution in 2D snapshots.** The SPA-LEED images have been taken from an in-situ measurement of the adsorption of 1 ML of PTCDA on Ag(10 8 7). Coverages have been chosen which are in between the characteristic points of the corresponding stress change curve (figure 4.6). The contours of the intensities are given in a logarithmic color code.

Eight diffraction patterns are compiled in figure 4.12. They correspond to the critical coverage regimes of surface stress changes of this system (compare 4.6). The major trends can be qualitatively identified by inspection.

At low coverages, the data is still dominated by diffuse scattering of the (00) spot of the (10 8 7) surface (bottom part of the depicted segment in figure 4.12). Its distribution, however, changes in the first three images: The "corona" is basically symmetric with respect to the vertical axis for the clean crystal. This symmetry is, however, broken in the vicinity of the (542) facet spot with beginning coverage (A-B). Subsequently, the (13 9 5) facets evolve as first pronounced facet types. The corresponding specular spot reaches its maximum intensity at point (D-E). It remains the most intense facet spot for the rest of the experiment. In addition, two further facet spots occur at this coverage which belong to the (532) and (954) facet rods. Upon close inspection, an increase of intensity between the latter two facet spots can be observed in the further development (E-F, F-G), which indicates the formation of (743) facets. Finally, it is noted that the intensity of the diffuse scattering of the (00)-spot has almost vanished from the field-of-view in the asymptotic state.

1D line scans

The 2D data indicates that the dynamics of the facet formation can be traced with 1-dimensional line scans without loss of information. The scans were recorded at 23 eV along the [$\bar{5}$41] direction. All facet spots could be traced within a single line scan in, or at least, close to their maximum intensity (compare the indicated line scan "A" in the inset of figure 4.10).

This reduction to one dimension improves statistics, lateral, and even temporal resolution: The integration time can be raised to 15 ms per point, significantly improving the signal-to-noise ratio. Each line scan (width 5.68 % BZ) can be sampled at 866 points, corresponding to a nominal resolution of (0.007 ± 0.001) % BZ. On top, the time of a single scan can be lowered to 27 s resulting in a "coverage resolution" of (0.023 ± 0.003) ML/scan.

The line scans obtained in a representative experiment are plotted against time in figure 4.13. They are depicted in a pseudo 3D graph with a logarithmic color scale. Again, the broad intensity background at the beginning (bottom of figure 4.13a) can be explained by the diffuse scattering at the slope of the (00) spot of the (10 8 7) surface. Five features (F1-F5) emerge with increasing PTCDA coverage which can be assigned to the specular reflections from the indicated facets. The sequence of the facet peaks is in accordance with the observation in two dimensions. The better resolution, however, allows the (542) facet (F_1) to be identified at very low coverages. Furthermore, the (743) facet (F_5) now appears unambiguously as pronounced shoulder between the (954) and the (532) facet peaks (F_3 and F_4).

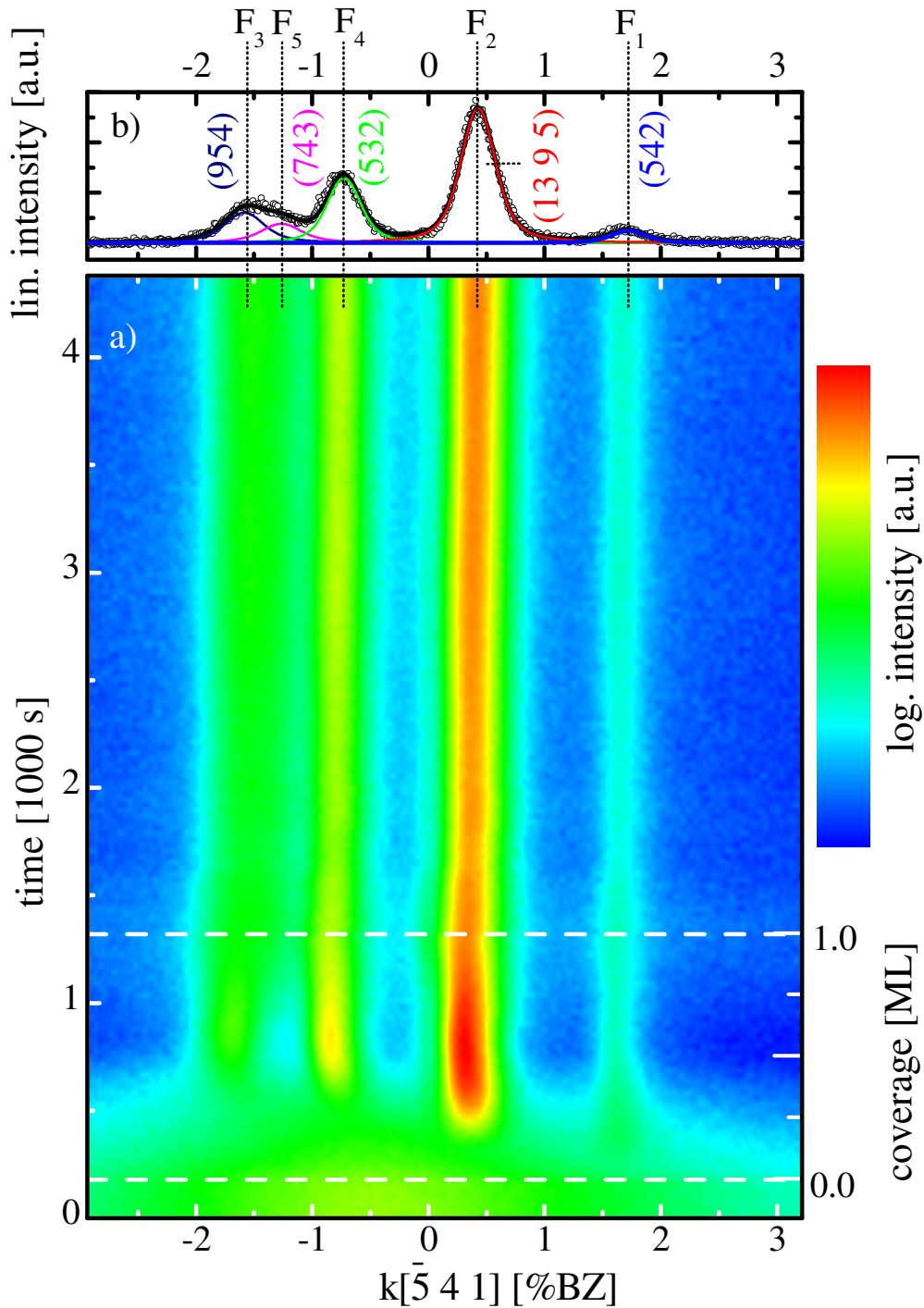At last, the better signal-to-noise ratio reveals the intensity of the most prominent

Figure 4.13.: Growth of facets during adsorption. a) 165 consecutive line scans were taken during the adsorption of 1 ML of PTCDA on Ag(10 8 7). They are put together to a pseudo 3D graph. Their intensity is given in a logarithmic color scale. The exposure time is indicated by dashed lines and converted into coverage by the scale on the right side. **b)** The 1-dimensional fit consists of five different facets as applied to the last scan of figure 4.13a.

features F_2 to F_4 (the (13 9 5), the (532), and the (954) facet) to be modulated in the depicted data. It undergoes a maximum at intermediate coverages in each case, indicating a further structural transition which reduces the population of the respective facets.

Mapping the facet evolution

The analysis of the data, however, can be taken further than just a qualitative discussion of the trends.

For that purpose, the 165 line scans forming figure 4.13a have been fitted consistently according to the example presented in figure 4.13b to map the faceting dynamics. Voigt profiles with a common Gaussian width, which is attributed to experimental broadening induced for example by the electron gun, provide an optimal description of the measured peak shapes. All scans were fitted in a single coupled fit. The relative peak distances and Gaussian widths were treated as identical parameters for all peaks.

The intense and structured background in the initial coverage region caused by the diffuse scattering of the (00) spot makes it necessary to fit in three separate groups: The ensemble of (954), (532) and (743)spots is simultaneously analyzed, while the early appearance of (13 9 5) and (542) facets requires an individual treatment. No further data normalization was performed beyond a simple subtraction of linear backgrounds for the respective ensembles before fitting.

The derived peak intensities are depicted in figure 4.14 according to the color code defined in figure 4.13b. All facet spots rise continuously. Hence, their time evolution can be regarded well resolved within the utilized experimental parameters. The fits reveal the rare (542) facets to be formed immediately after opening the shutter, which indicates defects to be bunched first. The predominant (13 9 5) facets are formed next. The azimuthal counter facets (532) and (954) appear nearly simultaneously within the resolution of the experiment, while the (743) facets only occur when a coverage of half a monolayer has been surpassed. After the shutter has been closed, it still takes approximately 20 minutes until the asymptotic value of the intensity is reached.

The fit results of the 1-dimensional data sets can be verified by comparison to the development of the complete intensity of the individual peaks. The latter were deduced from the 2-dimensional data sets which are the basis of figure 4.12. Considering the data quality, a slightly different technique was used to derive the intensity evolution: Rectangular windows comprehending a single facet peak were defined in the 2-dimensional surveys. Their intensities were then simply integrated. The deduced intensity evolutions are comprised in figure 4.14.

In order to ease the comparison of the two different approaches, the data sets were normalized to their asymptotic values. Despite the lower resolution of the 2-dimensional data set, the onsets of the peak formations are clearly confirmed by
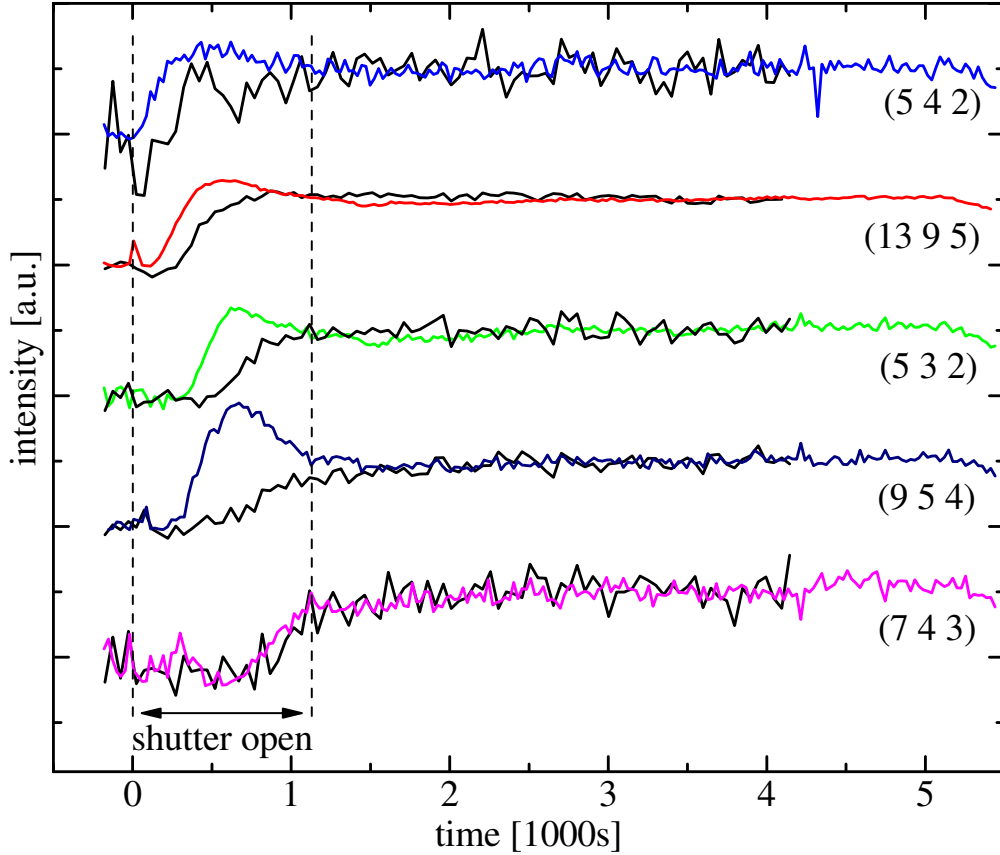
Figure 4.14.: **Comparison of 1D line scans vs. 2D intensities.** The colored data was obtained by fitting the model peaks of figure 4.13b to the 1D line scans. The black lines have been obtained by evaluating the intensities of the specular facet peak intensities measured with 2D scans as depicted in figure 4.12.

the comparison.

The precise intensity evolutions of the peaks, however, differ especially for the most dominant features. This can be explained by the fact that the chosen "window-integration" in the 2-dimensional case averages over a larger area in k-space, whereas the line scan is focussed on the narrow maximum of the feature. Since the intensity of the diffuse scattering is orders of magnitude smaller than the central intensity of a diffraction spot, it can only be identified in the results when a significant number of diffraction centers, i.e. facets, are present. Therefore, the integral measurement, which averages over the complete area of the peak in k-space, lags behind the 1-dimensional one.

In addition, external effects on the 1-dimensional data acquisition were investigated. As discussed in appendix C, they do not affect the result of the previous analysis.
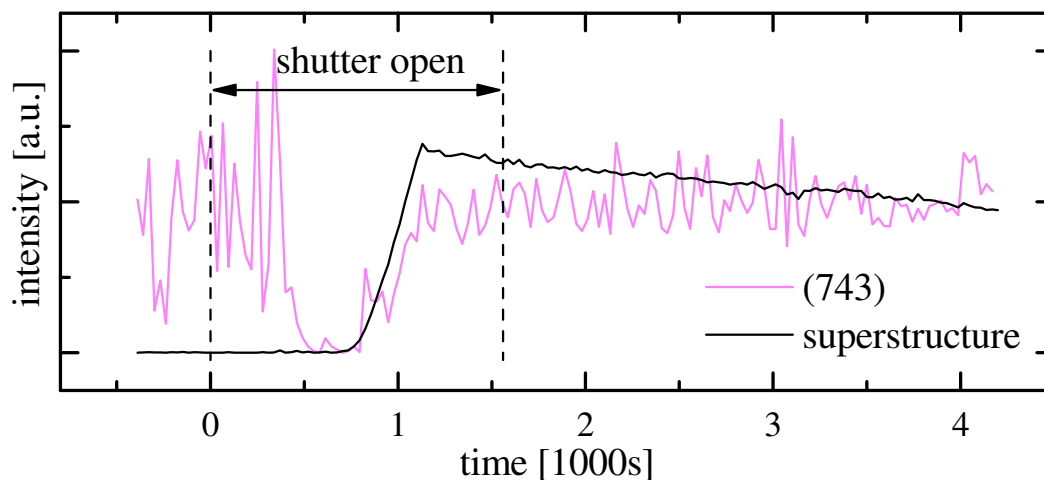
Figure 4.15.: **Simultaneous growth of (743) facets and (111) superstructure.** The growth of the specular (743) facet peak (colored) and the specular peak of the (111) facet (black line) was monitored by SPA-LEED line scans within the same experimental run. The fit result demonstrates their simultaneous rise. The apparent initial noisy intensity of the (743) is caused by background intensity stemming from inelastic scattering of the (00) peak.

Simultaneous formation of (743) facet and (111) superstructure

Not only facet spots, but also superstructure spots (see chapter 4.5.1) have been monitored in-situ by 1-dimensional line scans. In a separate experiment, line scans through the facet peaks (identical to those used in the previous paragraphs) and across a superstructure spot were alternatingly recorded during formation of the faceted PTCDA/Ag(10 8 7) interface. Both line scans are indicated in figure 4.10 (labeled "A" and "B"). In order to preserve the time resolution, shorter integration times were used.

In analogy to the previous 1-dimensional in-situ data, the rise of the individual facets was mapped by fitting the data sets. Figure 4.15 reveals the perfect correlation of the rise of the (743) facet (F_5 in figure 4.13) and the growth of the superstructure spot. Facet and superstructure form completely simultaneously within the resolution of the experiment, which indicates their mutual dependence.

In addition, when looking at the data given in figure 4.15, it can be noted that the fit result indicate noisy intensity of the (743) face even in advance to PTCDA exposure. This is an artifact of the automated fitting routine: The lower signal to noise ratio makes the background subtraction more difficult as in the previous cases, especially at the beginning of the experiment when the textured background of the diffuse (00) spot intensity is present. All intensity remaining after the background subtraction is described by the routine using the fit model, which leads to the
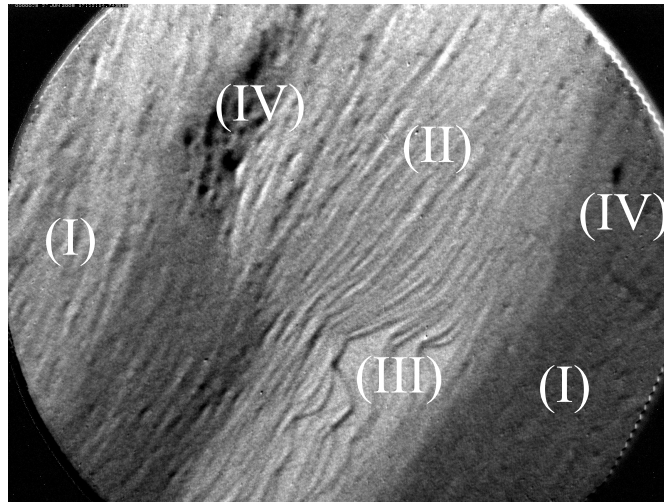
Figure 4.16.: **Starting morphology for a LEEM in-situ experiment.** Surface areas have been chosen for the LEEM in-situ experiments which contain areas with regular step densities (I,II) and different defects (III, IV). The field-of-view is 2 μm.

artifacts observed. Fortunately, the structured diffuse background of the (00) spot has vanished when the (743) facet really forms, which is confirmed by figure 4.12.

4.6. LEEM study of the system

The in-situ mapping of the reciprocal space described in the last chapter has revealed major larger steps during the formation of the morphology of the system. Although this electron diffraction technique is very precise with its high resolution in k-space, the method suffers from the fact that it averages over a large sample area due to an electron beam with a size of approximately 5 mm in diameter.

In order to gain complementary insight into the relevant scales of the system, the interface and its formation have been investigated using low energy electron microscopy (LEEM). The results provide further information on the in-situ processes of faceting and long-range order formation. In addition, the influence of local morphology and of temperature on the growth can be studied by this technique.

4.6.1. Faceting in real space

The formation of the PTCDA/Ag(10 8 7) interface is addressed in this section once again in order to corroborate the previous conclusions on the morphologic evolution. In particular, the microscopic data will provide additional information on the low-coverage regimes in which the surface stress does not alter significantly.

Measurement conditions

As mentioned in chapter 2, the experiments were performed using the SMART spectro-microscope at BESSY in Berlin. More specific remarks on the measurement conditions are given in the following paragraphs.

First, it must be mentioned that again, a special (10 8 7)-crystal was used for the experiment. Due to the high electric field on the sample surface the standard sample mount requires front and back side of the sample to be flat and parallel to each other. Since the wedge-shaped SPA-LEED crystal violates this requirement, a suitable round crystal with a diameter of 10 mm has been prepared following the procedures employed for the cantilever crystals.

The crystal was kept at a stable, elevated temperature between 418 and 612 K during the PTCDA adsorption. In order to minimize thermal drifts, the heating current was kept constant within 0.01 A in the following experiments. Nevertheless, the sample temperature drift was still smaller than 1 K over the course of an adsorption experiment.

The PTCDA molecules were evaporated with an adsorption rate of (0.052±0.005) ML/min. The data supports the sticking coefficient to be constant, i.e. the coverage being linear with time. The fluorescence screen was imaged by a CCD camera. Every 6 s a new image was taken with an integration time of 4 s. Altogether, a coverage resolution of (0.0052 ± 0.0005) ML has been achieved.

Electrons with an effective kinetic energy of $E_{kin} = 2.0$ eV were used in the following experiment. In the in-situ experiments, the specular spot of the (111) terraces on the surface is imaged (compare chapter 2.2.2). Therefore, (111) terraces appear bright, while the growing high-index facets appear dark. As known from previous experiments [20, 43], domains of PTCDA superstructure have enhanced intensity at this kinetic energy and appear brighter.

Working with a microscopic technique, the choice of the imaged sample area is of great importance. A field-of-view of 2 μm has been chosen because it is both, small enough to be able to resolve the relevant structures (10 pixels correspond to 12.2 nm in this magnification), and nevertheless still big enough to contain a representative choice of starting morphologies. Areas like the one depicted in figure 4.16 have been selected. This region contains large terraces of ordered step trains (indicated by (I),(II)), which represent the dominant morphology of the surface. Additionally, two different types of morphologies are located within the field-of-view: Area (III) consists of large (111)-terraces, while areas (IV) is characterized by a high step density.

Mapping the morphologic transitions

The adsorption of PTCDA on Ag(10 8 7) at a substrate temperature of 528 K is depicted in figure 4.17. The data has been selected according to the critical
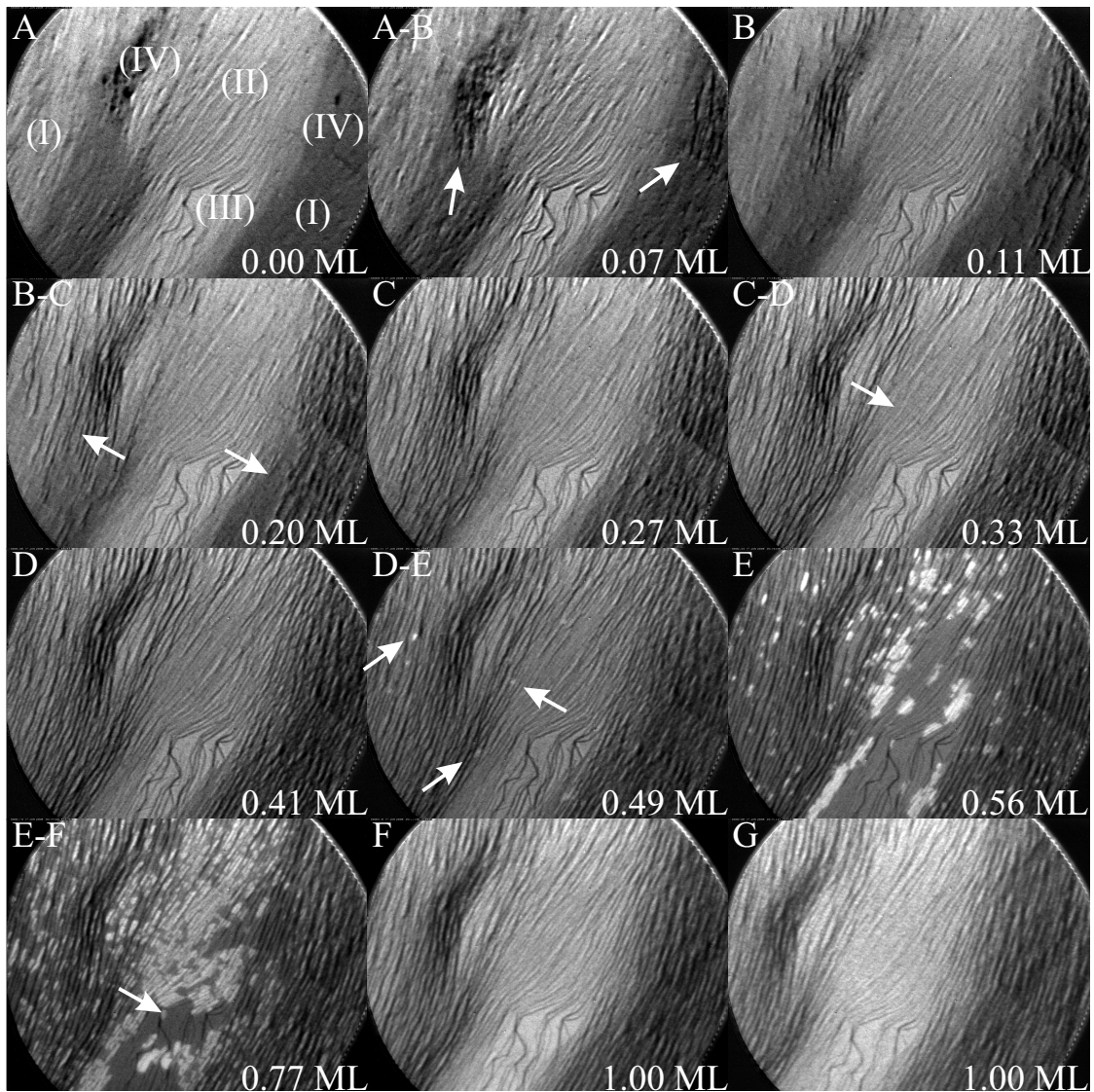
Figure 4.17.: **Characteristic stress regimes in LEEM.** The bright-field LEEM images (field-of-view: 2 μm) have been taken at an electron kinetic energy of E_{kin}=2.0 eV and a substrate temperature of T=528 K. Images are chosen to correspond to the characteristic regimes identified in the surface stress change curve. The arrows point to areas with changing morphology at the respective coverage. The capital letters in the upper left corner of each frame label the coverage regime in agreement with those of figures 4.6 and 4.12. In image A, the labels for the different morphologies in the field-of-view are repeated (compare figure 4.16) to ease the comparison with the text.

coverages identified in chapter 4.4.2. They are labeled according to the definitions in figures 4.6 and 4.12. The regions to which the following discussion refer are marked by white arrows.

The first adsorbed molecules nucleate in the regions with the highest step densities (IV). The contrast in the respective regions changes immediately (A-B). Larger facets, which can be identified as black features, form starting from the nucleation centers. At a coverage of 0.11 ML (point B), the corresponding areas are completely faceted, while no contrast change can be identified for the further coverage development.

In the following coverage regime up to a coverage of approximately 0.27 ML (B-C), the large homogeneous terraces (I) facet. The new structures start to grow in the vicinity of the early nucleation centers.

Within the next 0.14 ML (points C to D), mainly the contrast in the middle region (II) changes. It is dominated by the curvatures of the defect regions (III) and (IV). The average azimuthal orientation of the steps in this surface area therefore deviates from the overall one. At a coverage of 0.41 ML, the depicted area is completely faceted.

The first stable domains of PTCDA superstructure on (111) terraces appear as bright white spots at a coverage of approximately 0.49 ML, labeled D-E. They nucleate on narrow (111) terraces, limited by long high-index facets in regions (I) and (II). Subsequently, more and more (111) terraces get covered with PTCDA domains. The relatively large (111) terraces in region (IV) are covered in a final step. Their structure is not affected by the large-scale transitions observed, i.e. step bunches do not "populate" the flat terraces. The local morphology is hence still imprinted by the original defects.

Contrast differences cannot be identified after shutter closure in the LEEM data. Annealing effects or a further restructuring are therefore not backed by the LEEM results. But the (743) facets are very similar in azimuthal orientation to other facets formed before ((954) and (532)). In addition, SPA-LEED results indicate the density of (743) facets to be small. Therefore, the associated change in contrast is so subtle that it is not surprising that they cannot be identified in LEEM.

Finally, it is found that from the point of view of microscopy, the onsets of the different structural phases are not as sharp as the previous discussion might imply. The different regimes smoothly pass into each other. Thus, strict onsets are difficult to identify in contrast to the case of the in-situ SPA-LEED data. Nevertheless, the discussion in the last paragraphs shows that the classification of the adsorption period according to the characteristic stress regimes fits to different growth regimes in the LEEM data, too.

4.6.2. Influence of the local morphology

Besides its capabilities in time-resolved imaging, a LEEM experiment offers the possibility to directly connect a real space experiment (both in bright and in dark field mode) with a reciprocal space measurement (LEED). Hence, the identical area on the sample can be investigated by both, microscopy and diffraction. Since the instrument is able to work on the scale of the typical domain sizes of the faceted areas in these modes, a comprehensive insight into the local morphology can be gained. Thus, a strong dependence of the faceting process on the local morphology can be proven. Moreover, the homogeneous growth of facets in mesoscopic domains can be studied.

Local dependence of faceting

In the previous sections, the average morphology of the interface was characterized. Independent of the care of the surface preparation, a certain amount of defects in the starting morphology is unavoidable given the limited perfection of metal crystals. The following data will show that these variations can strongly influence the local faceting behavior.

In figure 4.18 an inhomogeneous section of the PTCDA/Ag(10 8 7) interface (prepared at 573 K) is depicted. The survey given in figure 4.18b is composed of five overlapping LEEM images taken consecutively along the horizontal axis. The mesoscopic terrace in the center (labeled "(I)" in figure 4.18) is limited by larger, wavelike protrusions and more pronounced defects on the right hand side. A schematic vertical projection is given in figure 4.18a as a guide for the eye. All steps are bunched and the faceting transition is completed.

Three colored circles (labeled (I) - (III)) indicate areas of different composition of morphology. The homogeneity of the structures decreases from (I) to (III). The marked areas on the samples have been investigated in reciprocal space, too. The corresponding LEED patterns are given in figure 4.18c labeled $\widetilde{(I)}$ to $\widetilde{(III)}$. Based on these LEED patterns, the facets have been indexed following the model by Schmitt [159]. This assignment is used consistently throughout this thesis.

Area (I) is located on the homogeneous terrace in the center. The interface consists of an almost perfect grating-like structure built up mainly of (542) and (13 9 5) facets as counter facets to the (111) terraces. In addition to these two predominant facets, a weak (532) signal is detected in LEED.

This signal evolves from LEED patterns $\widetilde{(I)}$ to $\widetilde{(III)}$, peaking in $\widetilde{(II)}$. One can interpret this facet type to be formed in area (II) to balance the average orientation of the (13 9 5) and (532) facets in order to preserve the pristine step direction. In area (II), this pristine step direction differs from the one in area (I) due to the wave-like protrusion labeled W in figure 4.18a.

The composition of facets complicates even more in area (III), which is dom-
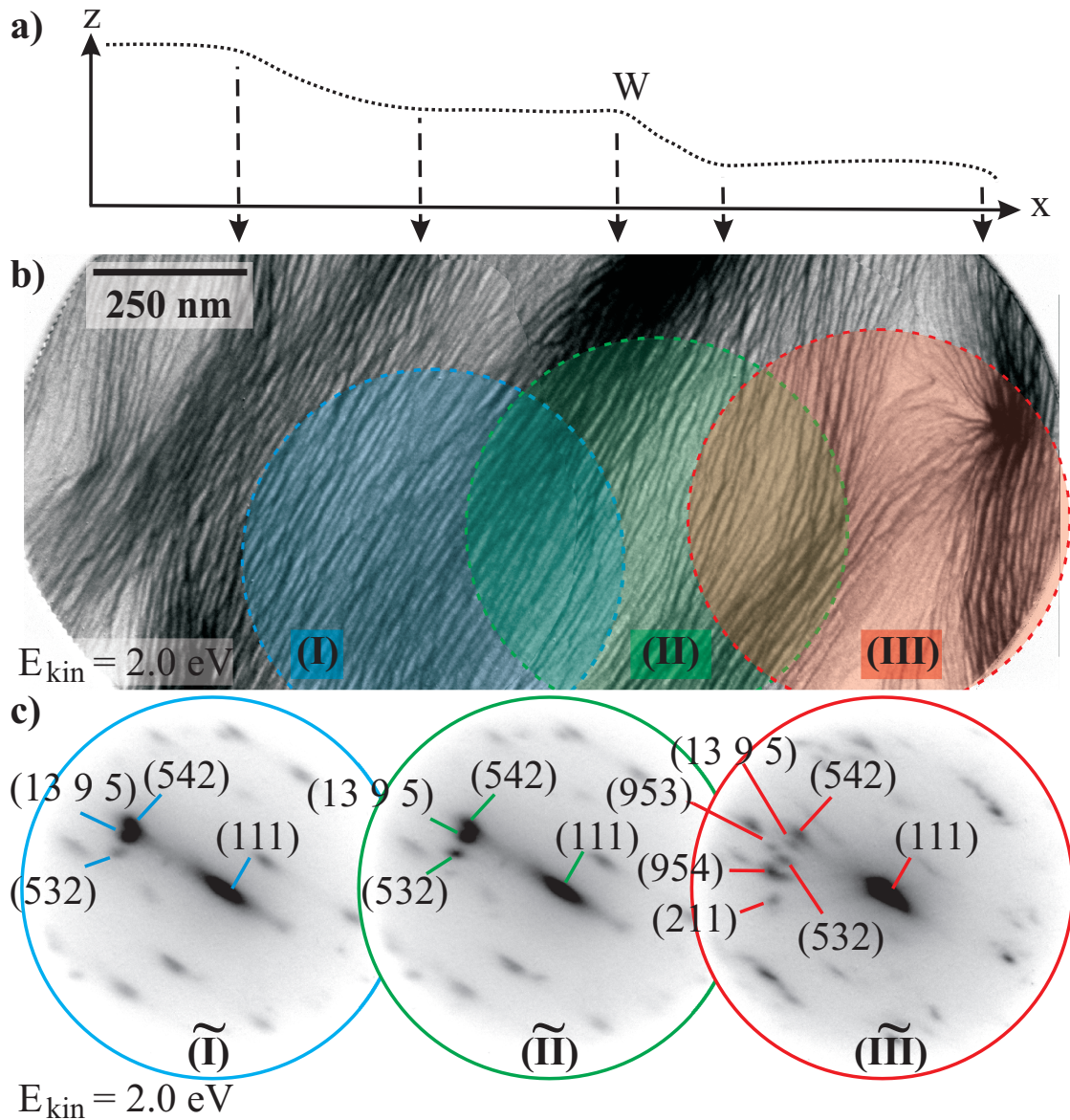
Figure 4.18.: **Local dependence of faceting. a)** Schematic of the vertical morphology seen in the survey given in b). The "z"-axis denotes the direction out of the image plane depicted in b), while "x" corresponds to the long edge of image b). **b)** The depicted survey is composed of 5 LEEM images of a field-of-view of 2 μm taken in bright-field mode at a kinetic energy of 2.0 eV. The PTCDA/Ag(10 8 7) interface has been grown at a substrate temperature of 573 K. **c)** The three local LEED images ($(\tilde{I})$, $(\tilde{II})$, and $(I\tilde{I}I)$), taken at a kinetic energy of 2.0 eV correspond to the three areas circled in b). The identified facet spots are labeled according to Miller's notation, based on the model by Schmitt [159]. Additional spots are due to the PTCDA superstructure on the various terraces.

inated by two large defects consisting mostly of (111) terraces. The grating-like arrangement of the facets has vanished there. The corresponding LEED pattern $\widetilde{(III)}$ shows a large number of different facets with spot intensities on a similar level. In addition to the already mentioned (542), (13 9 5), and (532) facets, also spots attributed to (211), (954), and (953) facets can be identified. It should be mentioned that, while most of the facets have been described by Schmitt [159], the last facet type has not been reported before for this system. The large variety of facets is necessary to decorate the edges of the defects since the local orientation there is in complete contrast to the average orientation.

In summary, the area depicted in figure 4.18b is composed of a surprising diversity of morphologies within a length of 1.0 μm. The homogeneous area (I) fits to the intuitive picture gained from the averaging diffraction experiments before. But the completely different morphology found in close vicinity to the homogeneous, "representative" area (I) demonstrates that the microscopic morphology can significantly deviate from this average conception.

Finally, I want to point out that larger defects responsible for such a local deviation from the average orientation are difficult to be identified by high resolving microscopic techniques like STM. Hence, a generalization of STM observations bares the danger of misinterpretation.

Predominant and minor facets in real space

The LEED images discussed in the previous paragraphs reveal the complex composition of different facets which forms the regular grating pattern. The understanding of the morphology can be driven further by dark field LEEM (compare chapter 2.2.2).

The spatial distribution of individual facet types is directly accessible with this technique. In figure 4.19, a complete spatial analysis is performed for a homogeneous area on a PTCDA/Ag(10 8 7) interface. The respective sample was grown at 573 K. The LEED pattern contains three dominating types of facets: (532), (954), and (111). In addition, one specular spot associated to (13 9 5) facets can be identified.

The corresponding real space images are depicted in the center and the right column of figure 4.19. Elongated bright stripes are imaged, which can be assigned to specific facets due to the imaging mode. The (111) terraces form a nice regular pattern across the whole field-of-view. The density of the other three facet types, however, is not homogeneous. The (532) and (954) facets dominate different areas, which smoothly fade into each other in the center of the depicted area. They are arranged in a regular grating-like pattern within such an area.

In the area selected as an example, the (13 9 5) facets form a minor species. They are homogeneously scattered within the (532) domain to sustain the local average pristine step direction.

E_{kin}= 2.0 eV

(532) (1395)

(111)

(954)

Sel. Area (LEED): 1 μm
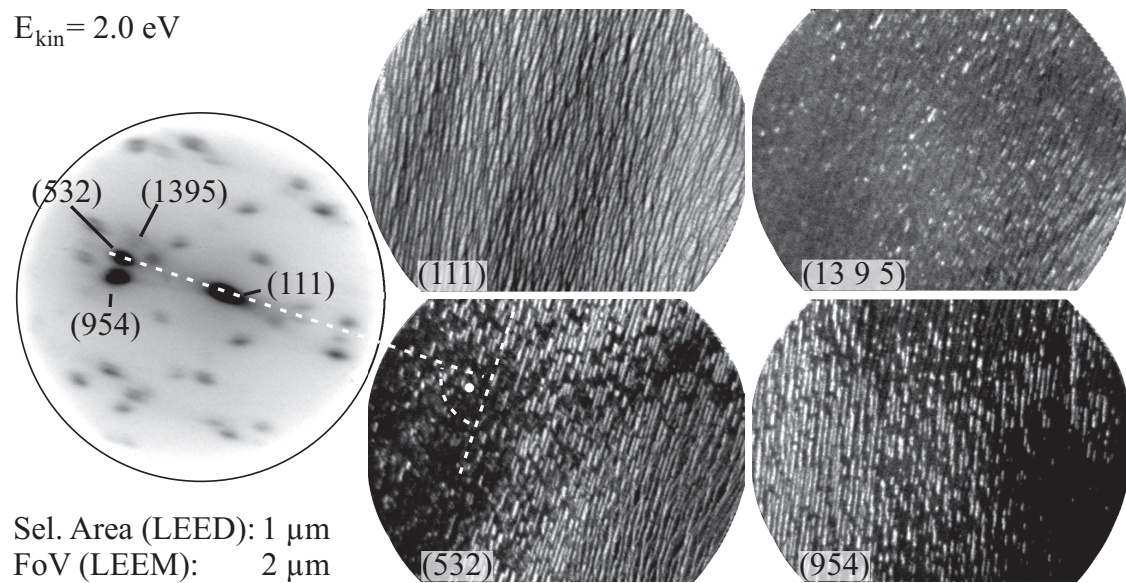FoV (LEEM):   2 μm

(111)

(13 9 5)

(532)

(954)

Figure 4.19.: **Local morphology deconvolution.** The depicted data set (taken from a preparation at 573 K substrate temperature) exemplifies the complementary information on the local morphology accessible by combining different LEEM imaging modes. The real space images (field-of-view of 2 μm) have been taken in dark-field mode by imaging the specular facet spots labeled in the LEED pattern (selected area of 1 μm). Directions in reciprocal space correspond to directions in real space by the construction indicated by white dashed lines for the (532) facets.

Finally, the data set depicted in figure 4.19 demonstrates that the directions in the LEED pattern directly correspond to the directions in the real space image due to the imaging properties of the LEEM apparatus. In fact, each imaginary line connecting specular facet spot and the (111) spot in the LEED pattern would stand perpendicular on the respective dark-field images of the facet stripes as exemplified for the (532) facet in figure 4.19.

4.6.3. Influence of the growth temperature

In addition to the thermodynamic driving forces, kinetics might play a decisive role in the faceting process, too. Therefore, the growth behavior has been investigated in the temperature range between 420 K and 620 K in order to learn more about the dynamics of nucleation.

Steep facets

At first, a highly interesting detail is discussed. At the lowest growth temperature of 418 K in this study, steeper facets have been observed than the ones discussed up to now. While all the latter have been inclined by approximately 20° with respect to the (111) orientation, also a facet of approximately 25° has been observed by LEED in the low-temperature growth regime.

In figure 4.20 the respective data is given. The selected area in which the steep facet has been found is depicted in figure 4.20b. It is situated in the vicinity of a defect (labeled D). Nevertheless, the morphology is not exceptionally different when compared to those observed at similar spots for other growth temperatures in LEEM.

The morphology of this spot has been studied by energy-dependent LEED. Nine diffraction patterns in an energy range between 1.5 and 6.0 eV have been analyzed. Three representative patterns of this energy stack are given in figure 4.20c. The imaged Ewald spheres have been cut out of the raw data. Their size ratio is prevailed in figure 4.20c. The spots analyzed in figure 4.20a are labeled by arrows. The respective traces have been fitted with straight lines in k-space; the results are indicated by dashed lines. Inclination angles of $\Theta_1 = (18.2 \pm 4.5)°$ and $\Theta_2 = (25.0 \pm 4.5)°$ are deduced with respect to the specular facet spot of the (111) terraces. Together with their azimuthal orientations, these values are in good agreement with (13 9 5) and (25 13 7)-facets.

Dark-field images of predominant facets

Having made this annotation on the morphology, the facet-sensitive or dark-field imaging introduced in figure 4.19 will be used to study the temperature dependence of the facet dimensions in the remainder of this section.
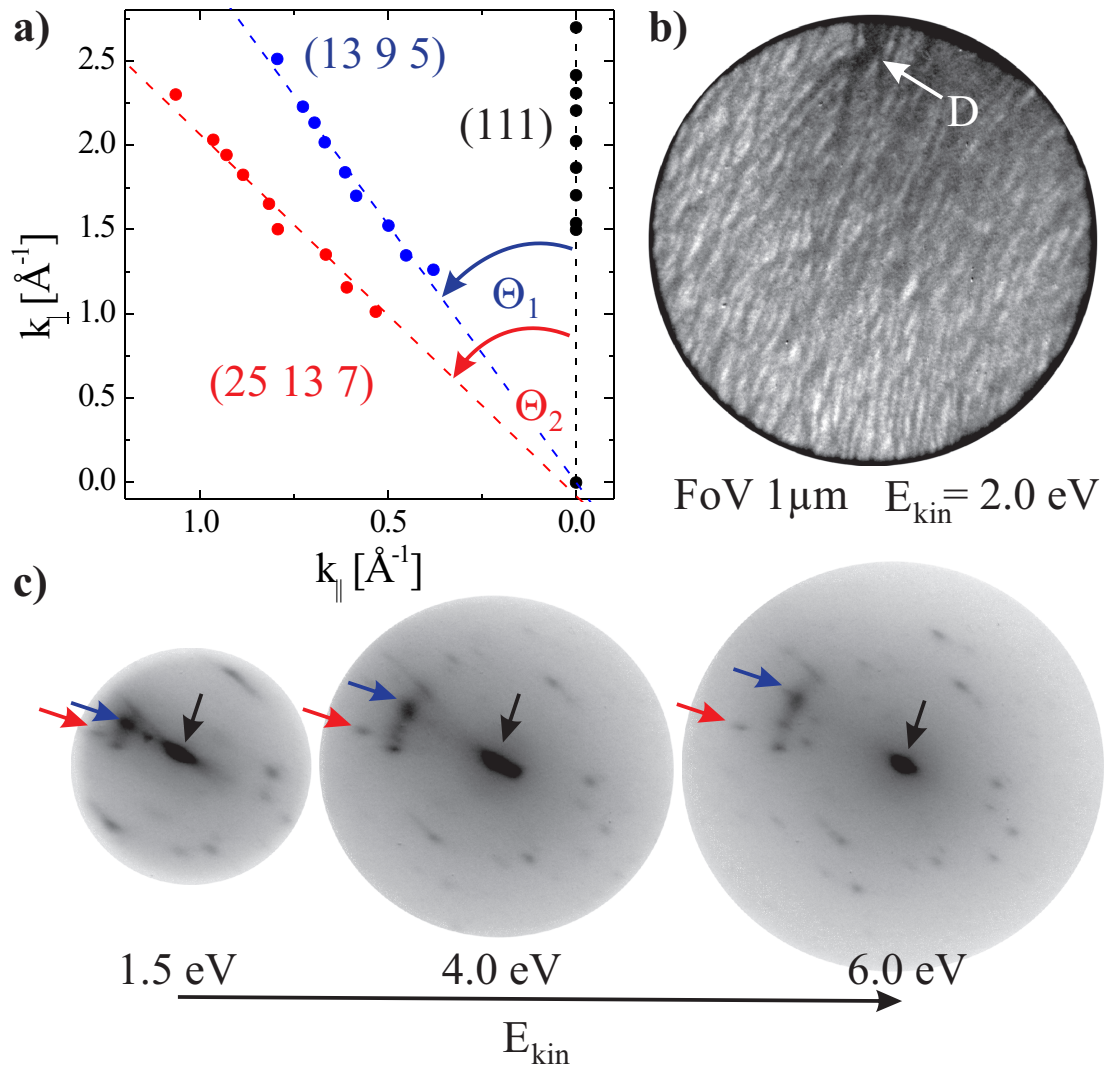
Figure 4.20.: **Steeper facets. a)** The analysis of the energy-dependence of spot positions of an interface grown at 418 K proves the existence of a second facet type with a steeper facet of inclination $\Theta_2 = (25 \pm 3)°$ than usually observed ($\Theta_1 = (18 \pm 3)°$). The fits from which the values for Θ_1 and Θ_2 have been taken are indicated by dashed lines. **b)** Selected area used for the diffraction patterns given in c. Label D marks a pinning center defect. **c)** Three from an energy stack of nine LEED patterns which have been evaluated for figure a. The corresponding LEED spots are indicated by arrows. The distances in reciprocal space have been calibrated using the well-known PTCDA/Ag(111) superstructure.

The dark field images have been taken after characterization with local LEED and identification of specular facet spots in the patterns (marked by arrows in column c) of figure 4.21). A field-of-view of 2 μm was chosen in all experiments, and electrons of a kinetic energy of 2.0 eV were used for the imaging. The data was recorded after the adsorption of a complete monolayer at the respective growth temperature. To reduce beam damage, the substrate temperature was lowered after the actual adsorption. Therefore, the temperatures given in this section refer to the growth temperature and not to the substrate temperature during the actual data taking, which was approximately 150 K lower in most cases.

In figure 4.21 five dark field images of high-index facets are given in column a), which have been grown at different temperatures. To achieve the best comparison, similar areas without larger defects have been chosen. Furthermore, the analysis is concentrated on one type of facet for each temperature. For this purpose, the (532) facet has been selected, observed as a predominant facet between 478 K and 573 K. In the experiments, however, this facet type has not been detected for 418 K and 612 K. In these cases, the only predominant facet type on the investigated spots has been chosen for the further analysis.

The dark areas in the LEEM images of figure 4.21a are usually populated by domains of different facet types (478 - 573 K). For 418 K, the contrast indicates that the surface is not completely planar. The data has been taken in a region of a mesoscopic protrusion similar to the one labeled "W" in figure 4.18. Darker areas on the right half of this image are presumably slightly deeper than the brighter area on the left half. Since electron of the darker areas are emitted under a slightly different angle, they do not exactly follow the optical path within the instrument through the aperture in the diffraction plane and are therefore blocked. Finally, the darker area of the 612 K image has been investigated, too. Large facets have not been found there, only dendritic clusters of PTCDA domains.

A major observation can be stated without a more sophisticated analysis. Step bunching and faceting occur in the whole investigated range of temperature. Nevertheless, the degree of long-range order varies. At 418 K, stripes of facets are observed, a periodicity is hard to recognize. In between 478 K and 573 K nice stripe patterns on the scale of the field-of-view can be observed. The situation changes, however, when the growth temperature reaches its maximum of 612 K. The facets appear more blurry, the long-range order is less pronounced.

It should be noted that the last temperature is close to (i.e. approximately 40 K below) the fragmentation temperature of the molecule on Ag(111). Moreover, increased beam damage has been observed in this case. Therefore, the partial disorder can be the result of both temperature-induced and beam-induced fragmentation of the molecules.
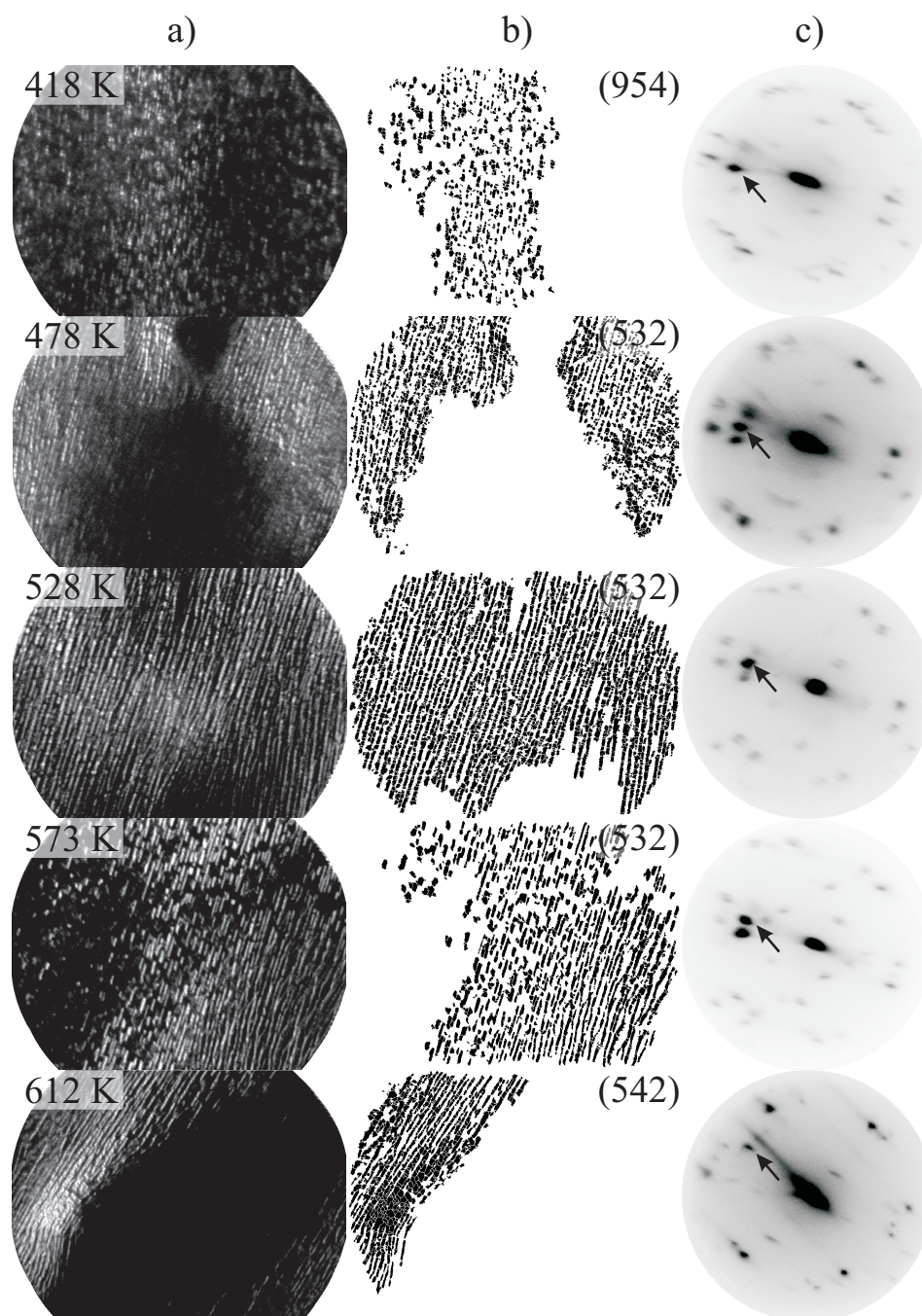
Figure 4.21.: **Facet-sensitive imaging and data processing. a)** Specific facets are imaged in dark field LEEM mode at five different temperatures (FoV: 2 μm, E_{kin} = 2.0 eV). If observed, (532) facets have been selected (418 K - 573 K). Dark areas are either populated by different facet types (for 418 K - 573 K), or not faceted at all (612 K). **b)** The images have been processed by an image recognition algorithm to measure the dimensions of the facets (labeled "b", compare figures 4.23 and 4.25). **c)** Corresponding LEED patterns (E_{kin} = 2.0 eV); arrows point to the imaged specular diffraction spots.

Automated size analysis

The data can be analyzed further on a more quantitative level. For that purpose, the dark field images were investigated with the help of the image analysis software "Gwyddion" [196]. In order to minimize human bias, facets were identified and marked by an implemented "watershed" algorithm [197]. Furthermore, a minimum size of the detected facet of 50 pixels^2 (corresponding to 74 nm^2) was required. This automated threshold was necessary to avoid noise to be counted as a facet by the program. But since this threshold does not distinguish between noise and possible small morphologic objects, it also defines the minimum size of facets to be included in the further analysis. Finally, the result has been checked by eye and corrected manually for remaining systematic errors, e.g.,like facets which are cut by the imaging horizon. The identified facets are depicted next to the original data in figure 4.21 (column b)).

Integral nucleation density N$_x$

In a system driven by diffusion the density of stable islands N$_x$ as a function of temperature should follow an Arrhenius-like behavior (compare equation (4.7)). The nucleation density is extracted from the data simply by dividing the number of identified facets by the investigated area.

The derived densities N$_x$ for the five different temperatures are given in figure 4.22 in an Arrhenius plot. The data points do not show a significant dependence on temperature. Nevertheless, they have been fitted to a simplification of equation (4.7) of the form

$$N \sim exp\left(-\frac{E_{eff}}{k_B T}\right),\tag{4.10}$$

which is indicated as dashed line in figure 4.22. An "effective activation energy" E_{eff} of (6 ± 13) meV is deduced from this fit. This at first glance strange result reflects the missing temperature dependence as already seen by eye. Marchetto and coworkers [44] have obtained a similar result for PTCDA nucleating on Ag(111) in areas of high pristine step density. Following their interpretation, it can be concluded that diffusion does not seem to determine the nucleation density in this case. Hence, adsorbing molecules attach to islands without being limited by the diffusion length.

But multiple particles (molecules and silver atoms) are necessary for a facet to nucleate and grow. Their complete kinetics is supposed to be comprehended in E_{eff}. Therefore, the simple physical model behind equation (4.10) might not appropriately cover the complex processes of facet formation.
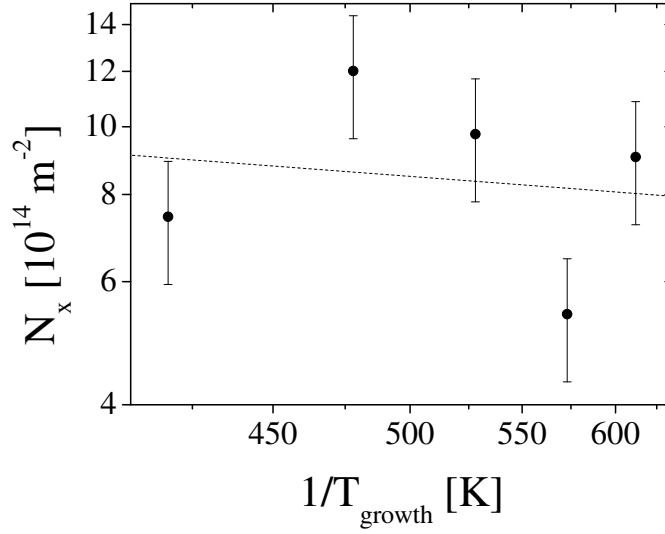
Figure 4.22.: **Temperature dependence of the nucleation density.** The number density N_x of all stable facets is plotted over temperature in an Arrhenius plot. The dashed line indicates the fit result assuming a thermally activated diffusion model.

Facet size distribution

More hints on the nucleation dynamics can be found when looking closer at the distribution of facet sizes, which is given in figure 4.23. The identified facets depicted in figure 4.21 were automatically measured and frequency histograms deduced for this comparison. Furthermore, the data were normalized such that the area of each histogram amounts to 1.

Due to the threshold, the frequency of the smallest facet sizes is truncated. Beyond this artificial range, however, the frequency of facets decreases with size, i.e. the distributions are not peaked but decrease monotonously. Moreover, the frequency histograms show a systematic dependence on temperature. In particular, the respective distributions broaden because more and more facets shift into the high-value tail. In addition, the corresponding mean values depicted in the inset show a negligible temperature-dependence similar to the one observed for the integral nucleation density N_x (compare figure 4.22).

As mentioned in chapter 4.2.3, the analysis of size distributions can be taken further. For this purpose, the size distributions given in figure 4.23 are scaled to test whether the scaling law (4.9) is obeyed in the system. A prerequisite thereof is a correct identification of the corresponding quantities in the experimental data. The scaled size S of facets is easily obtained by normalizing the facet area A to its mean value (denoted s_{av} in the following). The scaled number density N_S can be constructed by counting the frequency in the scaled interval ΔS and by consequent
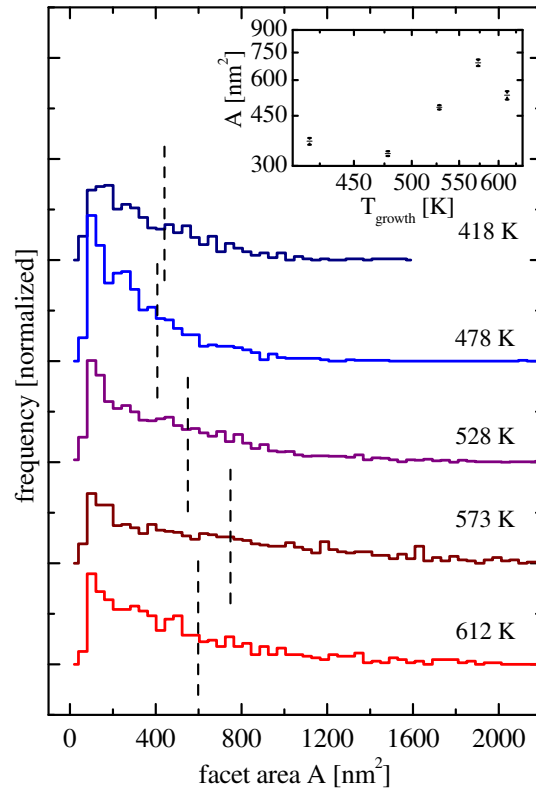
Figure 4.23.: **Temperature-dependence of the facet size distribution.** The size distributions have been derived from the data set given in figure 4.21. The respective mean values are indicated by dashed lines and in addition compiled in an Arrhenius plot in the insets, based on the hypothesis of a diffusion-based physical background. Objects smaller than 74 nm^2 have been neglected.
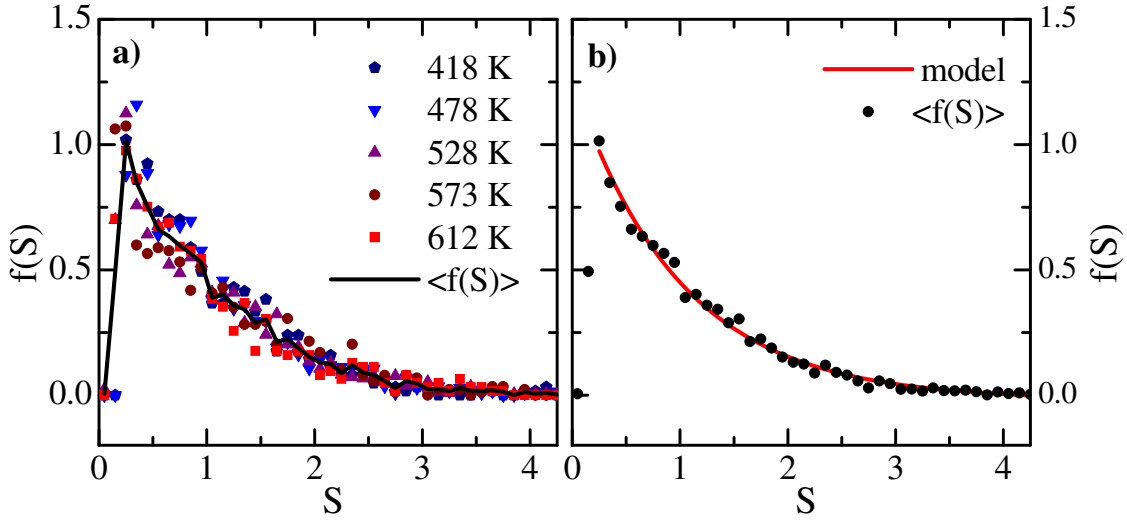
Figure 4.24.: **Collapse of the scaled size distributions** N_S. **a)** The size distributions given in figure 4.23 coincide when scaled into the common island size distribution function f_i. The scaled size distributions were averaged to deduce $\langle f(S) \rangle$ as experimental approximation to f_i. **b)** Assuming an exponential distribution (red line), $\langle f(S) \rangle$ can be fitted with high accuracy.

normalization thereon [192]. To finally shape the universal island size distribution function $f_i(S)$ out of the statistical distribution, N_S must be scaled with Θ_x / s_{av}^2 (compare chapter 4.2.3). Θ_x can be identified with the summed absolute coverage associated with the respective facets in the regime of interest [191].

The resulting data is comprised in figure 4.24. Indeed, all five scaled size distributions coincide into a single function. It can be approximated by the average of the five curves and is depicted as black line in figure 4.24.

In previous studies, pronounced maxima have been observed in the deduced island size distribution functions f_i [189, 191, 192]. The shape of this function has been used to deduce critical nucleation sizes based on comparison with simulations. The measured $\langle f(S) \rangle$, however, does not fit to the fingerprints published. It could be possible that these shapes could be reproduced if smaller facets were neither neglected by the analysis nor resolved in the experiment. Furthermore, the analysis is not performed in the low-coverage regime of the system. If coarsening of facets occurs, the system is no longer correctly described by the models. Nevertheless, an agreement should not even be expected because the scenarios on which the respective simulations are based do not comprehend the complete physics of faceting.

Beyond comparison to fingerprints, the following observation can be made: The resulting curve $\langle f(S) \rangle$ can be fitted excellently by an exponential distribution of

the form

$$\langle f(S) \rangle = A \cdot exp(-S) + B, \tag{4.11}$$

with A and B as the only free (physically meaningless) parameters. The frequency of facet sizes is hence determined by an exponential distribution. Such an island size distribution implies a random growth mode. In other words, the distribution function suggests that individual facets do not interact with each other (see, e.g., analogous reasoning in [46, 47, 49]).

Concluding the result of the last two paragraphs, the size distribution of the facets indeed obeys the scaling law originally deduced for atomic nucleation. Keeping in mind a remaining uncertainty due to the limited resolution, the shape of the island size distribution can be interpreted such that individual facets do not interact in the nucleation process. Given the previous results in this chapter, however, such a conclusion appears surprising and completely contradictory.

Anisotropy

This conclusion gets qualified, however, by inspecting not only the size distribution, but also the distributions of the extremal extensions of the facets. Therefore, minimal and maximal sizes of the identified objects (see figure 4.21b) have been measured. The maximum extension determined by the algorithm is assigned to the length l of the facet, while the minimum extension is ascribed to the facet width w. The latter assignment, however, can be problematic, especially if the algorithm renders objects imperfectly, e.g. highly fractal. Therefore, these shapes have been removed by hand. The identified objects which have been evaluated for the analysis are relatively homogeneous, as can be checked in figure 4.21b.

The corresponding histograms are given in figure 4.25. The length distributions (figure 4.25b) reflect the trends of the size distributions. They decay with growing dimension, which indicates an underlying exponential distribution similar to the one observed for the facet sizes. Furthermore, they also mimic the temperature-dependence of the facet sizes, both, in shape of the distributions, and in their mean values. Therefore, the conclusion that the growth process is not limited by diffusion is corroborated again.

The width distributions, however, are completely different in shape (compare figure 4.25a). The mean values are almost constant within the statistics. Only a small step-like rise between 478 K and 528 K could perhaps be deduced from the data. Most importantly, however, a peak can be observed around the corresponding mean values. Furthermore, no significant temperature-dependence can be identified in the distributions.

Therefore, the distributions reflect the anisotropic growth which one can of course already identify by eye in the real space images. In particular, they indicate that the exponential distribution only governs the length of the facets. The peaked
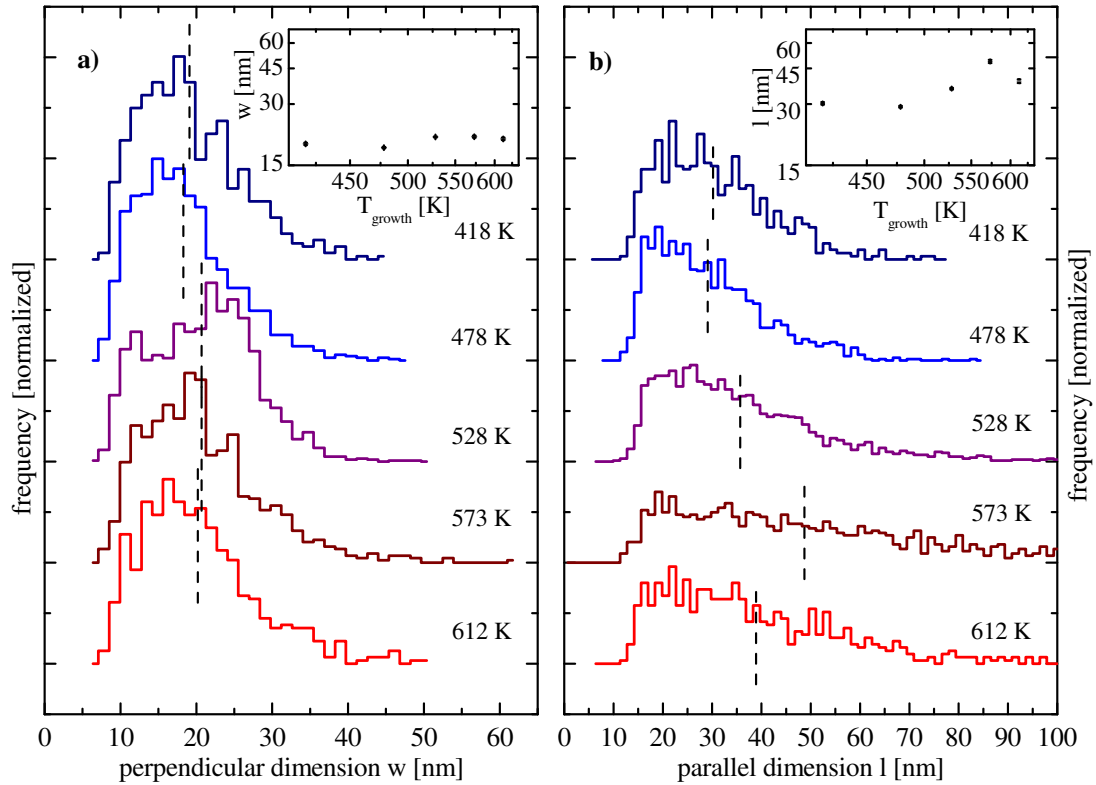
Figure 4.25.: **Temperature-dependence of facet width and length distributions.** Minimal (a) and maximal (b) extensions of the objects identified in figure 4.21b have been automatically measured and interpreted as width w and length l of the facets. The respective mean values are indicated by dashed lines in the histograms. Their temperature dependence is given as Arrhenius plots in the insets to look for a possible diffusion-based formation mechanism.
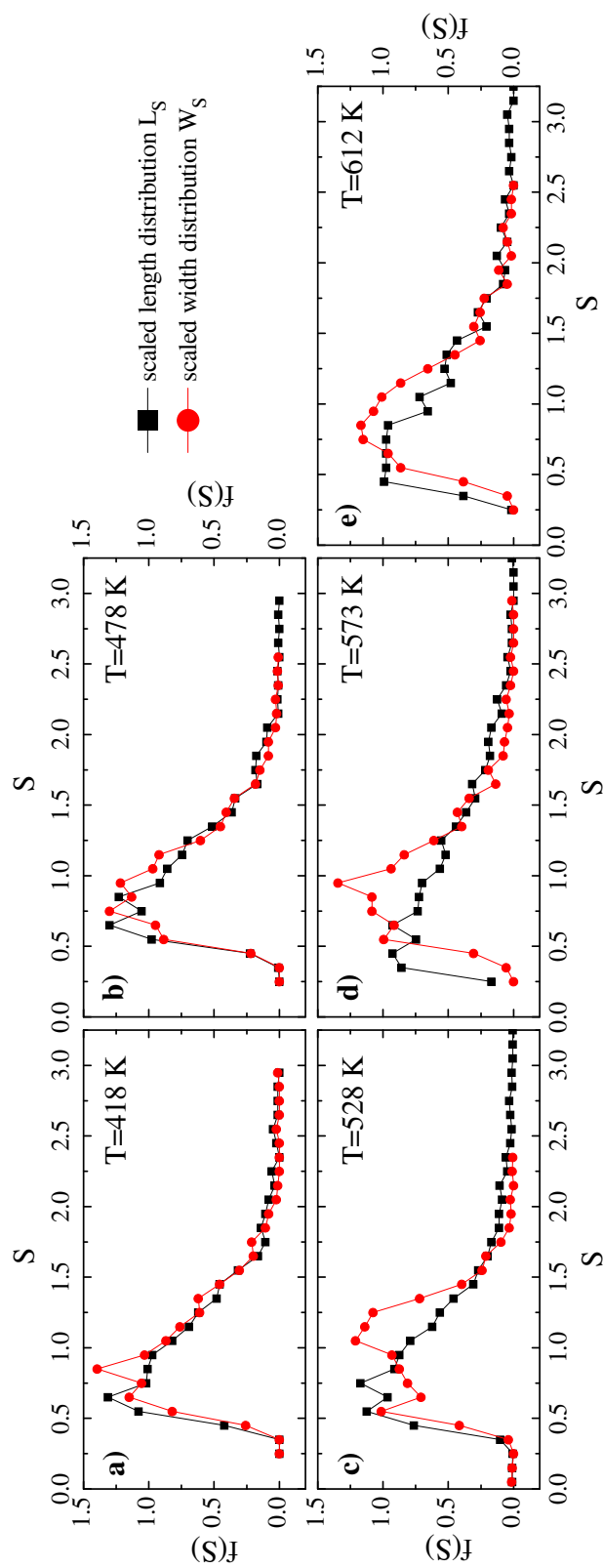
Figure 4.26.: **Anisotropy of scaled distributions.** Width and length distribution densities W_S and L_S have been scaled following the approach for size distributions. At lower temperatures (**a** and **b**) they are identical. Above 500 K, however, the isotropy is lifted.

width distributions indicate that the growth in this direction is not random but determined by mutual interactions [47].

Besides, one should be aware of the fact that the measurements of length based on the watershed algorithm are not perfect. The algorithm basically renders levels of intensity. If the contour of a structure is of considerably lower intensity than its center, it is incompletely identified. Although this has been carefully checked, it cannot be completely avoided. A general shift in the order of 2 nm to smaller dimensions can hence be expected. While this error is hard to be identified in size and length, it can be recognized in the width distribution: In the corresponding histograms (compare figure 4.25a) dimensions smaller than 10 nm appear, which is below the resolution limit of the current measurements.

Finally, the scaling analysis was extended to the width and length distributions. Therefore, the histograms given in figures 4.25 were scaled in the same way as the size distribution. Although such a scaling of dimension densities is lacking theoretical backing, the result appears promising. Therefore, it appears justified to be reported.

The scaled widths and lengths distribution functions W_S and L_S are compared for the different temperatures in figure 4.26. Two regimes can be identified. For the growth temperatures below 500 K, i.e. in figures 4.26a and b, the scaled distributions W_S and L_S are identical within the limits of resolution. Above this temperature, however, the scaled width distributions are more strongly peaked and more symmetric with respect to the mean values than before, and the two distributions do not coincide anymore.

Therefore, the result shows that the isotropy of the physics behind the growth of the facets in length and width is broken for higher temperatures.

4.7. Discussion

At this point of the chapter, I have finished the survey on the experimental results on the PTCDA/Ag(10 8 7) interface. In this section, I want to discuss them from a more topical point of view, trying to embrace the input of the different experimental approaches. First, new insights into the morphology of the system will be gathered, then the magnitudes of the surface stress change of the different PTCDA/Ag(111) interfaces pondered against each other, and finally, as a kind of synthesis, the intimate relation between surface stress change and morphology transitions revealed.

4.7.1. Morphologic aspects

In general, this characterization of the surface morphology is in good agreement with the observations by Schmitt [159]. For example, only one new facet type has

to be introduced to describe all the morphologic objects observed in the present experiments. Moreover, this (953) facet is only found in the vicinity of a defect.

Nevertheless, the techniques applied for the first time to characterize this interface have offered new insights into the morphology which in part add information and refine the understanding of Schmitt's results.

Sequence of nucleation

The in-situ experiments show that the formation of the first monolayer of PTCDA on Ag(10 8 7) follows a strict hierarchy not only when partial coverages are annealed, but also under a continuous supply of molecules. First, molecules nucleate in regions with high pristine step densities. The molecules immediately bunch steps and also, depending on temperature, micro-facets are formed. Subsequently, the step bunching is completed over the whole surface, starting in the vicinity of the first nucleation centers. The (111) faces are covered only as final step. The well-known preferred interaction of PTCDA with step edges on Ag(111) (see chapter 3.3) is hence demonstrated again under the extreme ambient condition of high temperature and continuous flux of molecules.

Occurrence of steeper facets

The fact that steeper facets have only been observed for the lowest substrate temperature of 418 K in the present experiments is more surprising. This could be explained by the special preparation path. At higher substrate temperatures and sufficient supply of molecules, it is apparently not necessary, or possible, to bunch three steps under a single molecular row. This mechanism had been described for the formation of steeper facets of an inclination angle of 27° with respect to the (111) terraces [159].

It is not be possible to finally decide from the present data whether kinetics suppresses the formation of steeper facets under the preparation conditions used, or whether the flatter configuration is energetically more favorable. The fact, however, that steep facets have not been observed in the low coverage regime with SPA-LEED (see chapter 4.5.1) favors the latter interpretation. At least, diffraction spots are still split in this coverage regime, which indicates that a significant number of steps is still available. A growth of more planar facets as compromise for lacking step atoms can therefore be excluded. On the contrary, their observation at lower growth temperatures indicates the mobility of the surface atoms to play a role. Therefore, the steeper facets rather seem to be a compromise.

Nevertheless, the role of the local morphology, considering a growth of steeper facets only in the direct vicinity to pristine defects, cannot be ruled out based on the observations.

Importance of the pristine mesoscopic orientation

In general, the intermediate resolution regime accessible for the first time with the LEEM experiment has demonstrated the important role the mesoscopic surface morphology plays. In the previous paragraphs, it has already been mentioned that areas of local high pristine step density are always observed to be nucleation centers for the faceting process. As argued in the previous paragraphs, similar defects might also promote the formation of steeper facets.

In addition, it should be emphasized that the observations demonstrate the contours of mesoscopic defects not to be altered by the faceting process. On the contrary, special facets are formed which adapt the contours of the defects. As seen in chapter 4.6.2, this can lead to a large local variety of different facets. In part, this finding could explain the large number of facets described before for this system, especially because some of them have exclusively been observed by STM measurements [159].

In total, the results establish a hierarchy of morphological objects: Steps get rearranged to form facets of special orientations. But the facets themselves depend on the mesoscopic morphology already present on the clean substrate. In other words, these observations define the dimensional limits of the restructuring of the surface in the faceting process. It is not the overall average surface orientation which defines the process of faceting, but the mesoscopic shape of the morphology.

Finally, the last statement should be extenuated to some degree. The average orientation of the substrate, however, obviously defines the average facet orientation and population for the same reasons as given in the previous paragraph. Therefore, averaged physical properties like the surface stress change can be well explained by averaging measurements of the structure (see chapter 4.7.3).

The role of the growth temperature

Looking at the Arrhenius plots of the temperature-dependence of integral nucleation densities and of the average facet dimensions given in figures 4.22, 4.23, and 4.25, one could come to the conclusion that the growth of the system is completely independent of the temperature for the range investigated. Nevertheless, such an absolute conclusion could be premature for the complex system PTCDA/Ag(10 8 7). The basis therefore would be an in part heuristic theory of nucleation developed for single-atomic adsorption on substrates which do not alter in the process.

In fact, there is some evidence in the presented results that a complete structural transition requires elevated temperatures above 500 K under the growth conditions applied. At 338 K, e.g., which is the lowest growth temperature investigated in this study, the surface stress changes in a completely different manner than in the high temperature regime. As seen in chapter 4.4.1, this can be correlated to a LEED pattern missing distinct facet specular spots.

More convincing that kinetics play a significant role in the formation of the structure is the discovery that the size distributions obey a scaling law derived for nucleation governed by diffusion. I believe that these distributions with their characteristic shape could be a suitable property of the system to compare prospective modeling efforts with experiment. At least, the adherence to the scaling law implies that a mean-field approach could be actually powerful enough to incorporate more complex systems.

Finally, there are indications of two distinct growth regimes in the width distributions: One below, and one above (500 ± 20) K. Above this "critical temperature" the width distribution is completely governed by thermodynamics, and kinetics are negligible thereon. It should be realized that it is indeed this width distribution which determines the quality of the structural order of a self-organized grating.

4.7.2. Stress change at the PTCDA/Ag(10 8 7) interface

In the following section, the stress change upon the formation of the PTCDA/Ag(10 8 7) interfaces will be discussed further. In the beginning, the stress change at the different PTCDA/Ag(111) interfaces investigated in this work will be compared. Subsequently, the magnitude of the elastic interaction will be confronted to an estimate of the competing electrostatic interaction to learn more on the driving force of the large-scale phase transition.

Comparison of the stress change at PTCDA/Ag(111) interfaces

As seen in chapter 4.4, different absolute stress changes are observed upon formation of the "disordered" and the "long-range-ordered" phases of the PTCDA/Ag(10 8 7) interface.

As argued in chapter 4.4.1, the first "disordered" phase is characterized by local step bunches and (111)-terraces covered by the PTCDA/Ag(111) superstructure. The phase is probably not a thermodynamically favored state but a consequence of kinetic hinderance of the formation of the long-range ordered state. Therefore, it could be argued not to be a well-defined but a strongly temperature-dependent state. But from a structural point of view, this "transition state" can be seen as an intermediate state between the PTCDA/Ag(111) interface and the long-range ordered PTCDA/Ag(10 8 7) interface. This interpretation is also supported by the surface stress change upon its formation.

The overall stress change of (-0.39 ± 0.10) N/m or (24 ± 6) meV/Å^2 is 30% larger than the one measured for the PTCDA/Ag(111) interface (see chapter 3.4). This comparison fits to the interpretation that surface stress is released both, upon superstructure formation, and, in addition, upon step bunching in the system. Nevertheless, the magnitude is still approximately 40% smaller than the one observed

upon formation of the long-range ordered system. The formation of large domains of bunched steps hence obviously decreases the intrinsic stress further.

Moreover, the functional dependance of the stress change curve in the disordered case shows features of both interfaces, too. In the low coverage regime (until point B in figure 4.5c), $\Delta\tau$ remains basically unchanged by the adsorption, similar to the behavior when the experiment is performed at higher temperature (compare phase A to B in figure 4.6a). In its following monotonous decrease, however, the functional dependence of $\Delta\tau$ resembles more to the one observed at the PTCDA/Ag(111) interface.

As mentioned before, the overall stress change in the case of the long-range order formation is with (-0.67 ± 0.10) N/m (corresponding to (0.30 ± 0.05) eV per silver atom) the largest stress change observed for the investigated PTCDA/Ag(10 8 7) interfaces.

At least two mechanisms can be identified for this well-defined state of the system which contribute to the measured compressive net change of surface stress. Firstly, the local charge transfer from the silver substrate into the adsorbate reduces the intrinsic tensile surface of the first atomic substrate layers in compliance to the physics identified at the PTCDA/Ag(111) interface in chapter 3. Secondly, on the mesoscopic level, the mono-atomic steps, which are originally distributed equidistantly, are bunched together in the faceting process. Thereby, they overcome the mutual repulsive step interaction, which also introduces compressive stress into the system.

The stress changes measured for the vicinal interfaces are even slightly larger than for the PTCDA/Ag(111) interface formation. Therefore, the values strongly support the conclusion in chapter 3.5.1, that the organic molecules cause a considerable stress even though the bonding is weaker than in most inorganic systems.

The decisive question is, of course, *whether the measured stress change is sufficient to drive the large scale self-organization of the system*. Regarding the absolute value of the stress change, a comparison to available literature values gives a mixed answer: In the case of the N/Cu(001) checkerboard pattern the intrinsic stress change upon the pattern formation is in fact ten times larger than in the present case [182, 186]. But the observed magnitude of the net stress change differs only within a factor of 2 from the one measured in the Cu-CuO-stripe system [61, 187]. Therefore, the strength of the elastic interaction appears to be large enough to explain the long-range order from the point of view of magnitude.

Elastic vs. electrostatic interaction

Nevertheless, the physics of the system might not be completely described by a purely elastic picture. The influence of the electrostatic interaction (4.3) should at least be estimated. The relatively small magnitude of $\Delta\tau$ in the system makes it necessary to think about the ratio r of elastic (4.4) and electrostatic (4.3) energy

again.

Neither experimental nor theoretical values for work functions of faces with high step density are presently available in literature for high-index silver surfaces, or even PTCDA-covered high index silver surfaces. At least, the work function difference $\Delta\Phi$ between the (111) surface and polycrystalline silver is known to amount to (0.46 ± 0.30) eV [24]. Together with the measured $\Delta\tau$ of 0.7 N/m, r can be evaluated to be

$$r = \frac{\gamma_{interaction}^{elastic}}{\gamma_{interaction}^{electrostatic}} = \frac{4(1 - \nu_{Ag(111)}^2)}{Y_{Ag(111)}\varepsilon_0} \left(\frac{\Delta\tau}{\Delta\Phi}\right)^2 \sim 10, \qquad (4.12)$$

with $\nu_{Ag(111)} = 0.513$, $Y_{Ag(111)} = 82.82$ GPa, and $\varepsilon_0 = 8.85 \times 10^{-12} \frac{C}{Vm}$.

Hence, according to this estimate, the elastic interaction can be expected to be one order of magnitude larger than the electrostatic interaction. Furthermore, the electrostatic contribution can be expected to be even smaller because the crystal faces are covered by PTCDA in the actual experiment. In fact, Zou has measured the work function difference between Ag(111) and Ag(110) to shrink from 0.3 eV to 0.1 eV when the faces are covered by a PTCDA monolayer [155]. Due to the quadratic dependence on $\Delta\Phi$, an analogous reduction in work function difference between PTCDA-covered (111) and true high-index faces would drastically reduce the importance of the electrostatic interaction further.

Nevertheless, it would be desirable to actually measure the work functions of the different facet faces directly. Such a local work function measurement could be performed by Kelvin-Probe Microscopy or by Spectro-Microscopy in photoemission electron microscopy (PEEM) mode.

4.7.3. Surface stress change and morphologic evolution

A discussion limited to the magnitude of the surface stress change cannot determine the role of surface stress in the system unambiguously. Further evidence, however, can be collected by correlating the stress change to the morphologic evolution.

Surface stress vs. morphology

For this purpose, in figure 4.27 the facet intensities derived from the SPA-LEED data (top panel) are compared to the surface stress curve (lower panel). In order to ease the comparison of the data sets previously presented in figures 4.14 and 4.6, they are not plotted against "experimental time" but the physically more meaningful quantities "coverage" and the "time annealed". To complete the understanding of the structural transitions, the microscopic information gathered by LEEM depicted in figure 4.17 is included in the discussion.
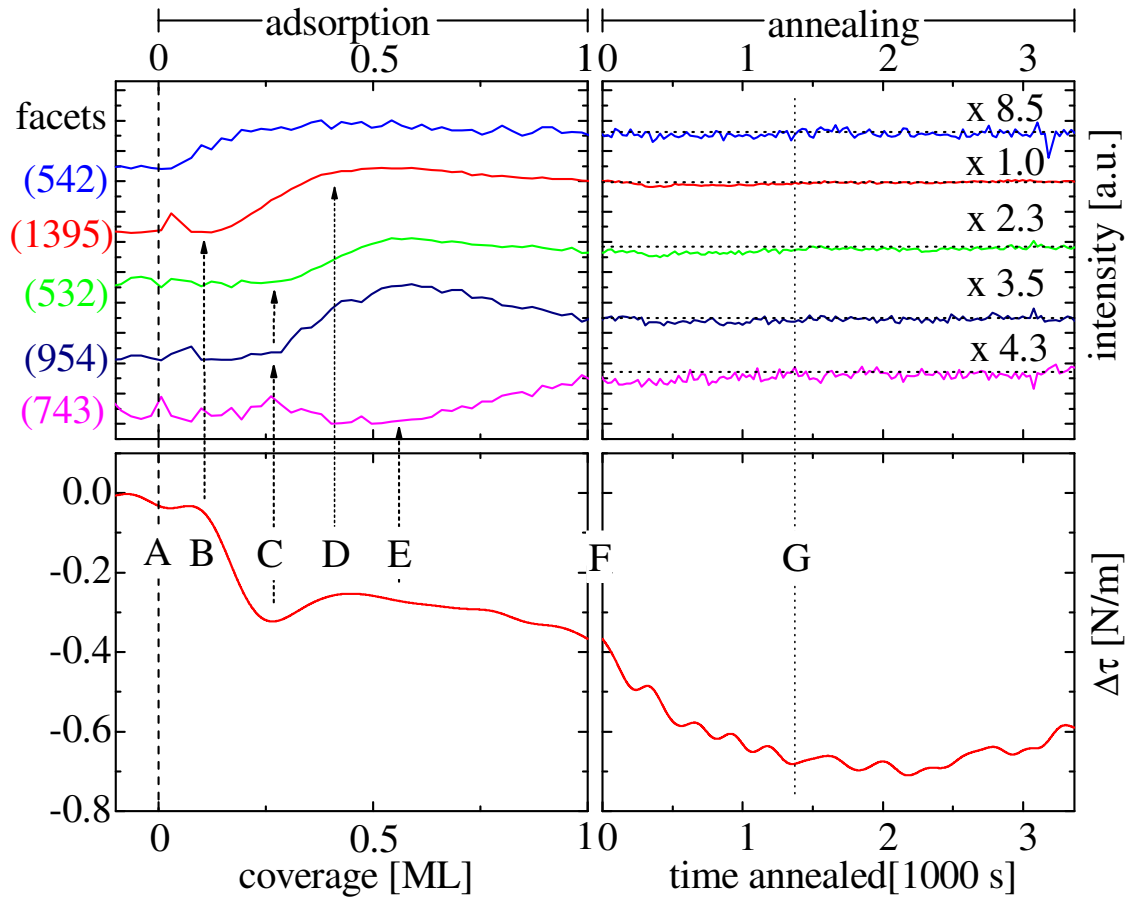
Figure 4.27.: **Correlation of structural evolution and change in surface stress.** The facet intensities (top panel) are derived from SPA-LEED line scans (compare chapter 4.5.2), the stress change curve was taken from figure 4.6. The data is plotted against coverage during the adsorption phase (left column) and against time during the annealing phase of the respective experiments (right column). Vertical dotted lines and arrows indicate the correlation between characteristic changes of the surface stress and the facet formation. The asymptotic facet intensities after prolonged annealing are indicated by dotted horizontal lines.

The comparison demonstrates that every change in curvature of the stress change curve coincides with the onset of a new facet peak during adsorption.

As mentioned before, $\Delta\tau$ does not alter in the initial stage of the experiment. The diffraction data, however, reveals that the (542) facets are already formed at very low coverage. Nevertheless, they do not seem to affect the surface stress within the limits of resolution. One reason thereof could be their relative rareness.

Another reason for the apparently constant surface stress can be found in the microscopic data. It reveals that the nucleation occurs exclusively in defect areas in this early stage. Since the orientation of the facets is dominated by the underlying local morphology of the substrate (see discussion in chapter 4.7.1), the facets which are formed in this stage can have a large variety of orientations. In average, the respective stress contributions would vanish. At least, it should not be expected that large mesoscopic strain fields would built up under these conditions.

The formation of the predominant (13 9 5) facets, however, significantly lowers the intrinsic stress. Stated otherwise, the surface is driven into a configuration from which it tends to expand. The next two facet types, (532) and (954), grow simultaneously. In superposition, the stress contributions of the latter three facets turn the stress change into the tensile direction, counteracting the previous compressive tendency.

At a coverage of 0.4 ML to 0.6 ML, the surface stress alters only slightly. In this coverage regime, nominally all steps are decorated with PTCDA molecules [11]. Both SPA-LEED and LEEM data show the surface to be faceted completely in this coverage regime. Freshly adsorbed PTCDA molecules start to populate (111) terraces. They form well-ordered superstructure domains, which appear white in the LEEM data. The regime is furthermore distinguished by the fact that (13 9 5), (532) and (954) facet spots reach their maximum intensity in SPA-LEED.

The phase of stationary equilibrium in surface stress and morphology ends at a coverage of 0.6 ML. In a last restructuring of the surface, the new facet type (743) is formed at the expense of (13 9 5), (532) and (954) facets. As a consequence, their intensities decrease. This final morphology transition causes a further reduction of surface stress, which is even not finished after all material is adsorbed. In contrast, the gradient increases in the initial annealing time. Equilibrium in both stress and morphology is finally reached after approximately 20 minutes of annealing.

The correlation to the complementary techniques allows to draw conclusions on the physics of the surface stress change.

First, the fact that both, surface stress change and structural transitions reach their asymptotic values on the same time scale strengthens the confidence in the data processing. Obviously, the last drop in stress change is induced by real annealing effects on the surface and not by an artifact of the drift correction. Besides, the time scale of approximately 20 minutes is in good agreement with the experimental experience for the growth of well-ordered structures.

Moreover, the clear correlation between structure and surface stress contributes

to the understanding of the kinetics of the faceting process. Up to now, two major boundary conditions are known to govern the process: The inevitable conservation of the average macroscopic orientation, which is equivalent to demand the conservation of the overall average step direction and density, and the preferred formation of defect-free boundary lines [159]. But the perfect alternation between the occurrence of tensile and compressive facets strongly suggests that whether and when a specific facet type is formed is determined by its stress contribution. This can be explained by assuming the system trying to limit the net stress built up. A balanced net surface stress should consequently be added to the boundary conditions discussed before.

Finally, and most importantly, however, the assignment of different stress regimes to morphological objects of mesoscopic dimensions (i.e. the facets) is equivalent to the identification of stress domains on the surface. These domains lead to stress discontinuities and induce effective force monopoles at the domain boundaries [183]. As discussed in chapter 4.2.2, the existence of these force monopoles promotes the equidistant spacing of domains with critical sizes in the Marchenko-Alerhand model [14, 15]. Thus, the experimental data provide clear evidence that it is indeed surface stress which plays a decisive role in the ordering on the mesoscale.

Stress relieve upon re-faceting

In addition, the correlation between stress change and morphologic evolution contributes to the understanding of another detail of the morphologic transition at the interface. In the high coverage regime (above point E in figure 4.27), the already completely faceted surface undergoes another transition and re-facets under transformation of (13 9 5), (532) and (954) facets into (743) facets.

Schmitt has attributed this transformation to the tendency of the system to form perfect boundary lines, based on his analysis of the respective superstructures of the involved surfaces [159]. As demonstrated in figure 4.15, the (743) facets are in fact formed in complete synchrony with the PTCDA superstructure on the (111) terraces.

But according to figure 4.27, another effect might promote the restructuring, too: The re-faceting is accompanied by a significant drop of surface stress of (0.45 ± 0.05) N/m or (28 ± 3) meV/Å^2. This value can only in part be explained by the superstructure formation on the (111) terraces, considering the magnitude in comparison to the one observed at the PTCDA/Ag(111) interface. Obviously, at higher coverages the morphologic configuration which is newly formed is lower in surface free energy than the initial configuration.

A complete re-faceting is nevertheless not observed. Such a drastic re-faceting is probably hindered by kinetics, considering the morphologic state the system has already changed into at medium coverage.

4.8. Conclusion

In summary, the formation of the interface PTCDA/Ag(10 8 7) and some of its final state properties have been investigated by a comprehensive experimental approach in this chapter: Completely different techniques have been combined to gather a large variety of complementary information.

All of the techniques have provided new insight into the formation of faceted metal-organic interfaces. Surface stress change measurements have been performed for the first time for a faceting system at all. Similarly, SPA-LEED has proven capable in the experiments to achieve temporal resolution on the relevant scale with sufficiently high resolution. Finally, the LEEM measurements close a "traditional" gap between experiments averaging over the complete macroscopic interface, like LEED, and characterizations on atomic scales as in STM as they are able to collect reliable information on the mesoscopic properties.

Indeed, these investigations have revealed a strong influence of the local morphology on the specifics of the faceting process. The local orientation on scales of several hundreds of nanometers can sincerely deviate from the parameters measured for the average surface. This result should be kept in mind when exploiting this system class as "perfect" templates. Thereby, the LEEM experiments have revealed the dimensional limit of the restructuring transition. Morphologic defects on the scale of several tens of nanometers force their contour on the facets formed, and not vice versa.

Furthermore, a thorough picture has been gained of the nucleation and the formation of the faceted interface. First of all, steeper facets seem to play a less important role for the nucleation of the molecules than has been suspected based on STM results [159]. Nevertheless, a strict hierarchy of steps in the morphologic transitions has been observed in all experiments during adsorption and faceting: High-index facets are formed (and thereby covered first) by molecules, before (111) terraces are populated by stable superstructure domains. This result is in excellent agreement with previous conclusions based on characterizations of intermediate states of the system [159].

A further important property which characterizes the nucleation kinetics of a system is the dependence of its formation on temperature. In the temperature regime studied, its influence is not obvious. Nevertheless, a scaling law has been found behind the size distribution of the facets, which was originally derived for nucleation governed by atomic diffusion. These scaled distributions might be suitable for comparisons to theoretical models due to their sensitivity to the physics involved in kinetics.

Moreover, the experiments provide evidence for the existence of a critical temperature beyond which the structural width of the long-range order is solely determined by thermodynamics. This might be a consequence of the preparation path used for the present experiments. At least in this case, however, high quality in long-range

order can probably only be achieved if the substrate is kept above this temperature. Nevertheless, subsequent annealing is not negligible either. Both SPA-LEED and cantilever experiments consistently reveal a minimum time required for full annealing in the order of 20 minutes, despite the high substrate temperature during adsorption.

One particularity of the kinetics of faceting systems is the fact that specific ("magic") facets are formed. The cantilever experiments indicate that one factor in this process could be the tendency of the system to limit the net stress built up by generation of new facets. Hence, a balanced net surface stress should be included to, and ranked amongst other conditions when discussing these processes.

With regard to the cantilever method itself, the three investigated "different" metal-organic interfaces in this work can be summarized. The comparison of the results shows that $\Delta\tau$ reflects the structural evolution of these systems in its systematics. Hence, cantilever measurements of the change in surface stress have proven to be a sensitive integral probe for organic-metal interfaces, which provides confidence in possible future experiments in this field.

In particular, the cantilever measurements have successfully contributed to a secured understanding of the physics behind the faceting process at these interfaces.

Only a slight question mark on the role of electrostatic interactions for the formation of periodically faceted metal-organic interfaces remains. This question can only be answered by an experiment, measuring the corresponding differences of work functions of neighboring facets. But the estimate of the strength of the electrostatic elastic interactions shows that elastic interactions can definitely not be neglected from the point of view of magnitude. On the contrary, the magnitude of the surface stress change measured upon formation of the ordered PTCDA/Ag(10 8 7) interface appears sufficient to enforce the observed self-organized long-range ordering. Additional interactions are hence not necessary to be postulated.

Finally, the perfect correlation of morphologic transitions and regimes in surface stress provides strong evidence that surface stress is indeed the driving force behind the long-range order in this system and more importantly, also in the whole system class of organic-metal interfaces. Therefore, the results strongly support respective theoretical descriptions in literature [14, 15] based on elastic interactions. Thus, the application of these theories on faceted, long-range ordered metal-organic interfaces has gained legitimation by these experiments.

Template-assisted growth: C_{10}SH/PTCDA/Ag(10 8 7)

In the previous chapter, the basic physics behind the self-organization and the faceting process induced by PTCDA on Ag(10 8 7) has been studied intensely. This effort can be justified by the prospective use of this kind of materials as templates for the bottom-up growth of nanostructures. In this chapter, we will present such an approach for the growth of a heterorganic nanostructure based on our model interface.

5.1. Self-assembled monolayers

We have chosen alkanethiols as co-adsorbents to the patterned PTCDA/Ag(10 8 7) interface. These molecules form dense, up-right standing films on noble metal surfaces, the so-called self-assembled monolayers (SAMs). This very popular class of organic-metal interfaces consists of a large variety of "ordered molecular assemblies formed by the adsorption of an active surfactant on a solid surface" [198].

Introduction to SAMs

SAMs are formed by a highly complex balance of localized adsorbate-substrate and intermolecular interactions [198]. These processes have been studied intensely, especially for interfaces formed by alkanethiols on a Au(111) surface. These archetype

systems are relatively easy to prepare and show a high degree of order. Comprehensive reviews on preparation, underlying chemistry, and physics have been published by Ulman [198], Poirier [199], and Schreiber [200]. Beyond their success in fundamental research, alkanethiol-based SAMs have also been used for a number of applications, for example as growth templates, in electrochemistry, or as a part of "biofunctionalized" surfaces [200, 201].

In general, two different preparation paths are possible. The more common one is the preparation by immersion, i.e. ex-situ in a bath of highly-concentrated alkanethiol solution. In the course of this preparation, the noble metal substrate is usually exposed to air and thus contaminated. Nevertheless, there are strong indications that a pre-coverage with oxygen actually promotes the redox-reaction necessary to form the chemical sulphur-gold bonding (see e.g. [202]).

If better-defined ambient conditions are necessary, also chemical vapor deposition (CVD) under high vacuum is possible [200]. A STM study has shown that in this case the growth mode of SAMs of alkanethiols strongly depends on the offered amount of material [125]. Different phases can be observed, from flat-lying at low coverages to upright-standing at high coverages. Moreover, the degree of order of these phases varies with coverage, too [125, 203].

Alkanethiols/Ag(111)

Given the template PTCDA/Ag(10 8 7), the main interest is of course in the growth of alkanethiols on Ag(111) surfaces. The alkanethiol-based SAMs on this substrate are characterized by the stronger substrate-head group interaction than in the case of Au(111) [198]. Therefore, the films are denser [198], and the molecules are arranged in an incommensurate superstructures of two rotational domains (superstructure cells: $(\sqrt{3} \times \sqrt{3})R(30 \pm 18)°$) [204, 205]. Moreover, some experimental results even indicate an island-growth mode for the interface formation [202].

In the denser structure, the molecules are standing more upright than observed on Au(111). Tilting angles Θ_t of only 10-12° (compare figure 5.1) have been measured for films prepared by immersion [202, 206], and of 17° for CVD-grown films [207]. Finally, one can observe the order to decrease from the level of the actual metal-organic interface to the surface of the SAM by comparing He-diffraction with x-ray-diffraction data [204].

Coadsorption of PTCDA and SAMs in literature

Since both PTCDA and alkanethiols are archetype molecules in surface science, it is not surprising that there have been investigations of their coadsorption before. PTCDA has been exposed to both of the well-ordered phases of decanethiol (CH_3-$(CH_2)_9$-SH; short $C_{10}SH$) on Au(111): the flat-lying stripe phase and the upright-standing c(4×2) phase [125].
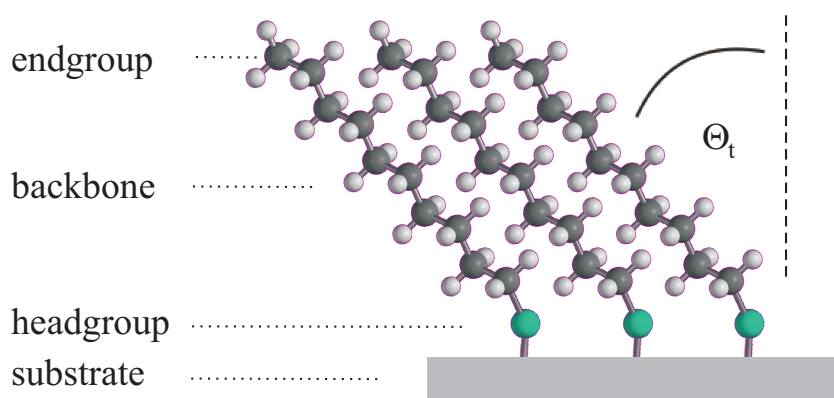
Figure 5.1.: **Schematic of a SAM.** Decanethiol molecules form a chemical bond between the sulphur atoms and the substrate. Their average orientation versus the surface normal is described by the tilt angle Θ_t. In addition, the conventional labels of the different functional units of a SAM are given [200].

In the former case, PTCDA molecules which are adsorbed on top induce a transition into complete disorder [208]: The alkanethiol stripe phases rearrange and get in part covered by PTCDA molecules. Moreover, PTCDA molecules can be observed which even replace the alkanethiols. Thereby, they can directly bond to the Au(111) surface and form the well-known herringbone superstructure [208].

In the latter case, however, an almost perfect sandwich layer can be prepared, which can act as a "molecular x-ray interferometer" [200, 209]. In fact, this configuration has been used to precisely determine the thickness of the SAM-layer [200, 209]. Nevertheless, the physical properties of the SAM seem to feel the influence by the covering PTCDA layers: The supposedly weak interaction has been argued to be responsible for a slight shift of the melting-temperature between covered and free-standing SAM configurations [210].

5.2. Chemical vapor deposition of decanethiol on Ag(111)

Since we are interested in adsorbing SAMs onto the pre-patterned PTCDA/Ag(10 8 7) interface, chemical vapor deposition has been chosen as growth mode for the SAMs. Thereby, the sample can be prepared completely in-situ, which prevents the template from contamination. Nevertheless, as indicated in the previous chapter, this preparation path raises the question of the quality of the films prepared. Therefore, the "pure" decanethiol films grown on clean Ag(111) are characterized before turning to the more complicated system.

Preparation conditions

The decanethiol molecules are fluid at room temperature. Therefore, the molecular vapor was entered into the chamber by a leak valve. It was guided directly onto the sample by a round nozzle of stainless steel of a diameter of 5 mm. The exit of the nozzle was positioned approximately 1 cm above the substrate.

The substrate was kept at 300 K throughout the preparation. It was exposed to a thiol partial pressure in the order of $1.5 \cdot 10^{-7}$ mbar for typically 15 minutes, measured by an ion gauge positioned approximately 40 cm away from the nozzle exit. Hence, a dose in the order of 100 - 300 Langmuirs (L) (1 L = $1.33 \cdot 10^{-6}$ mbar) was offered. Given the experimental geometry, however, this value should be considered to be an estimate of the lower limit.

Thermal desorption spectroscopy

The films have been investigated by thermal desorption spectroscopy (TDS) [25]. Therefore, they were heated underneath a quadrupole mass spectrometer with a heating rate β of 1 K/s. This magnitude of β has proven suitable for organic molecules before (see e.g. [203, 211]).

The signal intensity of the most prominent fragment of mass-to-charge ratio m/e=43 is given in figure 5.2. It can be assigned to the alkyl-radical $H_3C\text{-}(CH_2)_3\cdot$. Complete molecules (m/e=174) were not detected.

Two states A and B can be clearly distinguished in the TD spectrum. The "low-temperature peak" A occurs at 390 K, and the "high-temperature peak" B at 490 K. Since absolute temperature measurements are not very reliable for silver crystals, a large error bar of ± 30 K for the absolute temperatures given on the scale should be assumed [151].

The major result of two states fits to observations by Kondoh et al. [203] for SAMs formed by hexanethiol (C_6SH) on Au(111). They were able to assign the low-temperature peak to molecules desorbing from an upright-standing phase, while the high-temperature signal could be ascribed to the remaining molecules desorbing from a flat-lying stripe phase.

Therefore, the thermal desorption spectrum can be interpreted that at least domains of upright-standing molecules have been successfully prepared. Conclusions on the degree of order or the ratio of flat-lying to upright-standing molecules, however, are not possible from this data.

Attenuation of photoelectrons

Additional information on the orientation of the molecules can be derived from the attenuation of photoelectrons emitted by sulphur atoms. Assuming the molecules to stand up-right (compare figure 5.1), these electrons must pass a layer of hydrocarbons, in which a part of them are inelastically scattered before reaching vacuum
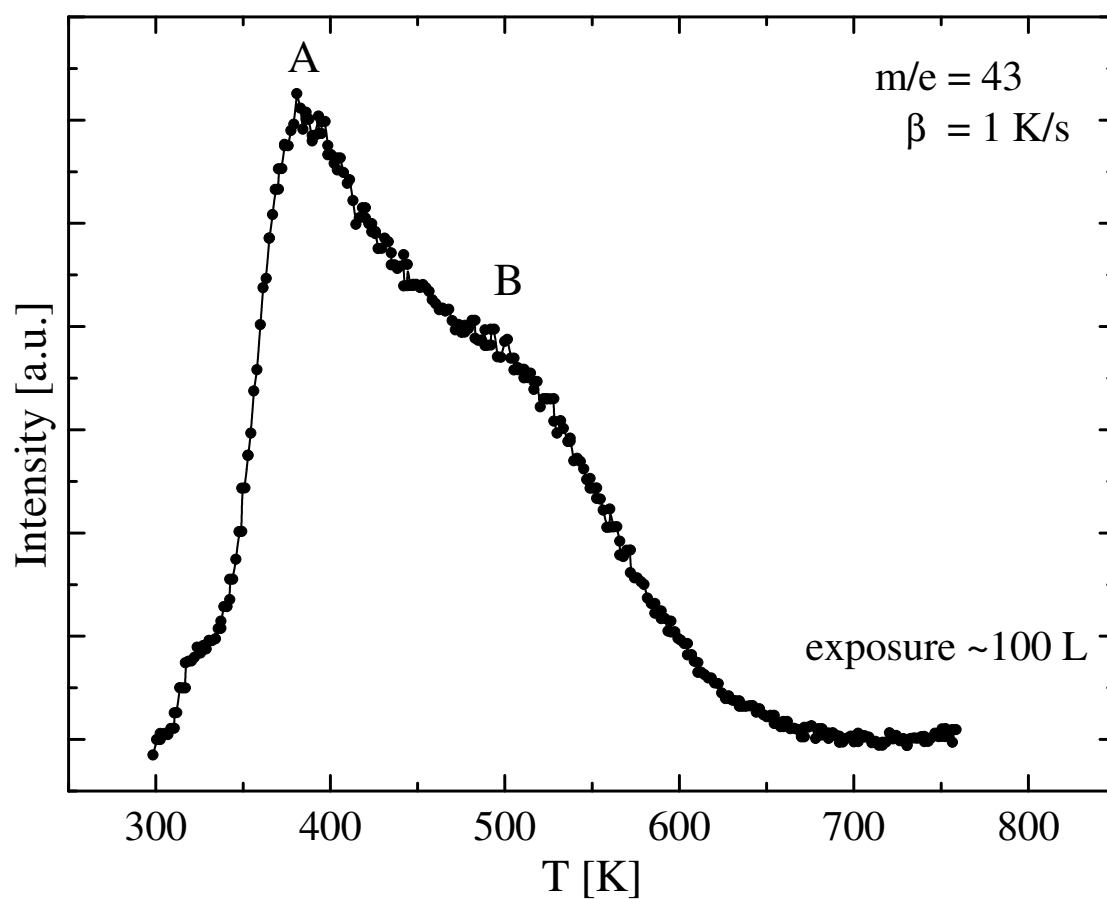
Figure 5.2.: **Thermal desorption spectrum from a CVD-grown SAM on Ag(111).** The desorption of a prominent fragment with a mass-to-charge ratio of 43 has been monitored using a heat ramp β of 1 K/s. Two different states labeled A and B can be identified in the TD spectrum. In advance, the sample has been exposed to decanethiol vapor of a dose of approximately 100 L.
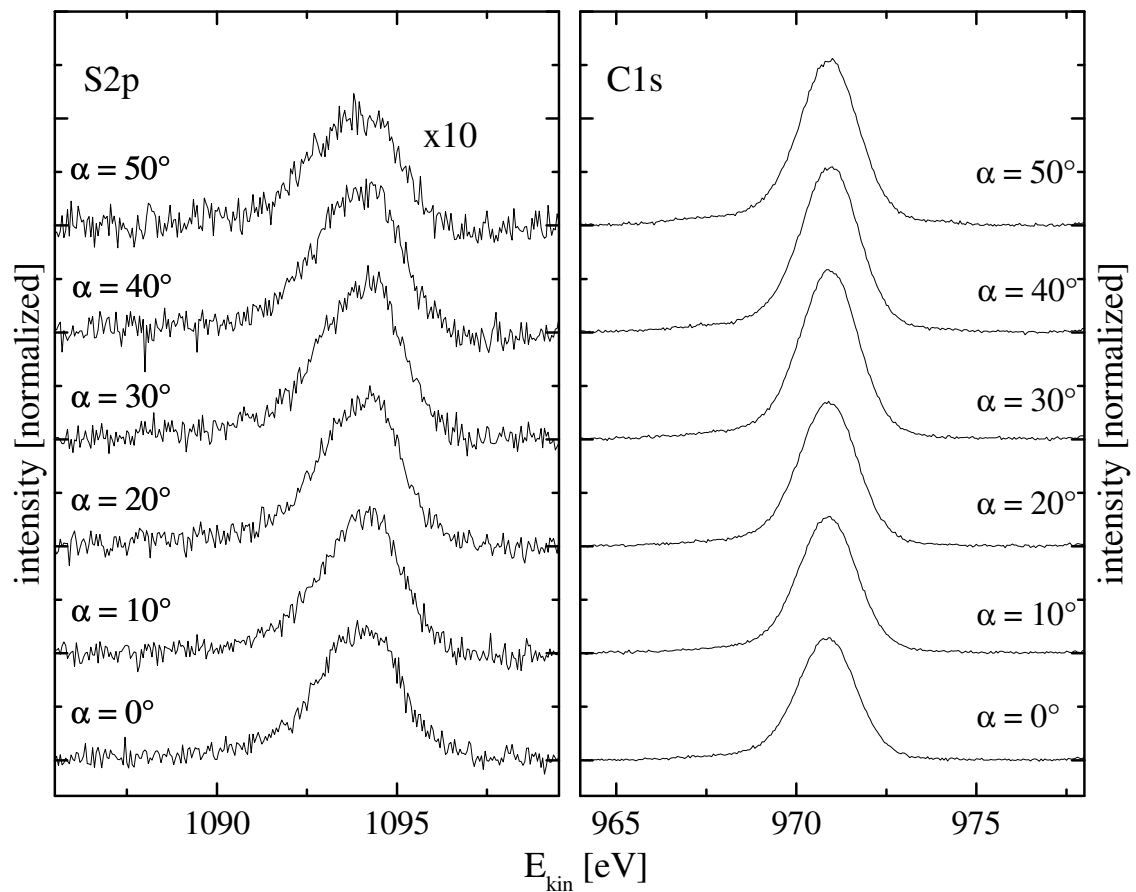
Figure 5.3.: **XPS spectra measured with different emission angles.** Data sets of S2p and C1s XPS signals measured under different electron emission angles α with a pass energy E_{pass} of 50 eV. The respective decanethiol-SAM was prepared ex-situ by immersion. The S2p spectra were multiplied by a factor of 10 to ease the comparison to the C1s spectra.
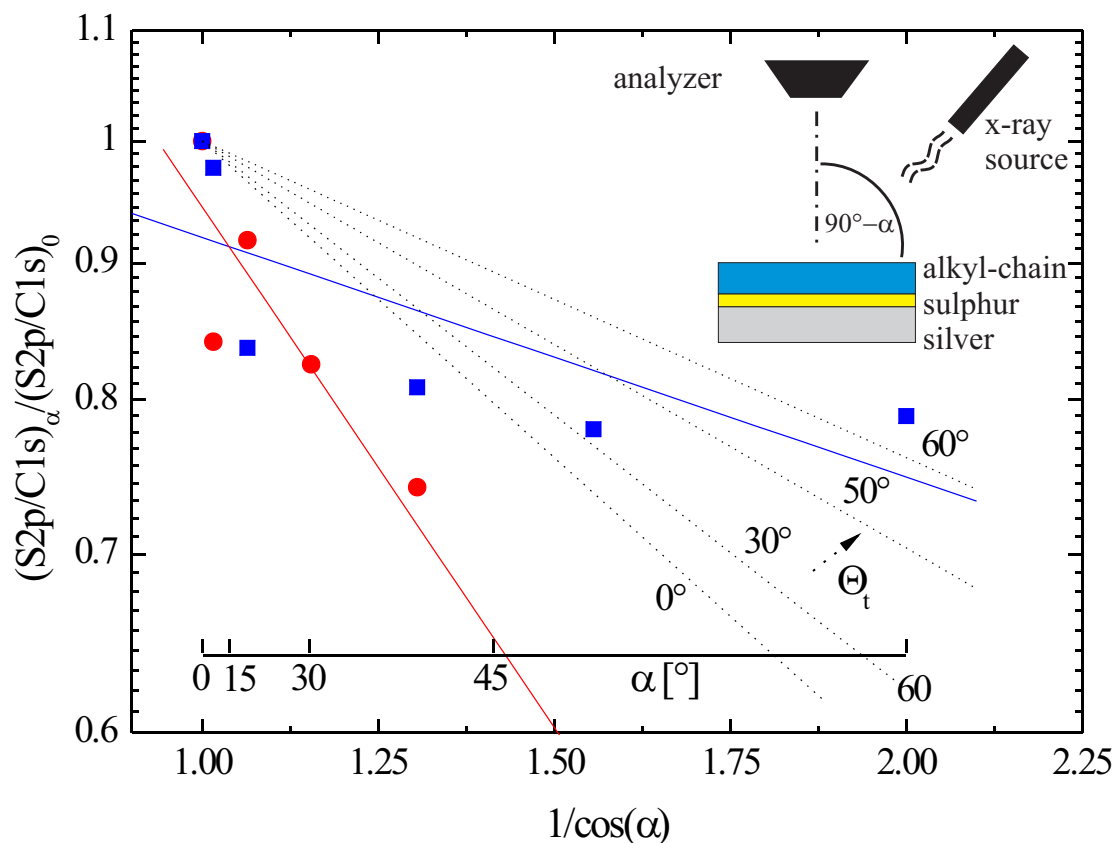
Figure 5.4.: **Attenuation of sulphur photoelectrons.** Decanethiol has been investigated by XPS under different emission angles α with respect to the detector axis. The S2p signals were normalized to the corresponding C1s signal (compare figure 5.3). The red data set was measured for a SAM prepared by immersion, while the blue data set corresponds to a film prepared from CVD. The dashed lines were obtained assuming a Lambert-Beer-type of electron attenuation (see equation 5.2) for the simple layer model given in the inset. The respective theoretical curves are indicated by dotted lines for different tilt angles Θ_t of the molecules.

and being detected. This attenuation of the signal intensity follows a Lambert-Beer-law,

$$\frac{I_E}{I_{0E}} = exp\left(-\frac{l}{\lambda_E}\right),$$

(5.1)

with I_{0E} and I_E being the initial and the detected intensity, l the propagation length through the hydrocarbons, and λ_E the inelastic mean free path of kinetic energy E.

The actual path length of the photoelectrons through the hydro-carbons can be altered by varying the inclination angle α of the sample surface with respect to the analyzer axis (see inset in figure 5.4). But since the effective area seen by the detector changes under such a rotation, the sulphur signal has to be normalized. It is suitable to choose a signal associated with the carbon layer for this purpose since the corresponding intensity variations are mainly based on geometric effects.

In the XPS setup, the electrons were excited by MgK_α-radiation (hν=1253.6 eV) and detected by an electron analyzer with a pass energy E_{pass} of 50 eV. The intensity attenuation of the S2p-peak was investigated. For normalization, it was divided by the corresponding intensity of the C1s-signal. A set of spectra of the same sample under different emission angles α is given in figure 5.3 as example for the quality of the raw data.

In figure 5.4, a normalized data set measured for a decanethiol film prepared from CVD (blue squares) is compared to a data set measured for a film prepared by immersion (red dots) in a semi-logarithmic plot. In the latter case, the substrate had been immersed in 96% decanethiol solution for 60 hours. The transfer in air into the chamber took approximately 2 minutes.

Although the data points are scattered, they are in agreement with an exponential attenuation. Furthermore, one can deduce a stronger intensity decrease for the film prepared by immersion than for those prepared by CVD by comparing the curvatures of the exponential fits to the data sets (indicated by straight lines). Therefore, the former film proves to be denser than the latter one, in agreement with expectations.

The attenuation of the photoelectrons can be estimated using a very simple model consisting of a sulphur atom layer covered by a perfect layer of hydro-carbons (see inset of figure 5.4). The thickness l of the hydro-carbon layer is determined by the length l_0 of the alkyl-chain, and the tilt angle Θ_t of the molecules in the film. The physically relevant escape length of the electrons is inversely proportional to the cosine of the inclination angle α of the sample. Assuming a Lambert-Beer type of attenuation (5.1), one obtains the following functional dependence for the

normalized data:

$$\frac{\left[\frac{I_{S2p}}{I_{C1s}}\right](\alpha)}{\left[\frac{I_{S2p}}{I_{C1s}}\right](0)} = exp\left(-\frac{l_0 cos\left(\Theta_t\right)}{\lambda}\left(\frac{1}{cos\left(\alpha\right)}-1\right)\right). \tag{5.2}$$

The results for four different tilt angles Θ_t are represented by dotted lines in figure. To model the decanethiol layer, a length l_0 of the alkyl-chain of 16.4 Å [209] and an inelastic mean free path λ of 30 Å for a kinetic energy of 1094 eV [212] were used. The agreement with the experimental data is not very convincing. Although perfect layers of alkyl-chains have been assumed, especially the immersed data set lies outside the range of the calculations.

Obviously, the simple model does not reflect the reality. But the systematics of the deviation cannot be explained by domains or imperfect hydro-carbon layers, which are very reasonable to be expected in the real films. Such an effect would decrease the attenuation of electrons and not increase it compared to the theoretical model. The fact that the photoelectrons of the denser films are stronger attenuated than in the model of perfectly upright-standing molecules ($\Theta_t=0$) indicates the real inelastic mean free path to be smaller than the one predicted by theory [212].

Nevertheless, one should not forget that there is a number of important details which are not included in the model. In particular, one has to think of experimental artifacts like, e.g., edge effects, or the finite angle of acceptance of the analyzer.

Together, one can conclude the SAMs to be at least in part upright-standing both for immersion- and CVD-grown films. The quality of the former films, however, is apparently better than the quality of the latter ones. Thus, the present results are in agreement with literature [198–200].

5.3. Coadsorption of $C_{10}SH$ on PTCDA/Ag(10 8 7)

As promised in the motivation of this chapter, SAM growth on the PTCDA-pre-patterned Ag(10 8 7) substrate has been investigated, too.

For this purpose, the PTCDA/Ag(10 8 7) interface was prepared first. Partial coverages of a monolayer of PTCDA were adsorbed onto the Ag(10 8 7) crystal kept at room temperature. Subsequently, the interface was annealed, checked by LEED for the faceting to be successful, and its PTCDA coverage determined by XPS. Finally, the structured template was exposed to decanethiol vapor following the procedure described in the previous section.

In the following, we will discuss a complete data set of a sample with a partial PTCDA-coverage of (0.75±0.02) ML and a nominal decanethiol coverage of (0.36± 0.02) ML. The coverages are given in fractions of the monolayer of the respective pure films on Ag(111). This definition is problematic in the case of the SAM, for
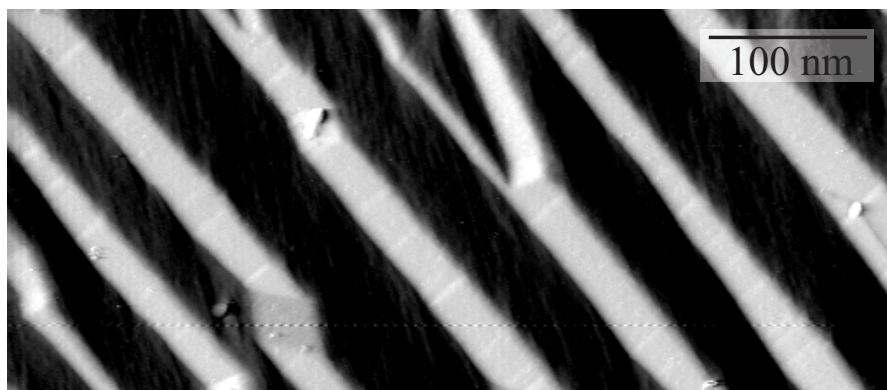
Figure 5.5.: **Morphology observed at a heterostructure.** STM image taken after adsorption of 0.36 ML decanethiol on the pre-patterned PTCDA/Ag(10 8 7) interface. The partial PTCDA coverage of the Ag(10 8 7) sample is 0.75 ML. The image is differentiated for contrast enhancement. High-index facets appear white, (111) terraces black. (Tunneling parameters: I=1.3 nA, U=-1.30 V)

which the "monolayer coverage" depends on the preparation conditions. In the following discussion, it refers to the coverage obtained by CVD under the same conditions on a clean Ag(111) crystal.

Morphology

The morphology of the heterostructure has been studied by scanning tunneling microscopy (STM). In general, imaging conditions have turned out to be complicated for these interfaces. Stable contrast was only achieved for tunneling currents I higher than 1.0 nA and absolute tunneling voltages U above 1.0 V. Individual molecules, however, have never been resolved in our experiments.

The mesoscopic morphology of the heterostructure is depicted in figure 5.5. To enhance contrast, the image has been differentiated. In analogy to figure 4.2, the white stripes in figure 5.5 can be ascribed to high-index facets, and the black areas to (111) terraces. This morphology reflects the properties of the PTCDA/Ag(10 8 7) interface. The faceted, self-ordered structure has therefore endured the second step of preparation.

Domains of decanethiol, however, have not been resolved in our experiments. Tunneling regimes of voltages in the order of 1.0-1.5 V and tunneling currents in the order of 0.2 nA have been reported for undecanethiol (C$_{11}$SH) on Ag(111) in literature [205]. In our case, no stable imaging conditions have been achieved, since the tip was constantly altering in this regime.

Therefore, one can conclude the template structure to determine the morphology of the heterostructure. But based on the STM data, it is not possible to decide

whether the preparation was successful to grow stripes of decanethiol, or whether the material is distributed over the PTCDA/Ag(10 8 7) interface in a different way.

XPS analysis of the heterostructure

Additional information on the composit interfaces can be gained by XPS. Therefore, the C1s-signal was studied both before and after exposure to the decanethiol vapor. For these experiments, a pass energy of 20 eV was used.

In figure 5.6a the data of the same heterostructure is given whose STM data has already been discussed in the previous paragraphs. The signal of the intermediate preparation step (i.e. the "pure" PTCDA/Ag(10 8 7) interface) is indicated by the orange dashed line, and the black solid line renders the data of the completed heterostructure.

Obviously, the difference between these two curves can be ascribed to the carbon of the adsorbed decanethiol molecules. The integrated difference corresponds to 36% of the intensity of a "pure", CVD-grown SAM on Ag(111). In fact, when adding a C1s signal of a "pure" SAM scaled accordingly (blue dotted line in figure 5.3) to the intermediate signal, the XPS data of the heterostructure can be reasonably well reproduced (compare the solid black line with the dash-dotted red one in figure 5.6).

Further information on the growth mode can be deduced by comparison of these results to a verification experiment summarized in figure 5.6b. In this latter experiment, a closed monolayer of PTCDA was prepared on a Ag(111) substrate by multilayer desorption. Subsequently, it was exposed to decanethiol vapor, in complete analogy to the procedure applied to the templates.

For this interface, only a small difference before and after exposure can be identified in the C1s data (compare figure 5.6b). It corresponds to 10% of the intensity of a closed decanethiol film. Again, the sum of the assumed components reproduces the final intensity reasonably well. Hence, one can deduce the Ag(111) faces to be passivated against decanethiol vapor when covered by PTCDA. Nevertheless, a small fraction cannot be excluded to stick to the surface, possibly in the vicinity of defects, at step edges or domain boundaries or even on top of the PTCDA layer

Finally, returning to the analysis of the heterostructure, it appears reasonable to assume the decanethiol molecules to be adsorbed preferably on the uncovered Ag(111) terraces. The nominal "over-coverage" of 10% when adding 0.75 ML of PTCDA to 0.36 ML of decanethiol could have three reasons. First, the density of the decanethiol molecules could be higher on the template than on the unstructured Ag(111) surface, which would actually improve the quality of the SAMs. Second, a fraction of the molecules could stick on top of the PTCDA molecules or be pinned at exceptional morphological objects, which would be less favorable for a "perfect" chemical patterning. At last, it could of course also simply reflect in part the error bar of the coverage determination.
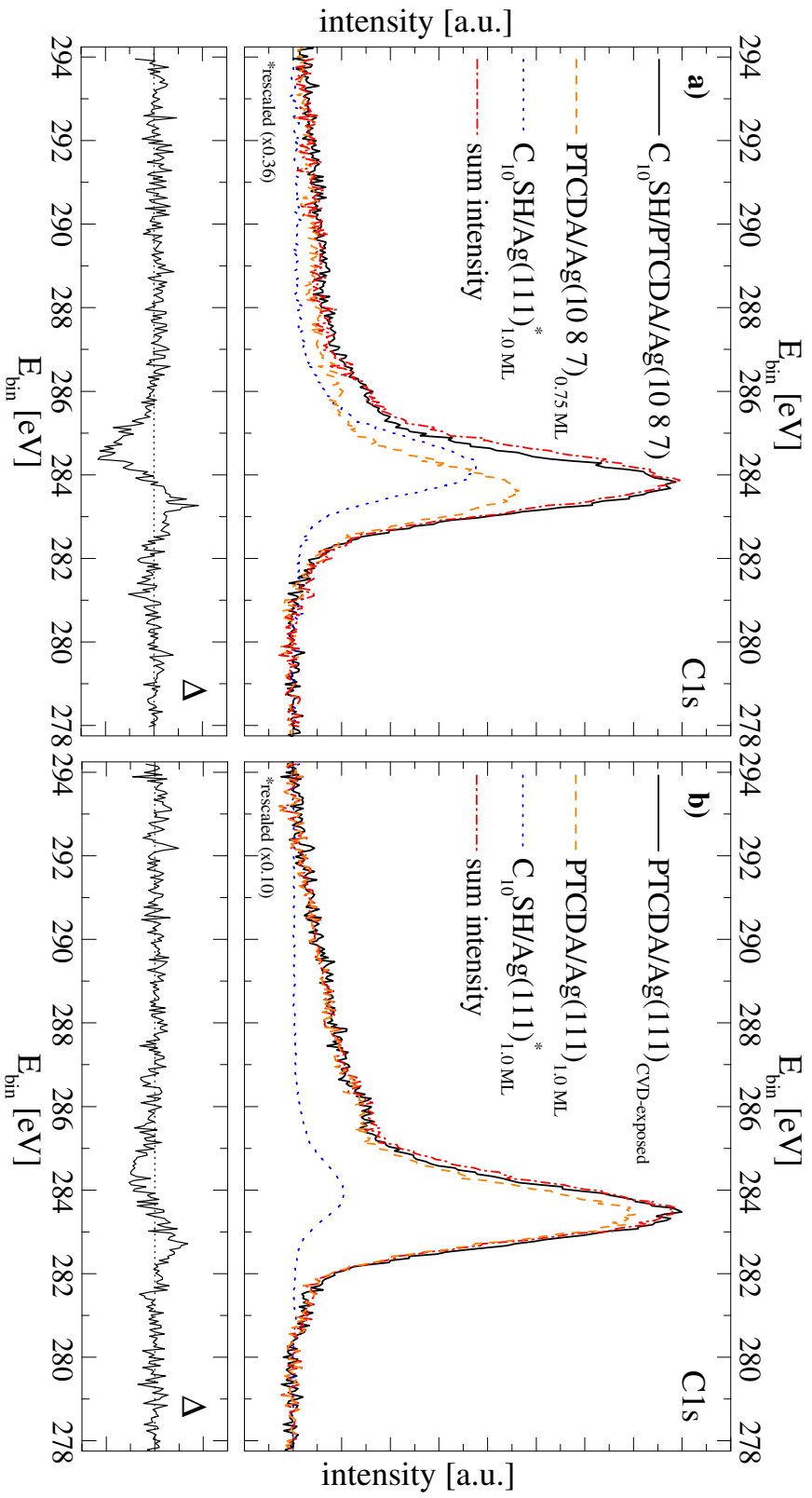
Figure 5.6.: **Spectroscopic analysis of C_{10}SH/PTCDA/Ag(111) interfaces.** XPS measurements of the binding energy interval corresponding to the C1s signal. **a)** A faceted PTCDA/Ag(10 8 7) interface with a partial molecular coverage of 0.75 ML (dashed orange line) was exposed to decanethiol (C_{10}SH) vapor. The resulting experimental signal intensity (solid black line) can be constructed by summing the former signal with the intensity corresponding to 0.36 ML of decanethiol on Ag(111) (dotted blue line). The residuum between this summation (dash-dotted red line) and the experimental result is given in the lower graph (labeled Δ). **b)** An analogous experiment performed on a PTCDA/Ag(111) interface passivated by a coverage of a closed monolayer of PTCDA.

5.4. Discussion and conclusion

A mixed picture can be gained from the experimental data: On one hand, they indeed reflect the properties which one would expect from template-assisted growth. The data of the x-ray photoemission spectroscopy shows the stoichiometry of the chemically patterned surface. Moreover, the STM data confirms the morphology to be as expected.

But both XPS and STM indicate a small fraction of decanethiol molecules to adsorb also on top of PTCDA molecules. The spectroscopic data of the verification experiment suggests such a conclusion, and the fact, that no individual PTCDA molecules have been resolved by STM would also fit to such an interpretation.

The fact, however, that no domains of decanethiol molecules have been found in the heterostructure by STM is less conclusive. This finding is probably due to experimental reasons since the optimal tunneling conditions of these molecules are at the limit of the electronics of the used STM.

The preliminary studies of the CVD process provide some confidence in the quality of the decanethiol-SAMs. Especially the fingerprint of two desorption states in the TDS data, but also the measurement of the attenuation of the photoelectrons support the assumption of at least domains of upright-standing molecules.

In conclusion, self-assembled monolayers have been grown by chemical vapor deposition in a quality which can be expected from literature. The heterostructures grown by subsequent adsorption of PTCDA and decanethiol on Ag(10 8 7) might not be perfect from the point of view of chemical phase separation. But their morphology is at least still governed by the template morphology. Therefore, the basic concept of template-assisted growth of heterorganic structures has been successfully demonstrated.

Nevertheless, the results also show that the experimental insight into these more complicated mesoscopic heterostructures should combine a high lateral resolution with chemical sensitivity. A suitable technique for such an investigation could be modern spectro-microscopy, for example, as used in chapter 4. Such experiments were not possible at the time when the coadsorption experiments were performed.

Summary

The role of elastic interactions, particularly for the self-organized formation of periodically faceted interfaces, was investigated in this thesis for archetype organic-metal interfaces.

The cantilever bending technique was applied to study the change of surface stress upon formation of the interface between 3,4,9,10-perylene-tetracarboxylic-dianhydride (PTCDA) and Ag(111). This system is known to form a chemisorptive bonding. Indeed, the sign and the coverage-dependence of the surface stress change are in agreement to models and previous measurements of chemisorptive systems in literature. While the adsorption of molecules into the large domains is associated with a negative, i.e. compressive stress change, the formation of domain boundaries in the molecular layer induces a stress change of opposite sign, increasing the surface stress. The magnitude of the surface stress change of (-0.30 ± 0.10) N/m reflects a relatively weak binding of a PTCDA molecule to each individual single silver atom. It is emphasized, however, that if normalized to the surface stress change per molecule, this value corresponds to a stress change of (-2.2 ± 0.2) eV per molecule which is in the order of the suspected binding energy of this system. Therefore, these experiments reveal elastic interactions to be of significant order of magnitude for this system class. Thereby, they add a new point of view to the understanding of these interfaces. Besides, since the results are in agreement with the well-known properties of this interface, they establish the cantilever bending technique in the field of organic-metal interfaces.

The mere existence of a bending of the sample implies an interesting detail for the PTCDA/Ag(111) interface in particular. It is the first experimental evidence

for a structural change in the topmost substrate layers upon adsorption of PTCDA on Ag(111). Since such a modification has significant implications for the interpretation of other experimental results, a further investigation with more quantitative structural methods appears necessary.

The main focus of this work, however, was on the investigation of the formation of the long-range ordered, self-organized faceted PTCDA/Ag(10 8 7) interface. Reciprocal space maps of this interface were recorded both by spot profile analysis low energy electron diffraction (SPA-LEED) and low energy electron microscopy (LEEM) in selected area LEED mode. Complementary to the reciprocal data, also microscopic real-space LEEM data were used to characterize the morphology of this interface. Six different facet faces ((111), (532), (743), (954), (13 9 5), and (542)) were observed for the preparation path of molecular adsorption on the substrate kept at 550 K. Facet-sensitive dark-field LEEM localized these facets to grow in homogeneous areas of microscopic extensions. If the pristine mesoscopic orientation locally deviates from the average orientation, e.g. in pristine step density, locally different facet types are formed, distorting the otherwise regular mesoscopic pattern. Hence, the original mesoscopic orientation of the substrate strongly determines the degree of order of the faceted surface and the facet species formed.

The temperature-dependence of the interface formation was studied in a range between 418 K and 612 K in order to learn more about the kinetics of the process. Additional steeper facets of 27° inclination with respect to the (111) surface were observed in the low temperature regime. Furthermore, using facet-sensitive dark-field LEEM, spatial and size distributions of specific facets were studied for the different temperatures. The nucleation density of the facets did not depend on temperature and can therefore be concluded not to be limited by diffusion. Moreover, the facet dimensions were statistically analyzed. The total island size of the facets follows an exponential distribution, indicating a random growth mode in absence of any mutual facet interactions. While the length distribution of the facets also follows an exponential distribution, the width distribution is peaked, reflecting the high degree of lateral order. This anisotropy is temperature-dependent and occurs starting above 478 K substrate temperature during growth. The peaked distribution indicates the presence of a long-range interaction which leads to the structural order of the self-organized grating.

The origin of this long-range interaction was investigated combining three complementary in-situ methods, all providing new insights into the formation of faceted organic-metal interfaces: the cantilever bending technique, high-resolution low energy electron diffraction (SPA-LEED), and microscopy (LEEM).

The cantilever bending technique was applied for the first time to a faceting system at all. Below the faceting transition temperature the surface stress change associated with the formation of the PTCDA/Ag(10 8 7) interface resembles in shape and magnitude the one observed for the reference interface PTCDA/Ag(111). But above the transition temperature the absolute surface stress change of (-0.67 ± 0.10)

N/m observed for the faceted PTCDA/Ag(10 8 7) interface is considerably larger than for the previous cases. Moreover, the stress change happens in distinguishable stages with a clearly resolvable fine structure of regimes of positive and negative stress changes. These different regimes of surface stress change can be correlated to different stages of the structural phase transition observed by the structural in-situ methods. Thereby, morphological objects (i.e. the facets) are assigned to a specific stress character. Thus, domains of different stress character can be identified on the surface. These stress domains are the prerequisite to apply continuum descriptions of the self-ordering process based on elastic interactions. Hence, the results are the first experimental verification that these continuum descriptions are indeed also applicable to the whole system class of faceting organic-metal interfaces. In conclusion, the results provide strong evidence for elastic interactions being the physical origin of long-range order for this system.

In addition, the clear correlation of structural phase transition and surface stress change regimes suggests surface stress to play also an important role for the kinetics of the system. Indeed, the system seems to try to limit the overall stress change during the interface formation by forming facets of positive and negative stress character. Hence, the selection of specific facets could depend on the corresponding stress character. Furthermore, the system seems willing to re-facet at high coverages in order to prevent imperfect domain boundaries which are associated with an increase of surface stress.

Finally, template-assisted growth of lateral, heterorganic nanostructures has been explored. Therefore, self-assembled monolayers as a second archetype class of molecules were grown on partially covered PTCDA/Ag(10 8 7) interfaces. Indeed, using standard surface science techniques, the basic principle of this growth scheme was confirmed to be successful.

Zusammenfassung

Anhand von Modellsystemen wurde in dieser Arbeit die Bedeutung elastischer Wechselwirkungen an Organik-Metall Grenzflächen, insbesondere für die selbstorganisierte Ausbildung periodisch facettierter Strukturen, untersucht.

Die Änderung der Oberflächenspannung während der Ausbildung der Grenzfläche zwischen 3,4,9,10-Perylentetracarbonsäuredianhydrid (PTCDA) und Ag(111) wurde mit der Biegekristalltechnik gemessen. Es ist bekannt, dass dieses System durch eine chemisorptive Bindung bestimmt wird. In der Tat stimmen Vorzeichen und Bedeckungsabhängigkeit mit Vorhersagen und Experimenten aus der Literatur zu chemisorptiv bestimmten Grenzflächen überein. Während der Einbau von Molekülen in große Domänen die Oberflächenspannung verringert, führt das Auftreten von fehlerhaften Domänengrenzen zu einer Erhöhung der Oberflächenspannung. Die absolute Änderung der Oberflächenspannung in der Höhe von (-0.30 ± 0.10) N/m ist in der relativ schwachen Wechselwirkung des PTCDA Moleküls mit einem einzelnen Silberatom begründet. Es soll jedoch betont werden, dass dieser Wert einer Oberflächenspannungsänderung von (-2.2 ± 0.2) eV pro Molekül entspricht, die damit in derselben Größenordnung wie die vermutete Bindungsenergie des Systems liegt. Daher zeigen diese Experimente, dass elastische Wechselwirkungen eine nicht zu vernachlässigende Rolle in dieser ganzen Materialklasse spielen können. Dadurch tragen die Experimente eine neue Sichtweise zum Verständnis dieser Grenzflächen bei. Ferner etablieren sie die Biegekristalltechnik auf dem ganzen Feld der Organik-Metall Grenzflächen, da die Ergebnisse in Einklang mit den wohlbekannten Eigenschaften des Systems liegen.

Schon der Nachweis einer Durchbiegung der Probe ist speziell für die Grenz-

fläche PTCDA/Ag(111) von Bedeutung. Dieser Effekt ist der erste experimentelle Nachweis einer strukturellen Änderung in den obersten Substratatomlagen während der Adsorption von PTCDA auf Ag(111). Da eine solche Modifikation nicht zu vernachlässigende Konsequenzen für die Interpretation anderer experimenteller Ergebnisse hat, erscheinen weitere Studien mit anderen, quantitativeren strukturellen Methoden notwendig.

Der Schwerpunkt dieser Arbeit lag jedoch auf der Untersuchung der Ausbildung der langreichweitigen, selbstorganisierten Ordnung der facettierten PTCDA/Ag(10 8 7) Grenzfläche. Der reziproke Raum dieser Grenzfläche wurde sowohl mit mittelnder hochauflösender Elektronenbeugung (SPA-LEED) als auch mit lokaler Elektronenbeugung in der Mikroskopie niederenergetischer Elektronen (LEEM) kartiert. Außerdem wurden diese reziproken Daten durch mikroskopische LEEM Realraumdaten komplementär ergänzt um die Morphologie der Grenzfläche zu charakterisieren. Für die gewählte Präparationsart, Adsorption der Moleküle auf das 550 K warme Substrat, wurden sechs verschiedene Facettentypen ((111), (532), (743), (954), (13 9 5) und (542)) beobachtet. Diese Facettentypen treten in homogenen, mikrometergroßen Gebieten auf der Oberfläche auf, wie Dunkelfeld-LEEM-Aufnahmen zeigen. Wenn jedoch die ursprüngliche mesoskopische Orientierung der Oberfläche lokal von der Durchschnittsorientierung z.B. in Bezug auf die ursprüngliche Stufendichte abweicht, werden an dieser Stelle andere Facettentypen gebildet und damit das ansonsten regelmäßige Muster gestört. Sowohl der Grad der erreichten Ordnung der facettierten Grenzfläche als auch die gebildeten Facettentypen hängen somit stark von der ursprünglichen mesoskopischen Morphologie des sauberen Substrates ab.

Um das Verständnis der kinetischen Prozesse zu verbessern wurde die Temperaturabhängigkeit der Ausbildung der Grenzfläche in einem Temperaturbereich zwischen 418 K und 612 K untersucht. Bei niedrigen Wachstumstemperaturen traten zusätzliche, steilere Facetten mit einem Neigungswinkel von 27° gegenüber der (111) Fläche auf. Weiterhin wurde mit Facetten-sensitivem Dunkelfeld-LEEM die Größen- sowie die räumliche Verteilung ausgewählter Facettentypen bei den verschiedenen Temperaturen untersucht. Die Nukleationsdichte der Facetten zeigte dabei keine Temperaturabhängigkeit. Eine Diffusionslimitierung der Nukleation kann daher ausgeschlossen werden. Darüber hinaus wurden die Ausmaße der Facetten statistisch ausgewertet. Die absolute Facettengröße folgt einer exponentiellen Verteilung, was auf ein zufallsgetriebenes Wachstum und das Fehlen einer Wechselwirkung der Facetten untereinander hinweist. Während die Facettenlängen ebenso einer exponentiellen Verteilung unterliegen, ist die Breitenverteilung durch ein Maximum ausgezeichnet. Letztere Verteilung spiegelt den hohen Grad an lateraler Ordnung in dem System wieder. Diese Anisotropie hängt von der Temperatur ab und kann bei Substrattemperaturen über 478 K während des Wachstums beobachtet werden. Die Existenz eines Maximums in einer solchen Größenverteilung weist auf eine langreichweitige Wechselwirkung hin, die die strukturelle Ordnung

induziert.

Die Natur dieser langreichweitigen Wechselwirkung wurde mit drei komplementären in-situ Methoden untersucht, wobei jeweils neue Einblicke in die Ausbildung von facettierten Organik-Metall-Grenzflächen gewonnen werden konnten: Die Biegekristalltechnik, hochauflösende Beugung niederenergetischer Elektronen (SPA-LEED), sowie deren Mikroskopie (LEEM).

Die Biegekristalltechnik wurde das erste Mal überhaupt auf ein facettierendes System angewendet. Unterhalb der kritischen Temperatur des Facettierungsübergangs ähnelt die Oberflächenspannungsänderung während der Bildung der PTCDA/Ag(10 8 7)-Grenzflächenbildung sowohl in funktionaler Abhängigkeit als auch in der Größenordnung der für die Referenzgrenzfläche PTCDA/Ag(111) beobachteten. Oberhalb der Übergangstemperatur beobachtet man jedoch für die ausfacettierte PTCDA/Ag(10 8 7) Grenzfläche mit (-0.67 ± 0.10) N/m eine bedeutend größere Oberflächenspannungsänderung als in den vorherigen Fällen. Zudem ändert sich die Oberflächenspannung in klar unterscheidbaren Schritten mit einer eindeutig auflösbaren Feinstruktur aus positiven und negativen Spannungsänderungen. Diese einzelnen Phasen in der Änderung der Oberflächenspannung können Stufen in der Entwicklung der Strukturüberganges dieses Systems zugeordnet werden, die mit den strukturellen Charakterisierungsmethoden beobachtet wurden. Durch diese Identifikation werden morphologischen Objekten, also den Facetten, ein eigener besonderer Spannungscharakter zugeordnet. Somit werden aber auch Spannungsdomänen auf der Oberfläche identifiziert. Die Existenz dieser Spannungsdomänen ist nun aber die Vorraussetzung für die Anwendung von elastizitätsbasierten Kontinuumsbeschreibungen des Selbstordnungseffektes. Daher stellen diese Ergebnisse den ersten experimentellen Nachweis dar, dass diese Kontinuumsbeschreibungen der Selbstorganisation tatsächlich auch auf die gesamte Materialklasse der facettierenden Organik-Metall-Grenzflächen angewendet werden können. Zusammengefasst sind diese Ergebnisse starke Beweise dafür, dass elastische Wechselwirkungen der physikalische Ursprung der langreichweitigen Ordnung dieses Systems sind.

Weiterhin legt die eindeutige Korrelation zwischen strukturellem Phasenübergang und Oberflächenspannungsänderung auch nahe, dass letzterer ebenso eine wichtige Rolle in der Kinetik des Systems spielt. Tatsächlich scheint das System zu versuchen die Gesamtänderung der Oberflächenspannung während der Grenzflächenbildung durch die Bildung von Facettentypen positiven und negativen Charakters zu begrenzen. Daher könnte die Art ihres Beitrags zur Oberflächenspannungsänderung darüber entscheiden, ob eine bestimmte Facettenorientierung gebildet wird oder nicht. Auch scheint das System sich bei hohen Bedeckungen unter anderem deshalb erneut umzufacettieren um der Bildung von fehlerhaften Domänengrenzen entgegenzuwirken, die mit einem Anstieg der Oberflächenspannung verbunden wären.

Schließlich wurde im Rahmen dieser Arbeit noch das templatunterstützten Wachstum lateraler, heteroorganischer Nanostrukturen untersucht. Dabei wurde ein

zweites, typisches molekulares Modellsystem, sogenannte "Selbstassemblierte Mono-lagen", auf der teilbedeckten PTCDA/Ag(10 8 7) Grenzfläche aufgewachsen. Mit Standardmethoden der Oberflächencharakterisierung konnte nachgewiesen werden, dass die grundlegenden Eigenschaften dieses Wachstumsprinzips im Experiment in der Tat erreicht werden.

Appendix

List of abbreviations

Quantities denoted by Latin capital letters:

E_{bin}	binding energy
E_d	activation energy for diffusion
E_i	binding energy associated with a critical island
E_{kin}	kinetic energy
i	critical atom number for an island to be stable; often also index number
k	Boltzmann factor
N_s	density of stable islands of size s per adsorption site
N_x	density of stable islands per adsorption site: $N_x = \sum_s N_s$
R	adsorption rate
s	number of atoms in a stable island ($s \geq i$)
s_{av}	average number of atoms per stable island
S	scaled island size S:=s/s_{av}; also scattering phase in diffraction
S_A	PTCDA/Ag(111) superstructure
T	absolute temperature
u	displacement field
Y	Young's modulus

Acronyms of surface science used in this thesis:

2PPE	two photon photoemission
AFM	atomic force microscope
BF	bright-field
BZ	brillouin zone
CVD	chemical vapor deposition
DFT	density functional theory
ECS	equilibrium crystal shape
ED	electron diffraction
EXAFS	extended x-ray-absorption fine-structure
GIXD	grazing incidence x-ray diffraction
HOMO	highest occupied molecular orbital
HREM	high resolution electron microscopy
LEED	low energy electron diffraction
LEEM	low energy electron microscopy
LUMO	lowest unoccupied molecular orbital
ML	monolayer
NEXAFS	near edge x-ray adsorption fine structure
OMBD	organic molecular beam deposition
PEEM	photoemission electron microscopy
PTCDA	3,4,9,10-perylene-tetracarboxylic-dianhydride
QMS	quadrupole mass spectrometer
SAM	self-assembled monolayer
SPA-LEED	spot profile analysis low energy electron diffraction
STM	scanning tunneling microscopy
TDS	thermal desorption spectroscopy
TEM	transmission electron microscopy
UHV	ultra high vacuum
XPS	x-ray photoelectron spectroscopy
XSW	x-ray standing wave

Quantities denoted by Greek capital letters:

γ	specific surface free energy
Γ	average terrace width
$\Delta\tau$	surface stress change
ϵ	surface strain tensor
ϵ^b	bulk strain tensor
Θ	coverage; also polar coordinate of facets
Θ_x	coverage associated with stable islands
Θ_t	tilting angle of molecules in SAMs
κ	compressibility
ν	Poisson's ratio
ν_v	vibrational pre-factor or attempt frequency
τ	surface stress tensor
τ^b	bulk stress tensor
Φ	azimuthal coordinate of facets

Sample mount for cantilever experiments

In the cantilever bending experiment described in chapter 2.3, the sample must be clamped strongly on one short edge , while the rest is allowed to bend freely.

In order to implement this sample mounting into the UHV set up, an adaptor sample mount was made from molybdenum (Mo) and attached to the standard transferable sample mounts used in Würzburg [17]. It is depicted in figure B.1.

The strong clamping is achieved by the help of a screw. It connects the thin cover clamp with the round sample mount of molybdenum. The cantilever itself is sandwiched between a tungsten (W) wire (diameter 0.38 mm) and a thin molybdenum foil (thickness 0.05 mm). Both covers prevent the sample from sticking to the sample mount after being heated. In addition, the tungsten wire fixes the sample and thereby makes the actual mounting of the fragile crystals easier.

Furthermore, surface stress change can be induced by all adsorption processes. Therefore, any evaporation on the back side of the sample must be inhibited during the measurement. As a consequence, the sample is shielded from the tantalum heating coil by a silver sheet (thickness 0.25 mm).

The temperature is measured using a chromel-alumel K-type thermocouple sensor. It is fixed to the cantilever crystal by a tungsten wire. The temperature measured at this spot has been calibrated to the temperature of the free protruding crystal by a reference experiment. For this purpose, the cantilever was replaced by a Ag foil of thickness 0.1 mm. A second thermocouple could then be attached to the protruding part of the cantilever. This measurement was repeated for all

Figure B.1.: **Cantilever sample mount.** The major components of the mount are labeled. It can be attached to the standard transferable sample mount used at Würzburg [17].

sample mounts used.

External influences in SPA-LEED

A "blind experiment" has been performed to identify external influences on the acquired SPA-LEED data. Therefore, a Ag(10 8 7) crystal already covered by a monolayer of PTCDA and completely faceted has undergone the same experimental procedure as in the experiments discussed in chapter 4.5.2. As in the case of the cantilever test experiments, the thus passivated sample is quasi inert against further PTCDA exposure if kept at 550 K.

As can be seen in figure C.1, the shutter opening induces a shift in the detected lateral position of the peaks in k-space. It is reversed when the shutter is closed again. When decreasing the evaporator heating current gradually, a slow continuous lateral drift can also be observed in the lateral peak positions. It gets abrupt when the evaporator is switched off.

Based on these observations, the magnetic field of the evaporator (heated with a spiral coaxial wire heating - for details see Kröger [57]) is supposed to be responsible for the shifting electron peaks. To limit this effect, it was avoided to switch the evaporator completely off during data acquisition. Furthermore, to account for the overall drift, the mutual peak distances were kept fixed in the fit routines, while an absolute lateral shift of the ensemble was allowed for each single line scan.
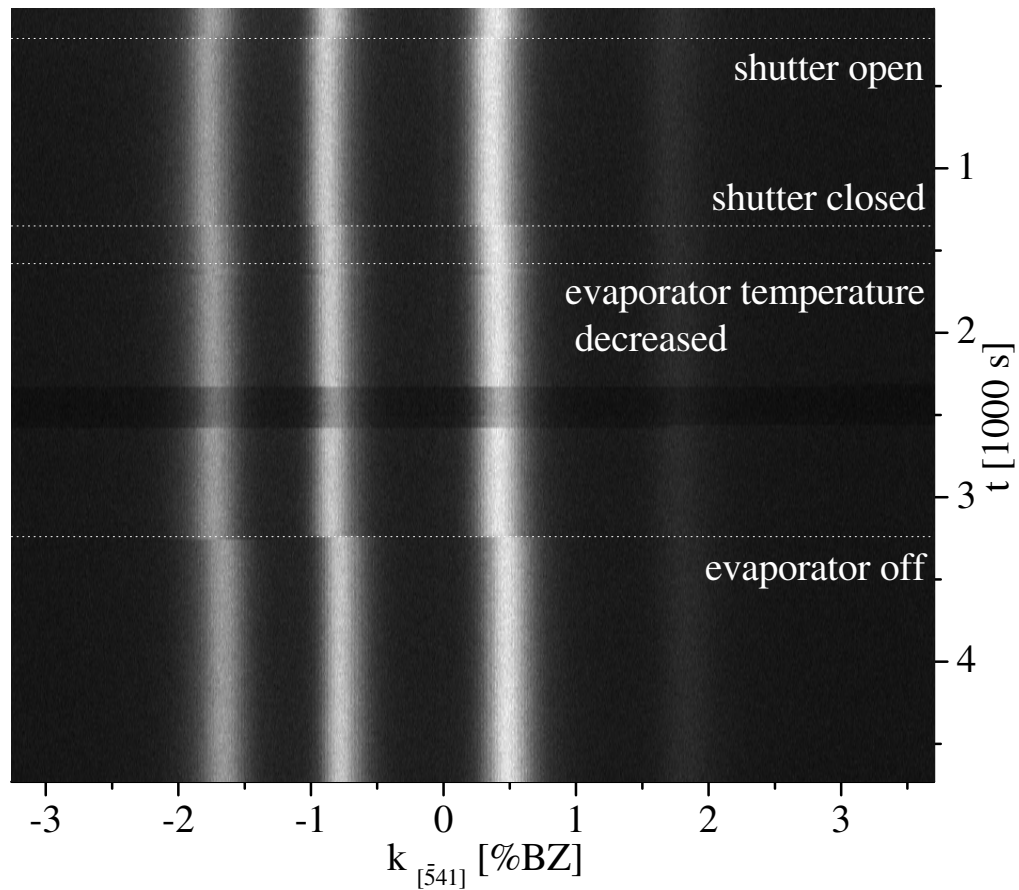
Figure C.1.: **External influences on the SPA-LEED data.** The sample which is completely PTCDA-covered and faceted is kept at 550 K. Thus passivated, it is exposed to shutter movements and evaporator-induced effects. Each test event is marked by a white dashed line.

Bibliography

[1] G. M. Whitesides and B. Grzybowski. Self-assembly at all scales. *Science*, 295(5564):2418–2421, 2002.

[2] J. V. Barth, G. Costantini, and K. Kern. Engineering atomic and molecular nanostructures at surfaces. *Nature*, 437(7059):671–679, 2005.

[3] A. Hoffknecht and D. Wechsler. Kontrollierte Selbstorganisation. *Physik Journal*, 4(4):43–46, 2005.

[4] R. Nötzel, Z. C. Niu, M. Ramsteiner, H. P. Schönherr, A. Tranpert, L. Däweritz, and K. H. Ploog. Uniform quantum-dot arrays formed by natural self-faceting on patterned substrates. *Nature*, 392(6671):56–59, 1998.

[5] S. R. Forrest. The path to ubiquitous and low-cost organic electronic appliances on plastic. *Nature*, 428(6986):911–918, 2004.

[6] E. Barrena, D. G. de Oteyza, S. Sellner, H. Dosch, J. O. Osso, and B. Struth. In situ study of the growth of nanodots in organic heteroepitaxy. *Physical Review Letters*, 97(7):076102, 2006.

[7] D. G. de Oteyza, N. Krauss, E. Barrena, S. Sellner, H. Dosch, and J. O. Osso. Towards controlled bottom-up architectures in organic heterostructures. *Applied Physics Letters*, 90(24):243104, 2007.

[8] M. P. Zach, K. H. Ng, and R. M. Penner. Molybdenum nanowires by electrodeposition. *Science*, 290(5499):2120–2123, 2000.

[9] S. Rousset, B. Croset, Y. Girard, G. Prévot, V. Repain, and S. Rohart. Self-organized epitaxial growth on spontaneously nano-patterned templates. *Comptes Rendus Physique*, 6(1):33–46, 2005.

[10] J. Kröger, N. Néel, H. Jensen, R. Berndt, R. Rurali, and N. Lorente. Molecules on vicinal au surfaces studied by scanning tunnelling microscopy. *Journal of Physics Condensed Matter*, 18(13):51–66, 2006.

[11] X. Ma, H. L. Meyerheim, J. Barthel, J. Kirschner, S. Schmitt, and E. Umbach. Self-assembled magnetic nanostripes by organic patterning. *Applied Physics Letters*, 84(20):4038–4040, 2004.

[12] N. Néel, J. Kröger, and R. Berndt. Fullerene nanowires on a vicinal gold surface. *Applied Physics Letters*, 88(16):163101, 2006.

[13] S. X. Du, H. J. Gao, C. Seidel, L. Tsetseris, W. Ji, H. Kopf, L. F. Chi, H. Fuchs, S. J. Pennycook, and S. T. Pantelides. Selective nontemplated adsorption of organic molecules on nanofacets and the role of bonding patterns. *Physical Review Letters*, 97(15):156105, 2006.

[14] V.I. Marchenko. Theory of the equilibrium shape of crystals. *Zh. Eksp. Teor. Fiz. [Sov. Phys. JETP 54 (3), 605 1981]*, 81:1141, 1981.

[15] O. L. Alerhand, D. Vanderbilt, R. D. Meade, and J. D. Joannopoulos. Spontaneous formation of stress domains on crystal-surfaces. *Physical Review Letters*, 61(17):1973–1976, 1988.

[16] David Vanderbilt. Phase segregation and work-function variations on metal surfaces: Spontaneous formation of periodic domain structures. *Surface Science*, 268(1-3):L300–L304, 1992.

[17] Christian Seidel. *Charakterisierung organischer Adsorbate auf Silbereinkristallen mit den Meßmethoden LEED und STM*. Dissertation, Universität Stuttgart, 1993.

[18] L. Kilian. *Adsorption, Struktur und Morphologie hochgeordneter organischer Morphologie hochgeordneter organischer Adsorbatschichten*. Dissertation, Bayerische Julius-Maximilians-Universität Würzburg, 2002.

[19] J. Taborski. *NEXAFS-Untersuchungen an organischen Adsorbaten auf verschiedenen (111)-Oberflächen*. Dissertation, Universität Stuttgart, 1994.

[20] H. Marchetto. *High-resolution spectro-microscopic investigations of organic thin film growth*. Dissertation, Freie Universität Berlin, 2006.

[21] M. P. Marder. *Condensed Matter Physics.* John Wiley & Sons, Inc., New York, corrected printing edition, 2000.

[22] Z. Tian. *private communication.*

[23] S. R. Forrest. Ultrathin organic films grown by organic molecular beam deposition and related techniques. *Chemical Reviews*, 97(6):1793–1896, 1997.

[24] S. Hüfner, editor. *Photoelectron Spectroscopy, Principles and Applications.* Springer Series in Solid-State Sciences. Springer Verlag, Heidelberg, 2nd Edition edition, 1996.

[25] R.I. Masel. *Principles of adsorption and reaction on solid surfaces.* Wiley Series in Chemical engineering. John Wiley & Sons, Inc., New York, 1996.

[26] G. Binning, H. Rohrer, C. Gerber, and E. Weibel. Surface studies by scanning tunneling microscopy. *Physical Review Letters*, 49(1):57–61, 1982.

[27] K. Besocke. An easily operable scanning tunneling microscope. *Surface Science*, 181(1-2):145–153, 1987.

[28] D.A. Bonnell. *Scanning Tunneling Microscopy and Spectroscopy, Theory, Techniques and Applications.* VCH Publishers, Inc., 1993.

[29] U. Herber. *Rastertunnelspektroskopie an polykristallinen Cu(In,Ga)(S,Se)−2-Dünnschichtsolarzellen.* Dissertation, Bayerische Julius-Maximilians-Universität Würzburg, 2006.

[30] G. Ertl and J. Küppers. *Low Energy Electrons and Surface Chemistry.* VCH, Weinheim, 2nd Edition edition, 1985.

[31] U. Scheithauer, G. Meyer, and M. Henzler. A new LEED instrument for quantitative spot profile analysis. *Surface Science*, 178(1-3):441–451, 1986.

[32] M. Horn-von Hoegen. Growth of semiconductor layers studied by spot profile analysing low energy electron diffraction. *Kristallographie*, 214:591–629, 1999.

[33] E. Bauer. Low-energy-electron microscopy. *Reports on Progress in Physics*, 57(9):895–938, 1994.

[34] E. Bauer, M. Mundschau, W. Swiech, and W. Telieps. Surface studies by low-energy electron-microscopy (LEEM) and conventional UV photoemission electron-microscopy (PEEM). *Ultramicroscopy*, 31(1):49–57, 1989.

[35] E. Bauer. LEEM basics. *Surface Review and Letters*, 5(6):1275–1286, 1998.

[36] W. Telieps, M. Mundschau, and E. Bauer. Dark field imaging with LEEM. *Optik*, 77(2):93–97, 1987.

[37] W. Telieps, M. Mundschau, and E. Bauer. Surface domain-structure of reconstructed Au(100) observed by dark field low-energy electron-microscopy. *Surface Science*, 225(1-2):87–96, 1990.

[38] F. J. M. z. Heringdorf, D. Kähler, M. Horn-von Hoegen, T. Schmidt, E. Bauer, M. Copel, and H. Minoda. Giant faceting of vicinal Si(001) induced by Au adsorption. *Surface Review and Letters*, 5(6):1167–1178, 1998.

[39] M. Horn-von Hoegen, F. J. M. z. Heringdorf, D. Kähler, T. Schmidt, and E. Bauer. Adsorption induced giant faceting of vicinal si(001). *Thin Solid Films*, 336(1-2):16–21, 1998.

[40] F. J. M. z. Heringdorf, R. Hild, P. Zahl, T. Schmidt, B. Ressel, S. Heun, E. Bauer, and M. Horn-von Hoegen. Local Au coverage as driving force for Au induced faceting of vicinal Si(001): a LEEM and XPEEM study. *Surface Science*, 480(3):103–108, 2001.

[41] R. Fink, M. R. Weiss, E. Umbach, D. Preikszas, H. Rose, R. Spehr, P. Hartel, W. Engel, R. Degenhardt, R. Wichtendahl, H. Kuhlenbeck, W. Erlebach, K. Ihmann, R. Schlögl, H. J. Freund, A. M. Bradshaw, G. Lilienkamp, T. Schmidt, E. Bauer, and G. Benner. Smart: A planned ultrahigh-resolution spectromicroscope for BESSY II. *Journal of Electron Spectroscopy and Related Phenomena*, 84(1-3):231–250, 1997.

[42] R. Wichtendahl, R. Fink, H. Kuhlenbeck, D. Preikszas, H. Rose, R. Spehr, P. Hartel, W. Engel, R. Schlögl, H. J. Freund, A. M. Bradshaw, G. Lilienkamp, T. Schmidt, E. Bauer, G. Benner, and E. Umbach. SMART: An aberration-corrected XPEEM/LEEM with energy filter. *Surface Review and Letters*, 5(6):1249–1256, 1998.

[43] U. Groh. *Spektromikroskopische Untersuchungen an organischen Nanostrukturen*. Dissertation, Bayerische Julius-Maximilians-Universität Würzburg, 2006.

[44] H. Marchetto, U. Groh, T. Schmidt, R. Fink, H. J. Freund, and E. Umbach. Influence of substrate morphology on organic layer growth: PTCDA on Ag(111). *Chemical Physics*, 325(1):178–184, 2006.

[45] M. Henzler. Atomic steps on single crystals: Experimental methods and properties. *Applied Physics A*, 9(1):11–17, 1976.

[46] M. Henzler. Quantitative-evaluation of random distributed steps at interfaces and surfaces. *Surface Science*, 73(1):240–251, 1978.

[47] T. M. Lu and M. G. Lagally. Diffraction from surfaces with randomly distributed steps. *Surface Science*, 120(1):47–66, 1982.

[48] J. M. Pimbley and T. M. Lu. Diffraction from surfaces with interacting steps. *Surface Science*, 159(1):169–183, 1985.

[49] J. Wollschläger, F. Schäfer, and K. M. Schröder. Diffraction spot profile analysis for vicinal surfaces with long-range order. *Surface Science*, 396(1-3):94–106, 1998.

[50] J. Wollschläger. Simple analysis of spot splitting due to diffraction at surfaces with atomic steps. *Surface Science*, 383(1):103–122, 1997.

[51] J. Wollschläger and M. Larsson. Diffraction from two-dimensional vicinal surfaces with noncolliding meandering steps. *Physical Review B*, 57(23):14937–14949, 1998.

[52] J. Wollschläger and C. Tegenkamp. Diffraction from disordered vicinal surfaces with alternating terraces. *Physical Review B*, 75(24), 2007.

[53] R. Hild, C. Seifert, M. Kammler, F.J.M.z. Heringdorf, M. Horn-von Hoegen, R. A. Zhachuk, and B. Z. Olshanetsky. Kinetics of Au induced faceting of vicinal Si(111). *Surface Science*, 512(1-2):117–127, 2002.

[54] W. Weigand. *Geometrische Struktur und Morphologie epitaktisch gewachsener ZnSe-Schichtsysteme*. Dissertation, Universität Würzburg, 2004.

[55] W. Weigand, F. Reuss, L. Hansen, A. Waag, L. W. Molenkamp, C. Kumpf, M. Sokolowski, and E. Umbach. Structure of the Te/Ge(001) surface studied by SPA-LEED. *Surface Science*, 562(1-3):33–42, 2004.

[56] F. J. M. z. Heringdorf and M. Horn-von Hoegen. Reciprocal space mapping by spot profile analyzing low energy electron diffraction. *Review of Scientific Instruments*, 76(8):085102, 2005.

[57] I. Kröger. *Geometrische Struktur von Kupfer-Phtalocyanin Submonolagen auf Ag(111)*. Diplomarbeit, Universität Würzburg, 2007.

[58] D. Sander and J. Kirschner. Cantilever stress measurements of ferromagnetic monolayers. *Applied Physics A*, 87(3):419–425, 2007.

[59] C. E. Bach, M. Giesen, H. Ibach, and T. L. Einstein. Stress relief in reconstruction. *Physical Review Letters*, 78(22):4225–4228, 1997.

[60] H. Ibach, C. E. Bach, M. Giesen, and A. Grossmann. Potential-induced stress in the solid-liquid interface: Au(111) and Au(100) in an HClO$_4$ electrolyte. *Surface Science*, 375(1):107–119, 1997.

[61] C. Bombis, M. Moiseeva, and H. Ibach. Adsorbate-induced surface stress and self-assembly of (2x1)O on Cu(110) measured with an STM. *Physical Review B*, 72(24):245408, 2005.

[62] R. Koch, H. Leonhard, G. Thurner, and R. Abermann. A UHV-compatible thin-film stress-measuring apparatus based on the cantilever beam principle. *Review of Scientific Instruments*, 61(12):3859–3862, 1990.

[63] D. Sander. *Adsorbat-induzierte Oberflächenspannungen*. PhD thesis, Rheinisch-Westfälische Technische Hochschule Aachen, 1992.

[64] D. Sander, A. Enders, and J. Kirschner. A simple technique to measure stress in ultrathin films during growth. *Review of Scientific Instruments*, 66(9):4734–4735, 1995.

[65] H. Ibach. The role of surface stress in reconstruction, epitaxial growth and stabilization of mesoscopic structures. *Surface Science Reports*, 29(5-6):195–263, 1997.

[66] D. Sander. Surface stress: implications and measurements. *Current Opinion in Solid State & Materials Science*, 7(1):51–57, 2003.

[67] W. Pan, D. Sander, M. T. Lin, and J. Kirschner. Stress oscillations and surface alloy formation during the growth of FeMn on Cu(001). *Physical Review B*, 68(22):224419, 2003.

[68] K. Dahmen, S. Lehwald, and H. Ibach. Bending of crystalline plates under the influence of surface stress - a finite element analysis. *Surface Science*, 446(1-2):161–173, 2000.

[69] R.F.S. Hearmon. The elastic constants of non-piezo-electric crystals. In K.H. Hellwege and A.M. Hellwege, editors, *Landolt-Börnstein*, volume III/2, page 3. Springer Verlag, Berlin, Neue Serie edition, 1969.

[70] P. Kury and M. Horn-von Hoegen. Impact of thermal dependence of elastic constants on surface stress measurements. *Review of Scientific Instruments*, 75(5):1357–1358, 2004.

[71] L.D. Landau and E.M. Lifshitz. *Theory of elasticity*, volume 7 of *Course of Theoretical Physics*. Reed Educational and Professional Publishing, Oxford, 3 edition, 1986.

[72] H. Ibach. The role of surface stress in reconstruction, epitaxial growth and stabilization of mesoscopic structures (vol 29, pg 193, 1997). *Surface Science Reports*, 35(1-2):71–73, 1999.

[73] H. C. Jeong and E. D. Williams. Steps on surfaces: experiment and theory. *Surface Science Reports*, 34(6-8):171–294, 1999.

[74] W. Haiss. Surface stress of clean and adsorbate-covered solids. *Reports on Progress in Physics*, 64(5):591–648, 2001.

[75] P. Müller and A. Saúl. Elastic effects on surface physics. *Surface Science Reports*, 54:157–258, 2004.

[76] D. Kramer and J. Weissmüller. A note on surface stress and surface tension and their interrelation via Shuttleworth's equation and the Lippmann equation. *Surface Science*, 601(14):3042–3051, 2007.

[77] V.A. Marichev. Comment on "A note on surface stress and surface tension and their interrelation via Shuttleworth's equation and the Lippmann equation" by D. Kramer and J. Weissmüller [Surf. Sci. 601 (2007) 3042]. *Surface Science*, 602(5):1131–1132, 2008.

[78] D. Kramer and J. Weissmüller. Reply to 'Comment on "A note on surface stress and surface tension and their interrelation via Shuttleworth's equation and the Lippmann equation" by D. Kramer and J. Weissmüller [Surf. Sci. 601 (2007) 3042]' by V.A. Marichev. *Surface Science*, 602(5):1133–1134, 2008.

[79] I.N. Bronstein, K.A. Semendjajew, G. Musiol, and H. Mühlig. *Taschenbuch der Mathematik*. Verlag Harri Deutsch, Frankfurt am Main, 4th edition, 1999.

[80] W. Nolting. *Spezielle Relativitätstheorie Thermodynamik*, volume 4 of *Grundkurs Theoretische Physik*. Springer, Berlin, 5 edition, 2005.

[81] P. Nozières and D.E. Wolf. Interfacial properties of elastically strained materials I. Thermodynamics of a planar interface. *Zeitschrift für Physik B - Condensed Matter*, 70(3):399–407, 1988.

[82] R. Shuttleworth. The surface tension of solids. *Proceedings of the Physical Society of London Section A*, 63(365):444–457, 1950.

[83] R. C. Cammarata. Surface and interface stress effects in thin-films. *Progress in Surface Science*, 46(1):1–38, 1994.

[84] C. Rottman and M. Wortis. Statistical-mechanics of equilibrium crystal shapes - interfacial phase-diagrams and phase-transitions. *Physics Reports-Review Section of Physics Letters*, 103(1-4):59–79, 1984.

[85] D. Sander, A. Enders, and J. Kirschner. Stress and magnetic properties of surfaces and ultrathin films. *Journal of Magnetism and Magnetic Materials*, 200(1-3):439–455, 1999.

[86] R. J. Needs, M. J. Godfrey, and M. Mansfield. Theory of surface stress and surface reconstruction. *Surface Science*, 242(1-3):215–221, 1991.

[87] H. Ibach. Adsorbate-induced surface stress. *Journal of Vacuum Science & Technology A*, 12(4):2240–2243, 1994.

[88] V. Heine and L. D. Marks. Competition between pairwise and multi-atom forces at noble-metal surfaces. *Surface Science*, 165(1):65–82, 1986.

[89] V. Fiorentini, M. Methfessel, and M. Scheffler. Reconstruction mechanism of fcc transition-metal (001) surfaces. *Physical Review Letters*, 71(7):1051–1054, 1993.

[90] K. Kadas, Z. Nabi, S. K. Kwon, L. Vitos, R. Ahuja, B. Johansson, and J. Kollar. Surface relaxation and surface stress of 4d transition metals. *Surface Science*, 600(2):395–402, 2006.

[91] G. Chiarotti, editor. *Physics of solid surfaces - structure*, volume 24a of *Landolt-Börnstein New Series III*. Springer-Verlag, Berlin, 1993.

[92] S. K. Kwon, Z. Nabi, K. Kadas, L. Vitos, J. Kollar, B. Johansson, and R. Ahuja. Surface energy and stress release by layer relaxation. *Physical Review B*, 72(23):235423, 2005.

[93] J. Kollar, L. Vitos, J. M. Osorio-Guillen, and R. Ahuja. Calculation of surface stress for fcc transition metals. *Physical Review B*, 68(24):245417, 2003.

[94] R. J. Needs. Calculations of the surface stress tensor at aluminum (111) and (110) surfaces. *Physical Review Letters*, 58(1):53–56, 1987.

[95] R. J. Needs and M. Mansfield. Calculations of the surface stress tensor and surface-energy of the (111) surfaces of iridium, platinum and gold. *Journal of Physics-Condensed Matter*, 1(41):7555–7563, 1989.

[96] Y. Umeno, C. Elsässer, B. Meyer, P. Gumbsch, M. Nothacker, J. Weissmüller, and F. Evers. Ab initio study of surface stress response to charging. *Europhysics Letters*, 78(1):13001, 2007.

[97] P. J. Feibelman. Anisotropy of the stress on fcc(110) surfaces. *Physical Review B*, 51(24):17867–17875, 1995.

[98] P. Gumbsch and M. S. Daw. Interface stresses and their effects on the elastic-moduli of metallic multilayers. *Physical Review B*, 44(8):3934–3938, 1991.

[99] C. W. Mays, J. S. Vermaak, and D. Kuhlmann-Wilsdorf. On surface stress and surface tension. 2. determination of surface stress of gold. *Surface Science*, 12(2):134–140, 1968.

[100] G. Apai, J. F. Hamilton, J. Stohr, and A. Thompson. Extended x-ray-absorption fine-structure of small Cu and Ni clusters - binding-energy and bond-length changes with cluster size. *Physical Review Letters*, 43(2):165–169, 1979.

[101] H.J. Wasserman and J. S. Vermaak. Determination of surface stress of copper and platinum. *Surface Science*, 32(1):168–174, 1972.

[102] R. Lamber, S. Wetjen, and N. I. Jaeger. Size dependence of the lattice-parameter of small palladium particles. *Physical Review B*, 51(16):10968–10971, 1995.

[103] H.J Wasserman and J. S. Vermaak. On determination of a lattice contraction in very small silver particles. *Surface Science*, 22(1):164–72, 1970.

[104] P. A. Montano, W. Schulze, B. Tesche, G. K. Shenoy, and T. I. Morrison. Extended x-ray-absorption fine-structure study of Ag particles isolated in solid argon. *Physical Review B*, 30(2):672–677, 1984.

[105] D. Salz, R. Lamber, M. Wark, A. Baalmann, and N. Jaeger. Metal clusters in plasma polymer matrices - Part II. silver clusters. *Physical Chemistry Chemical Physics*, 1(18):4447–4451, 1999.

[106] M. Dubiel, H. Hofmeister, and E. Schurig. Compressive stresses in Ag nanoparticle doped glasses by ion implantation. *Physica Status Solidi B-Basic Research*, 203(2):R5–R6, 1997.

[107] T. de Planta, F. Piuz, and R. Ghez. Variation de la maille de petits cristaux d'argent. *Helvetica Physica Acta*, 37(1):74–77, 1964.

[108] R. Lamber, S. Wetjen, G. Schulzekloff, and A. Baalmann. Metal-clusters in plasma polymer matrices - cold clusters. *Journal of Physical Chemistry*, 99(38):13834–13838, 1995.

[109] B. Medasani, Y. H. Park, and I. Vasiliev. Theoretical study of the surface energy, stress, and lattice contraction of silver nanoparticles. *Physical Review B*, 75(23):235436, 2007.

[110] L. D. Marks and Volker Heine. Electronically induced geometrical catalytic effects. *Journal of Catalysis*, 94(2):570–572, 1985.

[111] P. J. Feibelman. First-principles calculations of stress induced by gas adsorption on Pt(111). *Physical Review B*, 56(4):2175–2182, 1997.

[112] R. V. Kukta, D. Kouris, and K. Sieradzki. Adatoms and their relation to surface stress. *Journal of the Mechanics and Physics of Solids*, 51(7):1243–1266, 2003.

[113] M. J. Harrison, D. P. Woodruff, J. Robinson, D. Sander, W. Pan, and J. Kirschner. Adsorbate-induced surface reconstruction and surface-stress changes in Cu(100)/O: Experiment and theory. *Physical Review B*, 74(16):165402, 2006.

[114] D. Sander, U. Linke, and H. Ibach. Adsorbate-induced surface stress - Sulfur, oxygen and carbon on Ni(100). *Surface Science*, 272(1-3):318–325, 1992.

[115] A. L. D. Kilcoyne, D. P. Woodruff, A. W. Robinson, T. Lindner, J. S. Somers, and A. M. Bradshaw. A photoelectron diffraction study of the Ni(100)(2 x 2)-C(p4g) and Ni(100)(2 x 2)-N(p4g) structures. *Surface Science*, 253(1-3):107–115, 1991.

[116] S. Y. Hong, A. Kara, T. S. Rahman, R. Heid, and K. P. Bohnen. Ab initio calculations of adsorbate-induced stress on Ni(100). *Physical Review B*, 69(19):195403, 2004.

[117] S. Stolbov, S. Y. Hong, A. Kara, and T. S. Rahman. Origin of the C-induced p4g reconstruction of Ni(001). *Physical Review B*, 72(15):155423, 2005.

[118] A. Grossmann, W. Erley, and H. Ibach. Adsorbate-induced surface stress and surface reconstruction: Oxygen, sulfur and carbon on Ni(111). *Surface Science*, 337(3):183–189, 1995.

[119] M. Godin, P. J. Williams, V. Tabard-Cossa, O. Laroche, L. Y. Beaulieu, R. B. Lennox, and P. Grutter. Surface stress, kinetics, and structure of alkanethiol self-assembled monolayers. *Langmuir*, 20(17):7090–7096, 2004.

[120] R. Berger, E. Delamarche, H. P. Lang, C. Gerber, J. K. Gimzewski, E. Meyer, and H. J. Güntherodt. Surface stress in the self-assembly of alkanethiols on gold. *Science*, 276(5321):2021–2024, 1997.

[121] P. Shrotriya, K. K. S. Karuppiah, R. Zhang, A. Chandra, and S. Sundararajan. Surface stress generation during formation of alkanethiol self-assembled monolayer (SAM). *Mechanics Research Communications*, 35(1-2):43–49, 2008.

154

[122] R. Berger, E. Delamarche, H. P. Lang, C. Gerber, J. K. Gimzewski, E. Meyer, and H. J. Güntherodt. Surface stress in the self-assembly of alkanethiols on gold probed by a force microscopy technique. *Applied Physics A*, 66:55–59, 1998.

[123] A.G. Hansen, M.W. Mortensen, J.E.T. Andersen, J. Ulstrup, A. Kühle, J. Garnæs, and A. Boisen. Stress formation during self-assembly of alkanethiols on differently pre-treated gold surfaces. *Probe Microscopy*, 2(2):139, 2001.

[124] P. Kury, K. R. Roos, M. Horn-von Hoegen, and F. J. M. z. Heringdorf. Absence of surface stress change during pentacene thin film growth on the Si(111)-(7x7) surface: A buried reconstruction interface. *New Journal of Physics*, 10:023037, 2008.

[125] G. E. Poirier and E. D. Pylant. The self-assembly mechanism of alkanethiols on Au(111). *Science*, 272(5265):1145–1148, 1996.

[126] M. Godin, V. Tabard-Cossa, P. Grutter, and P. Williams. Quantitative surface stress measurements using a microcantilever. *Applied Physics Letters*, 79(4):551–553, 2001.

[127] J. Zang and F. Liu. Theory of bending of Si nanocantilevers induced by molecular adsorption: A modified Stoney formula for the calibration of nanomechanochemical sensors. *Nanotechnology*, 18(40):405501, 2007.

[128] X. F. Li and X. L. Peng. Theoretical analysis of surface stress for a microcantilever with varying widths. *Journal of Physics D*, 41(6):065301, 2008.

[129] H. Clausen-Schaumann, M. Rief, and M. Seitz. Artificial noses sniff DNA. *ChemPhysChem*, 1(2):89–92, 2000.

[130] C. Ziegler. Cantilever-based biosensors. *Analytical and Bioanalytical Chemistry*, 379(7-8):946–959, 2004.

[131] K. M. Goeders, J. S. Colton, and L. A. Bottomley. Microcantilevers: Sensing chemical interactions via mechanical motion. *Chemical Reviews*, 108(2):522–542, 2008.

[132] A. Hauschild, K. Karki, B. C. C. Cowie, M. Rohlfing, F. S. Tautz, and M. Sokolowski. Molecular distortions and chemical bonding of a large pi-conjugated molecule on a metal surface. *Physical Review Letters*, 94(3):036106, 2005.

[133] C. Stadler, S. Hansen, F. Pollinger, C. Kumpf, E. Umbach, T. L. Lee, and J. Zegenhagen. Structural investigation of the adsorption of SnPc on Ag(111) using normal-incidence x-ray standing waves. *Physical Review B*, 74(3), 2006.

[134] E. Umbach. Characterization of organic overlayers on well-defined substrates. *Progress in Surface Science*, 35(1-4):113–127, 1990.

[135] E. Umbach, C. Seidel, J. Taborski, R. Li, and A. Soukopp. Highly-ordered organic adsorbates: Commensurate superstructures, OMBE, and 1D nanostructures. *Physica Status Solidi B-Basic Research*, 192(2):389–406, 1995.

[136] E. Umbach, K. Glöckler, and M. Sokolowski. Surface "architecture" with large organic molecules: Interface order and epitaxy. *Surface Science*, 404(1-3):20–31, 1998.

[137] G. Witte and C. Wöll. Growth of aromatic molecules on solid substrates for applications in organic electronics. *Journal of Materials Research*, 19(7):1889–1916, 2004.

[138] F.S. Tautz. Structure and bonding of large aromatic molecules on noble metal surfaces: The example of PTCDA. *Progress in Surface Science*, 82(9-12):479–520, 2007.

[139] B. Krause, A. C. Dürr, K. Ritley, F. Schreiber, H. Dosch, and D. Smilgies. Structure and growth morphology of an archetypal system for organic epitaxy: PTCDA on Ag(111). *Physical Review B*, 66(23):235404, 2002.

[140] L. Chkoda, M. Schneider, V. Shklover, L. Kilian, M. Sokolowski, C. Heske, and E. Umbach. Temperature-dependent morphology and structure of ordered 3,4,9,10-perylene-tetracarboxylicacid-dianhydride (PTCDA) thin films on Ag(111). *Chemical Physics Letters*, 371(5-6):548–552, 2003.

[141] L. Kilian, E. Umbach, and M. Sokolowski. Molecular beam epitaxy of organic films investigated by high resolution low energy electron diffraction (SPA-LEED): 3,4,9,10-perylenetetracarboxylicacid-dianhydride (PTCDA) on Ag(111). *Surface Science*, 573(3):359–378, 2004.

[142] K. Glöckler, C. Seidel, A. Soukopp, M. Sokolowski, E. Umbach, M. Böhringer, R. Berndt, and W. D. Schneider. Highly ordered structures and submolecular scanning tunnelling microscopy contrast of PTCDA and DM-PBDCI monolayers on Ag(111) and Ag(110). *Surface Science*, 405(1):1–20, 1998.

[143] A. Kraft, R. Temirov, S. K. M. Henze, S. Soubatch, M. Rohlfing, and F. S. Tautz. Lateral adsorption geometry and site-specific electronic structure of a large organic chemisorbate on a metal surface. *Physical Review B*, 74(4):041402, 2006.

[144] A. Gerlach, S. Sellner, F. Schreiber, N. Koch, and J. Zegenhagen. Substrate-dependent bonding distances of PTCDA: A comparative x-ray standing-wave study on Cu(111) and Ag(111). *Physical Review B*, 75(4):045401, 2007.

[145] J. Taborski, P. Väterlein, H. Dietz, U. Zimmermann, and E. Umbach. NEX-AFS investigations on ordered adsorbate layers of large aromatic molecules. *Journal of Electron Spectroscopy and Related Phenomena*, 75:129–147, 1995.

[146] A. Schöll, Y. Zou, D. Hübner, S. G. Urquhart, Th. Schmidt, R. Fink, and E. Umbach. A comparison of fine structures in high-resolution x-ray-absorption spectra of various condensed organic molecules. *The Journal of Chemical Physics*, 123(4):044509, 2005.

[147] B. Krause, A. C. Dürr, F. Schreiber, H. Dosch, and O. H. Seeck. Thermal stability and partial dewetting of crystalline organic thin films: 3,4,9,10-perylenetetracarboxylic dianhydride on Ag(111). *Journal of Chemical Physics*, 119(6):3429–3435, 2003.

[148] R. Rurali, N. Lorente, and P. Ordejon. Comment on "molecular distortions and chemical bonding of a large pi-conjugated molecule on a metal surface". *Physical Review Letters*, 95(20):209601, 2005.

[149] A. Hauschild, K. Karki, B. C. C. Cowie, M. Rohlfing, F. S. Tautz, and M. Sokolowski. Comment on "molecular distortions and chemical bonding of a large pi-conjugated molecule on a metal surface" - reply. *Physical Review Letters*, 95(20):209602, 2005.

[150] M. Rohlfing, R. Temirov, and F. S. Tautz. Adsorption structure and scanning tunneling data of a prototype organic-inorganic interface: PTCDA on Ag(111). *Physical Review B*, 76(11):115421, 2007.

[151] Y. Zou, L. Kilian, A. Schöll, T. Schmidt, R. Fink, and E. Umbach. Chemical bonding of PTCDA on Ag surfaces and the formation of interface states. *Surface Science*, 600(6):1240–1251, 2006.

[152] S. Picozzi, A. Pecchia, M. Gheorghe, A. Di Carlo, P. Lugli, B. Delley, and M. Elstner. Schottky barrier height at an organic/metal junction: A first-principles study of PTCDA/X (X = Al, Ag) contacts. *Physical Review B*, 68(19):195309, 2003.

[153] M. Eremtchenko, J. A. Schaefer, and F. S. Tautz. Understanding and tuning the epitaxy of large aromatic adsorbates by molecular design. *Nature*, 425(6958):602–605, 2003.

[154] F. S. Tautz, M. Eremtchenko, J. A. Schaefer, M. Sokolowski, V. Shklover, K. Glöckler, and E. Umbach. A comparison of the chemisorption behaviour of PTCDA on different Ag surfaces. *Surface Science*, 502:176–184, 2002.

[155] Y. Zou. *Electronic properties of organic molecular thin films in condensed- and interfacial states with metal substrates.* Dissertation, Bayerische Julius-Maximilians-Universität Würzburg, 2003.

[156] L. Kilian, A. Hauschild, R. Temirov, S. Soubatch, A. Schöll, A. Bendounan, F. Reinert, T. L. Lee, F. S. Tautz, M. Sokolowski, and E. Umbach. Role of intermolecular interactions on the electronic and geometric structure of a large pi-conjugated molecule adsorbed on a metal surface. *Physical Review Letters*, 100(13):136103, 2008.

[157] R. Temirov, S. Soubatch, A. Luican, and F. S. Tautz. Free-electron-like dispersion in an organic monolayer film on a metal substrate. *Nature*, 444(7117):350–353, 2006.

[158] S. Sachs, C.H. Schwalb, M. Marks, F. Reinert, A. Schöll, E. Umbach, and U. Höfer. About the character of a metal-organic interface state in PTCDA/Ag(111). In *ECOSS 25*, Liverpool, 2008.

[159] Stefan Schmitt. *Adsorbatinduzierte richtungsabhängige Facettierung und selbstorganisierte Domänen-Musterbildung auf vizinalen Ag(111)-Oberflächen.* Dissertation, Universiät Würzburg, 2006.

[160] S. J. Stranick, M. M. Kamna, and P. S. Weiss. Atomic-scale dynamics of a 2-dimensional gas-solid interface. *Science*, 266(5182):99–102, 1994.

[161] Falk Viczian. *Präparation und Adsorption auf gestuften Einkristalloberflächen: Thiophen auf Ag(S)-[6(111)x(100)].* Diplomarbeit, Universität Stuttgart, 1992.

[162] Eric I. Altman and Richard J. Colton. Nucleation, growth, and structure of fullerene films on Au(111). *Surface Science*, 279(1-2):49–67, 1992.

[163] M. D. Alvey, K. W. Kolasinski, J. T. Yates, and M. Headgordon. Molecular-orientation on metal-surfaces by electrostatic interactions - the adsorption of cyclopentene on a stepped (221) silver surface. *Journal of Chemical Physics*, 85(10):6093–6099, 1986.

[164] S. Lukas, S. Vollmer, G. Witte, and C. Wöll. Adsorption of acenes on flat and vicinal Cu(111) surfaces: Step induced formation of lateral order. *Journal of Chemical Physics*, 114(22):10123–10130, 2001.

[165] L. Gavioli, M. Fanetti, M. Sancrotti, and M. G. Betti. Long-range-ordered pentacene chains assembled on the Cu(119) vicinal surface. *Physical Review B*, 72(3):03458–03463, 2005.

[166] N. Néel, J. Kröger, and R. Berndt. Highly periodic fullerene nanomesh. *Advanced Materials*, 18(2):174–177, 2006.

[167] F. M. Leibsle, S. Haq, B. G. Frederick, M. Bowker, and N. V. Richardson. Molecularly induced step faceting on Cu(110) surfaces. *Surface Science*, 343(3):L1175–L1181, 1995.

[168] J.I. Pascual, J.V. Barth, G. Ceballos, G. Trimarchi, A. De Vita, K. Kern, and H.-P. Rust. Mesoscopic chiral reshaping of the Ag(110) surface induced by the organic molecule PVBA. *Journal of Chemical Physics*, 120(24):11367–11370, 2004.

[169] Q. Chen, D. J. Frankel, and N. V. Richardson. Organic adsorbate induced surface reconstruction: p-aminobenzoic acid on Cu110. *Langmuir*, 17(26):8276–8280, 2001.

[170] X. Y. Zhao, H. Wang, R. G. Zhao, and W. S. Yang. Self-assembly of amino acids on the Cu(001) surface. *Materials Science & Engineering C*, 16(1-2):41–50, 2001.

[171] Q. Chen and N. V. Richardson. Surface facetting induced by adsorbates. *Progress in Surface Science*, 73(4-8):59–77, 2003.

[172] X. Y. Zhao. Fabricating homochiral facets on Cu(001) with L-lysine. *Journal of the American Chemical Society*, 122(50):12584–12585, 2000.

[173] M. Böhringer, R. Berndt, and W.-D. Schneider. Transition from three-dimensional to two-dimensional faceting of Ag(110) induced by Cu-phthalocyanine. *Physical Review B*, 55(3):1384–1387, 1997.

[174] A. Tamai, W. Auwärter, C. Cepek, F. Baumberger, T. Greber, and J. Osterwalder. One-dimensional chains of C-60 molecules on Cu(221). *Surface Science*, 566:633–637, 2004.

[175] M. Fanetti, L. Gavioli, M. Sancrotti, and M. G. Betti. Morphology of pentacene films deposited on Cu(119) vicinal surface. *Applied Surface Science*, 252(15):5568–5571, 2006.

[176] B. Mutaftschiev. *The Atomistic Nature of Crystal Growth.* Materials Science. Springer Verlag, Berlin, 1 edition, 2001.

[177] G. Wulff. *Zeitschrift für Kristallographie*, 34:449, 1901.

[178] Conyers Herring. Some theorems on the free energies of crystal surfaces. *Physical Review*, 82(1):87 LP – 93, 1951.

[179] E. E. Gruber and W. W. Mullins. On the theory of anisotropy of crystalline surface tension. *Journal of Physics and Chemistry of Solids*, 28(5):875–887, 1967.

[180] C. Jayaprakash, Craig Rottman, and W. F. Saam. Simple model for crystal shapes: Step-step interactions and facet edges. *Physical Review B*, 30(11):6549 – 6554, 1984.

[181] R. Smoluchowski. Anisotropy of the electronic work function of metals. *Physical Review*, 60(9):661–674, 1941.

[182] B. Croset, Y. Girard, G. Prévot, M. Sotto, Y. Garreau, R. Pinchaux, and M. Sauvage-Simkin. Measuring surface stress discontinuities in self-organized systems with X rays. *Physical Review Letters*, 88(5):056103, 2002.

[183] V.A. Shchukin and D. Bimberg. Spontaneous ordering of nanostructures on crystal surfaces. *Reviews of Modern Physics*, 71(4):1125–1171, 1999.

[184] P. Zeppenfeld, M. Krzyzowski, C. Romainczyk, G. Comsa, and M. G. Lagally. Size relation for surface systems with long-range interactions. *Physical Review Letters*, 72(17):2737–2740, 1994.

[185] Peter Zeppenfeld and Michael Hohage. Nanostrukturierte Oberflächen. *Physikalische Blätter*, 56(11):33–38, 2000.

[186] G. Prévot, B. Croset, A. Coati, Y. Garreau, and Y. Girard. Self-organized systems for measuring surface stress at the nanoscale: N and O adsorption on Cu(001). *Physical Review B*, 73(20):205418, 2006.

[187] G. Prévot, B. Croset, Y. Girard, A. Coati, Y. Garreau, M. Hohage, L. D. Sun, and P. Zeppenfeld. Elastic origin of the O/Cu(110) self-ordering evidenced by GIXD. *Surface Science*, 549(1):52–66, 2004.

[188] J. A. Venables, G. D. T. Spiller, and M. Hanbücken. Nucleation and growth of thin-films. *Reports on Progress in Physics*, 47(4):399–459, 1984.

[189] J. W. Evans and M. C. Bartelt. Nucleation and growth in metal-on-metal homoepitaxy - rate-equations, simulations and experiments. *Journal of Vacuum Science & Technology A*, 12(4):1800–1808, 1994.

[190] T. R. Linderoth, J. J. Mortensen, K. W. Jacobsen, E. Laegsgaard, I. Stensgaard, and F. Besenbacher. Homoepitaxial growth of Pt on Pt(100)-hex: Effects of strongly anisotropic diffusion and finite island sizes. *Physical Review Letters*, 77(1):87–90, 1996.

[191] J. A. Stroscio and D. T. Pierce. Scaling of diffusion-mediated island growth in iron-on-iron homoepitaxy. *Physical Review B*, 49(12):8522–8525, 1994.

[192] J. J. Mortensen, T. R. Linderoth, K. W. Jacobsen, E. Laegsgaard, I. Stensgaard, and F. Besenbacher. Effects of anisotropic diffusion and finite island sizes in homoepitaxial growth Pt on Pt(100)-hex. *Surface Science*, 400(1-3):290–313, 1998.

[193] J. A. Blackman and P. A. Mulheran. Scaling behavior in submonolayer film growth: A one-dimensional model. *Physical Review B*, 54(16):11681–11692, 1996.

[194] P. A. Mulheran and J. A. Blackman. Simulation and theory of island growth on substrate steps. *Surface Science*, 376(1-3):403–410, 1997.

[195] P. Bayersdorfer. Diplomarbeit, Universität Würzburg, 2008.

[196] D. Nečak and P. Klapetek. Gwyddion V2.10. *http://gwyddion.net.*

[197] P. Klapetek, I. Ohlidal, D. Franta, A. Montaigne-Ramil, A. Bonanni, D. Stifter, and H. Sitter. Atomic force microscopy characterization of ZnTe epitaxial films. *Acta Physica Slovaca*, 53(3):223–230, 2003.

[198] A. Ulman. Formation and structure of self-assembled monolayers. *Chemical Reviews*, 96(4):1533–1554, 1996.

[199] G. E. Poirier. Characterization of organosulfur molecular monolayers on Au(111) using scanning tunneling microscopy. *Chemical Reviews*, 97(4):1117–1127, 1997.

[200] F. Schreiber. Structure and growth of self-assembling monolayers. *Progress in Surface Science*, 65(5-8):151–256, 2000.

[201] F. Schreiber. Self-assembled monolayers: from 'simple' model systems to biofunctionalized interfaces. *Journal of Physics-Condensed Matter*, 16(28):R881–R900, 2004.

[202] M. Himmelhaus, I. Gauss, M. Buck, F. Eisert, C. Woll, and M. Grunze. Adsorption of docosanethiol from solution on polycrystalline silver surfaces: an XPS and NEXAFS study. *Journal of Electron Spectroscopy and Related Phenomena*, 92(1-3):139–149, 1998.

[203] H. Kondoh, C. Kodama, H. Sumida, and H. Nozoye. Molecular processes of adsorption and desorption of alkanethiol monolayers on Au(111). *Journal of Chemical Physics*, 111(3):1175–1184, 1999.

[204] P. Fenter, P. Eisenberger, J. Li, N. Camillone, S. Bernasek, G. Scoles, T. A. Ramanarayanan, and K. S. Liang. Structure of $CH_3(CH_2)_{17}SH$ self-assembled on the Ag(111) surface - an incommensurate monolayer. *Langmuir*, 7(10):2013–2016, 1991.

[205] R. Heinz and J. P. Rabe. Scanning-tunneling-microscopy investigation of sulfide and alkanethiolate adlayers on Ag(111). *Langmuir*, 11(2):506–511, 1995.

[206] P. E. Laibinis, G. M. Whitesides, D. L. Allara, Y. T. Tao, A. N. Parikh, and R. G. Nuzzo. Comparison of the structures and wetting properties of self-assembled monolayers of normal-alkanethiols on the coinage metal-surfaces, Cu, Ag, Au. *Journal of the American Chemical Society*, 113(19):7152–7167, 1991.

[207] H. Kondoh, A. Nambu, Y. Ehara, F. Matsui, T. Yokoyama, and T. Ohta. Substrate dependence of self-assembly of alkanethiol: X-ray absorption fine structure study. *Journal of Physical Chemistry B*, 108(34):12946–12954, 2004.

[208] R. Staub, M. Toerker, T. Fritz, T. Schmitz-Hübsch, F. Sellam, and K. Leo. Scanning tunneling microscope investigations of organic heterostructures prepared by a combination of self-assembly and molecular beam epitaxy. *Surface Science*, 445(2-3):368–379, 2000.

[209] M. C. Gerstenberg, F. Schreiber, T. Y. B. Leung, G. Bracco, S. R. Forrest, and G. Scoles. Organic semiconducting thin film growth on an organic substrate: 3,4,9,10-perylenetetracarboxylic dianhydride on a monolayer of decanethiol self-assembled on Au(111). *Physical Review B*, 61(11):7678–7685, 2000.

[210] F. Schreiber, M. C. Gerstenberg, H. Dosch, and G. Scoles. Melting point enhancement of a self-assembled monolayer induced by a van der waals bound capping layer. *Langmuir*, 19(24):10004–10006, 2003.

[211] P. Väterlein, M. Schmelzer, J. Taborski, T. Krause, F. Viczian, M. Bäßler, R. Fink, E. Umbach, and W. Wurth. Orientation and bonding of thiophene and 2,2 '-bithiophene on Ag(111): A combined near edge extended X-ray absorption fine structure and X alpha scattered-wave study. *Surface Science*, 452(1-3):20–32, 2000.

[212] S. Tanuma, C. J. Powell, and D. R. Penn. Calculations of electron inelastic mean free paths. 5. Data for 14 organic-compounds over the 50-2000 eV range. *Surface and Interface Analysis*, 21(3):165–176, 1994.

Danksagung

An dieser Stelle möchte ich all denen danken, die zum Gelingen dieser Arbeit beigetragen haben:

Prof. Dr. Eberhard Umbach möchte ich für das Vertrauen und die interessante Themenstellung danken. Er hat mir ein sehr freies, wissenschaftliches Arbeiten ermöglicht und war immer bereit in kniffligen oder auch brenzligen Situationen weiterzuhelfen. Seine Denkanstöße, seine Ideen und sein Optimismus haben mich durch das sehr weite Feld einer Dissertation geleitet.

Prof. Dr. Kai Fauth danke ich für seine freundliche Bereitschaft das Zweitgutachten zu übernehmen und auch ganz besonders für die geplante rasante Anfertigung desselben.

Prof. Dr. Friedrich Reinert hat bewiesen, dass seine Tür nicht grundlos offen steht. Er war immer bereit sich sowohl mit experimentellen Tages- als auch mit grundlegenderen Verständnisproblemen auseinanderzusetzen.

Bei **Dr. Achim Schöll** möchte ich mich für seine jahrelange Unterstützung bedanken. Mit seiner großen Erfahrung und seiner anpackenden Art hat er mir sehr geholfen.

Auch **Dr. Christian Kumpf** war immer bereit zu diskutieren und (nicht nur) im reziproken Raum weiterzuhelfen.

Die Biegekristallmessungen sind das Ergebnis einer hervorragenden Zusammenarbeit mit **Dr. Dirk Sander**, **Dr. Zhen Tian** und **Prof. Dr. Jürgen Kirschner** vom Max-Planck-Institut für Mikrostrukturphysik in Halle. Dr. Sander war nicht nur bereit mir seinen Aufbau anzuvertrauen, sondern auch die ganze Zeit dabei involviert, reproduzierbare und robuste Ergebnisse zu erlangen. Seine Hinweise und Beiträge zur Interpretation waren für mich von sehr großem Wert.

Lebenslauf

Persönliche Daten:

Name: Florian Pollinger
Geburtstag: 31. März 1979
Geburtsort: Erlenbach am Main
Wohnort: Würzburg
Staatsangehörigkeit: deutsch
Familienstand: verheiratet, ein Sohn (7 Monate)

Schulausbildung:

09/85 - 07/89   Grundschule Klingenberg
09/89 - 06/98   Hermann-Staudinger-Gymnasium Erlenbach
26.06.1998   Abitur
07/98 - 04/99   Wehrdienst

Hochschulausbildung:

10/99 - 07/02   Studium der Physik an der Universität Würzburg
08/02 - 08/03   Masterarbeit an der University of Texas at Austin
                         Thema der Arbeit: "Design of a
                         Time-Resolved Reflectance Difference Spectrometer"
18.08.2003   Master of Arts in Physics
11/03 - 12/08   Promotion am Lehrstuhl für Experimentelle Physik II
                         am Physikalischen Institut der Universität Würzburg